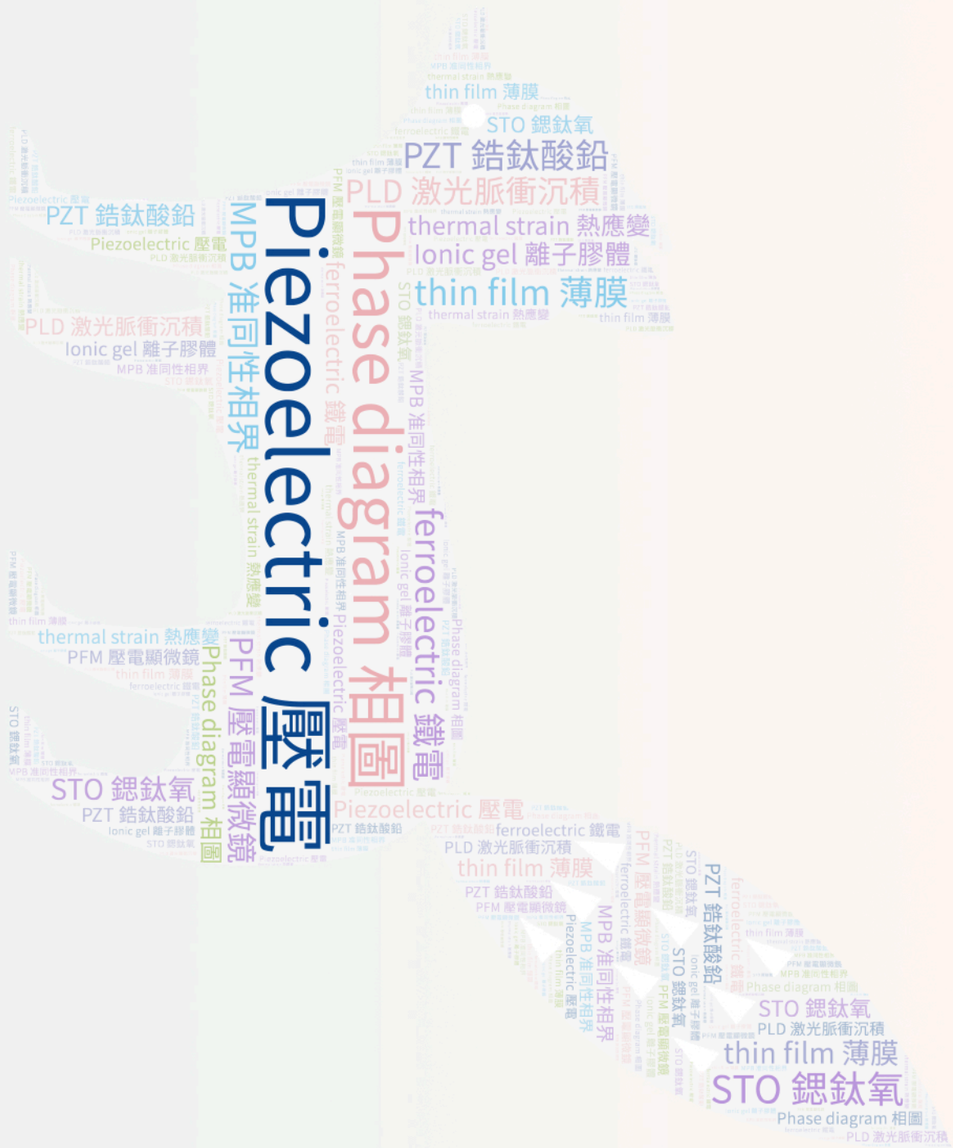

ISBN: 978-90-365-5276-9

Symmetry and functional properties of clamped $Pb(Zr_{0.6}Ti_{0.4})O_3$ tuned by thermal strain and electrostatics effects

Sizhao Huang

SYMMETRY AND FUNCTIONAL PROPERTIES OF CLAMPED $Pb(Zr_{0.6}Ti_{0.4})O_3$ TUNED BY THERMAL STRAIN AND ELECTROSTATICS EFFECTS

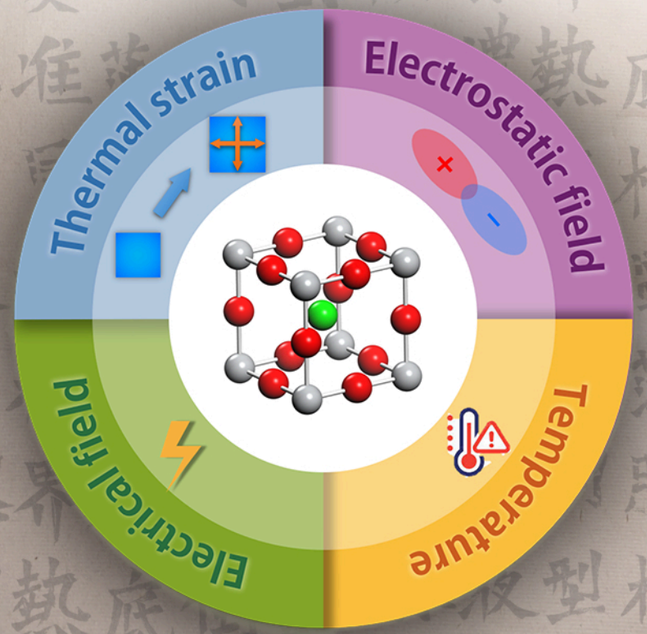

SIZHAO HUANG

Invitation

to

public defense
of
Ph.d. dissertation

on 3rd Nov. 2021
at 16:45h

Sizhao Huang
bismarck96@gmail.com

Paranymphs:
Zhen Wu
Yury Smirnov

Symmetry and functional properties of clamped $Pb(Zr_{0.6}Ti_{0.4})O_3$ tuned by thermal strain and electrostatics effects

Sizhao Huang (黄斯昭)

Symmetry and functional properties of clamped $Pb(Zr_{0.6}Ti_{0.4})O_3$ tuned by thermal strain and electrostatics effects

Dissertation

to obtain
the degree of doctor at the Universiteit Twente,
on the authority of the rector magnificus,
prof. dr. ir. A. Veldkamp,
on account of the decision of the Doctorate Board
to be publicly defended
on Wednesday 3 November 2021 at 16.45 hours

by

Sizhao Huang (黄斯昭)

Born on the 15th of December 1987
Henan, P. R. China

This dissertation has been approved by:

Supervisors
Prof.dr.ing. A.J.H.M. Rijnders
Prof.dr.ir. G. Koster

Cover design:	The cover was made by S. Huang. The background shows the keywords of this thesis in Weibei calligraphy (front cover). The inserted figure indicates four manipulation methods that used in this thesis. The back cover shows the keywords of this thesis in English.
Printed by:	Ipskamp Printing
ISBN:	978-90-365-5276-9
DOI:	10.3990/1.9789036552769

Graduation Committee:

Chair / secretary:	Prof. dr. J.G.E. Gardeniers
Supervisors:	Prof. dr. ing. A.J.H.M. Rijnders Prof. dr. ir. G. Koster
Assistant Promoter:	Dr. ir. E.P. Houwman
Committee Members:	Prof. dr. M.D. Ackermann Prof. dr. ir. W.G. van der Wiel Prof. dr. ir. J.E. ten Elshof Prof. dr. ir. B.J. Kooi Prof. dr. P. Yu Dr. ir. F.R. Blom

Contents

Chapter 1 Introduction

The year of 2020 is exactly 100 years since ferroelectricity was first reported. In 1920, at the University of Minnesota, French Joseph Valasek found ferroelectricity in Rochelle salt ($NaKC_4H_4O_6 \cdot 4H_2O$), while he was only a graduate student, guided by Prof. W.F.G. Swan.[1, 2]

In this chapter, the concepts of ferroelectricity and piezoelectricity are introduced, and one of the most widely used ferroelectric materials $PbTi_xZr_{1-x}O_3$ (PZT) is discussed. Some applications will be briefly presented.

Furthermore, a phenomenological methodology and a three-domain model to model structural and functional behaviour of PZT is described in this chapter. Pulsed laser deposition (PLD) is introduced as a thin film fabrication technique and the growth parameters are addressed. X-ray diffraction (XRD) and scanning probe microscope (SPM) characterisation techniques are addressed. Strain engineering is discussed and its progress in the past years.

Finally, the main aim and the motivation of this project is described, which is to find experimental proof for the three-domain model and Vergeer's series predictions for $x = 0.6$ composition PZT.[3, 4] By applying the techniques described previously, we have successfully achieved that goal. At the end of this chapter, the thesis outline is provided.

1.1. The first hundred years of ferroelectric materials

It was Debye who first proposed that a permanent dipole moment can exist in some molecules. In addition, he showed that dipole moment alignment can be achieved by changing the temperature. Analogous to Langevin's paramagnetism theory, Debye proposed a Curie temperature for phase transition between a paraelectric phase and the ferroelectrical phase.[5, 6] Later in the same year of 1912, Schrödinger proposed in his thesis that a solid could be ferroelectric when the solid dipole moments are aligned.[7]

Rochelle salt was reported for its high electromechanical properties, leading Joseph Valasek to perform a series of experiments, altering the temperature and electric field

over $NaKC_4H_4O_6 \cdot 4H_2O$.[1] In 1920, he discovered the "*piezo-electric and allied phenomena*". He became the first person to use the terms of *spontaneous polarisation* and *Curie point*.[8]

During World War II, the need for high performance military sonar and radar rose. This drove several discoveries of new high permittivity materials for capacitors. In 1941, Hans Thurnauer from the Lava company discovered $BaTiO_3$.[9, 10] (Some post war document suggests that the discoveries of $BaTiO_3$ ceramic were also independently made by R. B. Grey from Erie resistor company, Shepard Robert from MIT and Goldman from Russia).[9, 11, 12] During the summer of 1944 in the UK, Helen Megaw received a batch of high quality capacitors from America and started to study $BaTiO_3$ by X-ray diffraction.[13] She solved the symmetries and described the tetragonal and cubic phases. The results were not released until 1945 because of the 1917 Espionage act.

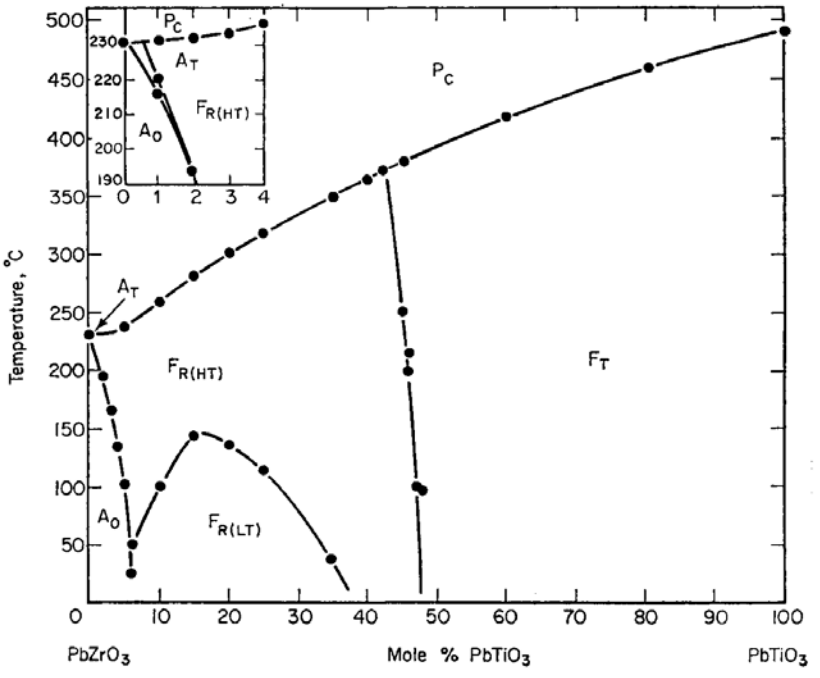

Figure 1.1. *The PZT composition phase diagram with temperature against Zr/Ti composition ratio.[14] The ferroelectric tetragonal is labelled as F_T, ferroelectric rhombohedral phase at high temperature is $F_{R(HT)}$, ferroelectric rhombohedral phase at*

low temperature is $F_{R(LT)}$, anti-ferroelectric orthorhombic phase is A_o and P_c is para-electric cubic phase.

Anti-ferroelectrics gained further attention with the discovery of $PbZrO_3$, followed in 1952, with the discovery of the solid solution from $PbTiO_3$ and $PbZrO_3$ (PZT) by Shirane and Takeda.[15-17] PZT has now become one of most important commercial piezoelectric ceramics. The unconventionally large piezoelectric response was found in a transition region in PZT composition phase diagram by Bernard Jaffe.[18] This phase boundary region between rhombohedral phase and tetragonal phase was later referred to as the morphotropic phase boundary (MPB) by Hans Jaffe and Bob Roth in 2001.[19, 20] With the two Jaffes' contributions, W. R. Cook was able to complete his PZT composition phase diagram since 1971, until Noheda et al. filled the last piece, by confirming MPB is low symmetry monoclinic phase in 2000.[14, 21-23] More details of PZT are discussed in 1.1.2.

Other important ferroelectric materials have now been introduced. Royen and Swars first synthesised and measured a multi-ferroelectric material in 1950, $BiFeO_3$.[24] This material simultaneously and spontaneously exhibits ferroelectric, ferroelastic and anti-ferromagnetic behaviour at room temperature. $LiNbO_3$ was found and commercially used at high temperature due to its high Curie point. [25] Apart from conventional organic ferroelectric materials such as PVDF, a series of single-phase new class metal-organic frameworks (MOFs) has been intensively studied, especially organometal trihalide perovskites (OTPs) show great advantages in various applications, for example in photovoltaic and wearable electronics.[26, 27] It is also noted that a family of metal-free organic perovskite ferroelectrics discovered in 2018 shows similar properties as $BaTiO_3$ but with approximately, 100°C higher Curie temperature point.[28]

Next to the unique ferroelectric materials mentioned previously, new materials have been developed and studied showing remarkably high piezoelectric coefficients. In between 1968-1971, a unique diffuse scattering was first reported in $NaNbO_3$ above Curie temperature, due to its rare micropolar regions and short-distance polarisation disorder.[29, 30] This family of perovskite ferroelectrics were then referred to as relaxors or ferroelectrical relaxors. Their nanoscale random distributed dipole moment regions were named polar nanoregions (PNRs). For PZT solid solution, the

major strategies to create local distortions and inhomogeneities in the lattices to get relaxor behaviour are 7% - 10% A-site substitution with La^{+} as well as B-site substitution with Mg^{2+} and Nb^{5+}. As the crystalline quality was improved in 1990s, Shrout and Park reported a piezoelectric coefficient as much as 2500 pC/N in $PbMg_{1/3}Nb_{2/3}O_3$-$PbTiO_3$ (PMN-PT) relaxor.[31] Compared with parent PZT single crystal, the PNRs electrostatic and elastic energies in PMN-PT attribute to a discontinuity of polarisation and strain at the interface between PNRs and ferroelectric matrix, which drive the dipole moments in PNRs to align with the matrix long-distance ferroelectric order. This results in a dramatic enhancement in flexoelectric response and piezoelectric properties, which has been reported for many other high quality single crystal relaxors.[32, 33] For example, a significant improvement of piezoelectric coefficient of 4000 pC/N was found in Sm doped PMN-PT indicating that artificial design and doping is a successful manipulation approach.[34, 35]

1.1.1. *Electrostriction, piezoelectricity and ferroelectricity*

Piezoelectricity comes from the combination of Greek terms *piezein* (means pressing) and *electricity*. Both electrostriction and piezoelectricity are coupling effect terms to describe the relationship between mechanical strain and an electrical field. Most dielectrics (solid or liquid) can show deformation or strain proportional to the square of an external electrical field, whereas 21-non-centrosymmetric symmetries materials show an inverse piezoelectrical effect where the strain is linear to the electrical field. In addition, using strain to generate dipole moments are also observed in piezoelectric.

The item of ferroelectric came after ferromagnetics, since the relationship between spontaneous polarisation and electrical field strength in ferroelectric is simialr with the relationship of magnetic moment to magnetic field strength in ferromagtics. Compared with other piezoelectric materials, ferroelectric perovskites show a spontaneous polarisation in combination with remarkably high piezoelectric coefficients and coupling coefficients. For example, the first ferroelectric perovskite material $BaTiO_3$ reported approximately 190 pC/N, in contrast with quartz 2 pC/N.[36, 37] Several ferroelectrics studies suggest that the piezoelectric coefficient is approximately proportional to the spontaneous polarisation, when the

electrostriction coefficient and dielectric constant. Therefore, a delicate balance between strong polarisation and short-distance domain orientation order can be one reason that contributes to the favourable piezoelectric properties of ferroelectric materials; however, this balance usually leads to a low Curie temperature, which is not ideal for applications.

1.1.2. *$Pb(Zr_xTi_{1-x})O_3$ (PZT)*

At this moment, environmental concerns force the industry towards lead-free ferroelectrics, such as $BaTiO_3$, whereas the $BaTiO_3$ was first replaced by PZT in 1950's due to PZT outstanding piezoelectric response (300 pC/N) and temperature stability (Curie temperature above 300 °C).[38]

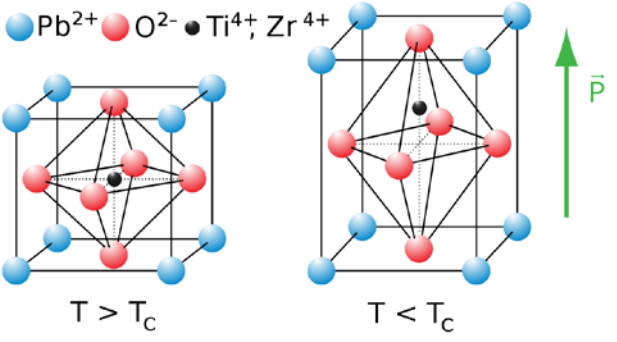

Figure 1.2. *The unit cell structure of tetragonal phase PZT with a schematic illustration of upwards polarisation.*

Fundamental research in PZT primarily focussed on the MPB compositions and the effects of doping. If B-site substitutes Zr with Ti, when Zr: Ti ratio becomes 53:47, the PZT transits from rhombohedral to tetragonal, and the polarisation orientation changes from <111> to <100>. Note that although the lattice space group is differently classified, the lattice constant difference between rhombohedral and tetragonal is very small. The boundary between these two phases has been referred to as MPB, but strictly it is a low symmetry transition region. In 2000 Cohen reported that a polarisation rotation mechanism is responsible for the property enhancement at the MPB, where a distorted lattice lowers the free energy barrier causing the polarisation orientation to change more easily. [39] Doping creates distortions in the

lattice by altering the ionic radius, and artificially controls the mobility of domain movements. With A-site doping, such as Sm and La, the free energy of domain structures is high, leading to a remarkably high 800 pC/N piezoelectric coefficient.[40, 41] In contrast, with B-site doping, such as Nb and Mn, domains are stabilised and the loss can be reduced to 1‰.[42]

1.1.3. *Ferroelectric materials in applications*

Next to sonar applications for the military, ferroelectrics are also required in ultrasonography sensors, diesel engine valves, mobile mechanical motors, energy harvesting nanogenerators and printer ink heads, etc. due to their high piezoelectric coefficients.[43-46]

In an inkjet printer, the ink tank is a sealed chamber. The process of printing relies on PZT layers as a piezo element to precisely deform and push ink out of the chamber, to form an ink drop.

In thin film piezo-printheads, PZT is deposited and integrated into a series of micro-electromechanical system (MEMS) devices. In general, the thin films fabrication processes include chemical methods, such as modified chemical vapor depositions (MCVD, atomic layer deposition (ALD)) and sol-gel, or physical methods, such as magnetron sputtering, pulsed laser deposition (PLD) and molecular beam epitaxy (MBE). The PLD process is thoroughly discussed in following session 1.4.1.

The failure and fatigue analysis for PZT piezoelectric membranes in MEMS drew a lot of attention in past decades. For instance, defects in the films caused by strain and thermal stress at interfaces were intensively studied in many researches.[47, 48] For the above applications, thin film PZT or related materials are a requirement. This in turn requires the use of a substrate material, which inevitably imposes stress on the functional piezoelectric, either due to epitaxy or due to a thermal mismatch. To predict these effects on the properties of PZT, several models were developed. In this thesis work, the prediction of a phenomenological model which includes the thermal strain in PZT films, are discussed and an attempt is made to experimentally verify them.

1.2. From Landau theory to Vergeer’s model

1.2.1. *Phenomenology*

Landau and Ginzburg first established a mathematical physical model (LG equation) in the 1950s, which was for computing the system free energy in a superconductivity secondary phase transition.[49, 50] An order parameter is used in this LG equation to describe the symmetry state of the system. Since ferroelectrics are similar to ferromagnetic systems in many thermodynamic aspects, this order parameter (which is density of superconducting electrons from original LG equation), can then be replaced by polarisation (*P*) to describe a dipolar system as mentioned by Devonshire in "*Theory of Ferroelectrics*".[51]

The Landau-Ginzburg-Devonshire (LGD) thermodynamic model of ferroelectric materials presents a tool to successfully analyse ferroelectric phase transitions and domain pattern formation in bulk materials, especially in well-ordered single crystals. In ferroelectric thin films, multiple extrinsic effects play an important role that have been neglected in the general LGD equation. Limiting the discussion to epitaxially grown films, the ferroelectric structure consists of multiple domains, separated by domain walls. The film is usually under substrate induced thermal strain, and domain wall motion under the influence of an applied field contributes significantly to the ferroelectric and piezoelectric properties of the film.

1.2.2. *Three-domain model and functional properties predictions*

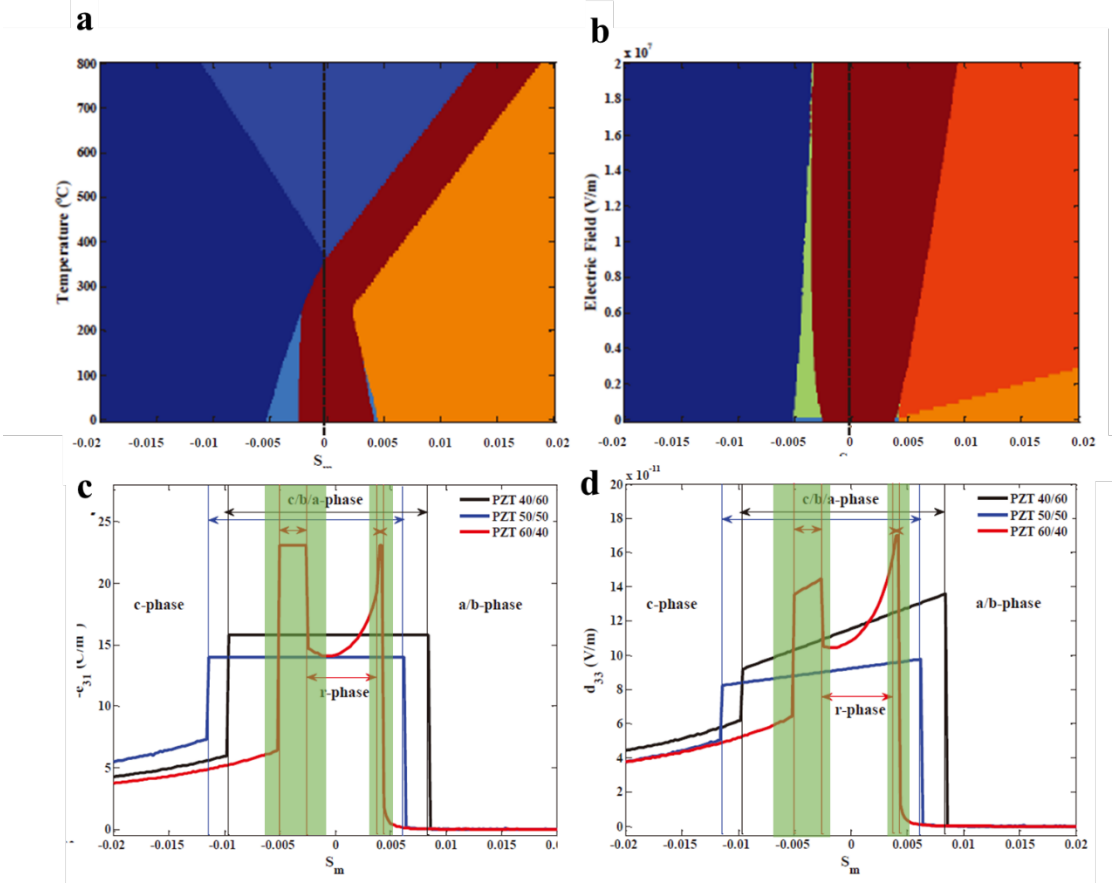

Figure 1.3. *a and b are the computed phase diagrams that temperature and electric field against thermal misfit strain, respectively. c and d are the calculated* e_{31} *and* d_{33} *of PZT(x=0.6) against thermal misfit strain, respectively.*

Houwman et al. developed the so-called a 'three-domain model' based on earlier work by Khukar, Pertsev et al., what is considered as a 'two-domain' model.[3, 52-54] In the three-domain model additional boundary conditions were applied to the formalism of Khukar et al. which led to a more realistic model for clamped films. Early experimental work on films with tetragonal composition PZT(x=0.4) supported the applicability of the model.[3] The three-domain model connects domain wall motion, external elastic and electric field to intrinsic ferroelectric and piezoelectric properties of a clamped films.[3] Using this model, Vergeer produced

a set of predictions for the piezoelectric behaviour and crystal symmetry transitions as function of the substrate misfit strain due to thermal expansion mismatch for different compositions.[4] In the present experimental study, we make an attempt to validate this model. The approach we used is to determine the temperature dependence of the structural and piezoelectric properties of thin films, with different strain states, grown on different substrates and compare them to the values found by the model. Following is a detailed description of the methods used.

1.3. Strain engineering

One of the major methods used to change thin film symmetry and properties is to tune the strain in epitaxial thin films. The deposition process takes place on a substrate at a temperature higher than 25 °C in PLD, to form the oxygen octahedra network through the interface between thin films and the substrate. Therefore, the lattice parameters from the substrate can be imprinted into the film's growth upon it, which introduces misfit strains and stress in the heteroepitaxial thin films.

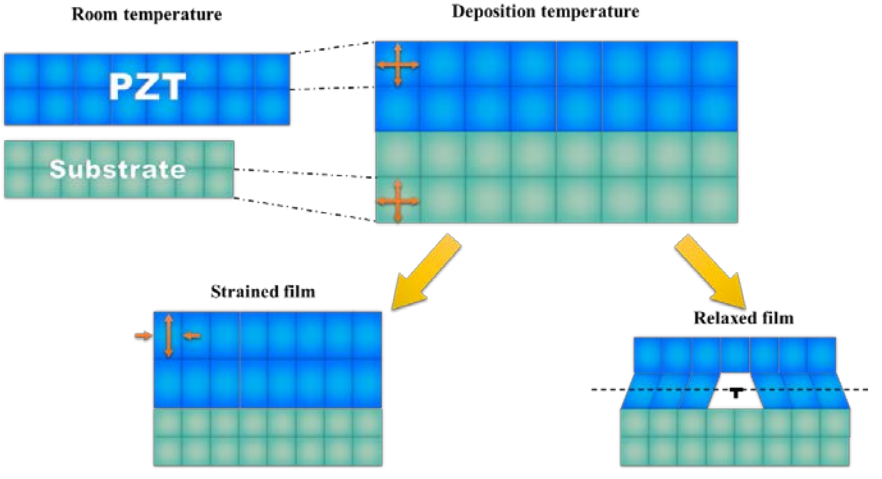

Figure 1.4. *The schematic of strained thin film and relaxed thin film with a dislocation.*

For example, a coherently strained, epitaxial film of $BiFeO_3$ can endure up to 6%

$$S_{strain\ misfit}^{Epitaxial} = \frac{a_{substrate} - a_{thin\ film}}{a_{substrate}} \quad (1.1)$$

compressive bi-axial in-plane misfit strain up to approximately a maximum of 50 nm thickness. The tilting in O-B-O bonds angles and deformation in oxygen octahedral cages can occur, but relaxation in a thicker film restores the bulk lattice parameters. Thus, we define epitaxial misfit strain to be the strain calculated based on the lattice constant difference between the film material in bulk at room temperature and the substrate materials in bulk at room temperature.

As mentioned previously, the films are cubic on cubic deposited on the substrate at a temperature hundreds Celsius degrees higher than room temperature. Consequently, thermal expansion in films and the substrate has to be considered to play a role here. In contrast with the epitaxial misfit strain, in this work, we define the thermal misfit strain to be based on the lattice constant difference between the film materials in bulk at deposition temperature and the substrate material in bulk at deposition temperature. Therefore, the thermal misfit strain is mainly caused by the thermal expansion coefficient (CTE) difference between the film and the substrate and can be described in the equation as following:

$$S_{misfit(RT)}^{Thermal} = -\Delta T\left(< \alpha_{substrate} > - < \alpha_{thin\ film} >\right) \quad (1.2)$$

Where *S* stands for the misfit strain, *T* stands for the temperature difference, α is the CTE.

1.4. Experimental section

We produced the thin film samples with (Pulsed laser deposition)PLD process, and characterised the PZT films with temperature dependent X-ray reciprocal space mapping (RSM) and grazing incidence diffraction (GI-XRD), transmission electron microscopy (TEM). This was in bright field (BF) and dark field (DF) modes as well as selected area diffraction (SEAD) and piezoresponse force microscopy (PFM). The Zr/Ti ratio has been confirmed by Rutherford Backscattering Spectrometry (RBS). The PZT(x=0.6) film which in bulk has a rhombohedral lattice symmetry, is at room temperature on STO, which is first time this has been observed for this composition. Some of the major characterisation techniques are introduced as following in the experimental section.

1.4.1. Pulsed laser deposition(PLD)

It cannot be more proper to describe Pulsed Laser Deposition (PLD) as "… a rare thing for a newly discovered (or rediscovered) synthesis technique to immediately deliver both enhanced performance and simplicity in a field of accelerating interest."[55] In 1969, Hass and Ramsey found that a pulsed laser can be used as an energy source for evaporative deposition to produce thin films. However, despite nearly 20 years of limited progress, PLD has been recognised to have several merits.

In the late 1980s, the American navy and NASA sought reproducible high temperature superconducting (HTS) thin films $YB_2Cu_3O_{7-X}$ for several cutting-edge applications. (i.e., Vertical Josephson junctions, high Q microwave resonators for navy satellites or high efficiency bolometers for the Cassini mission). However, the stoichiometry in the multi-composition oxide film was difficult to preserve by sputtering. The molecular beam epitaxy (MBE) process was too slow for large scale production and the crystalline quality achieved by the sol-gel process was too poor to meet the application requirements. In 1987, T. Venkatesan et al. first applied the PLD process with a 248 nm wavelength commercially available laser to produce reliable, high-quality HTS thin films from a bulk material.[56, 57] With 10Hz repetition rate, a deposition rate of 1nm per 1 second was achieved. Heterojunction devices (Josephson junctions) were later tested by John Clarke in a Superconducting

Quantum Interference Device (SQUID), and the device showed the lowest flux noise compared with other reports in that period, which demonstrated the advantages of PLD among other process.[58, 59]

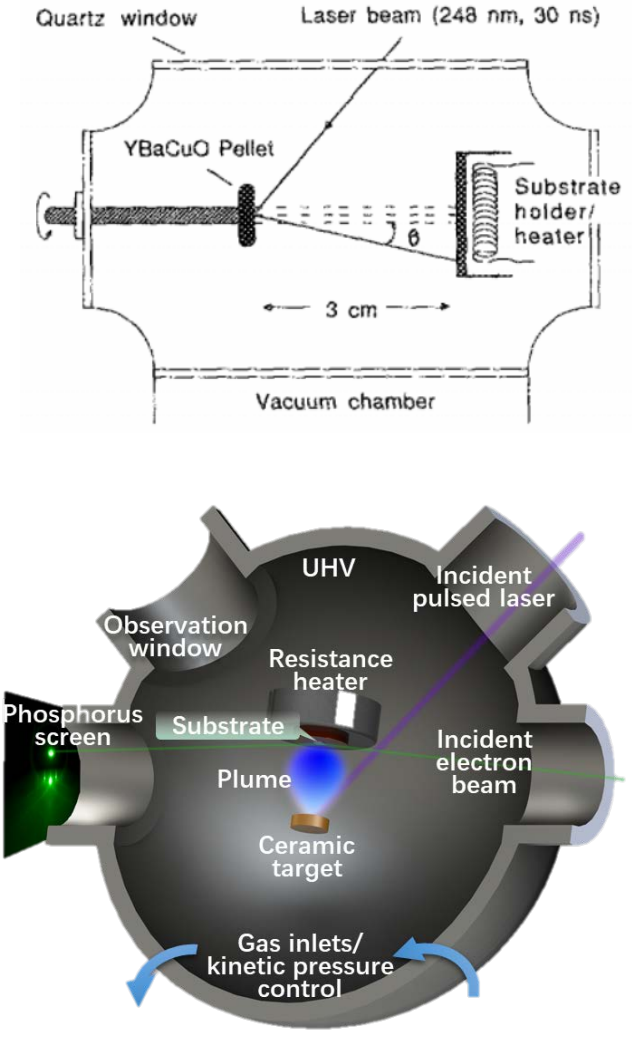

Figure 1.5. *The top panel is the early age schematic of the concept of PLD. [57] The bottom panel is the modern schematic of PLD.*

Now, good quality complex oxides thin films, simple oxides thin films and metal electrodes have all been successfully deposited by PLD. In benefits of the reflection high-energy electron diffraction (RHEED), the physicists can use PLD to artificially

fabricate desired atomic level layered structures or heterostructure interfaces.[60-62] Si-based high-quality thin film devices made by PLD have shown to be promising for large scale industrial manufacturing.[63]

The tuneable deposition parameters in PLD systems are incident laser fluence (energy density), deposition temperature, repetition rate, gas pressure and the distance between sample and target.

Oxygen pressure seems to be a simple parameter, but in fact it is directly related to one of the most common issues in PLD thin films. the oxygen vacancies. Despite the promise of preserving stoichiometry from a ceramic target, in principle, there should be no need for excess oxygen from another supply in the PLD process. However, in practice the oxidation process in the plume is rarely fully effective. For $SrFeO_3$ deposition, for instance, ozone is essential for oxidising Fe to 4^+ valence.[23] Meanwhile, gas pressure at a certain level confines the plume, reduces the kinetic energy of ions and molecular clusters, and provides the environment for oxidisation. One solution to remove the oxygen vacancies in a sample, is to post-annealing the sample with a higher oxygen pressure. This additional procedure has been proven very important for the prevention of leakage in ferroelectrics.

Deposition temperature determines the surface mobility of ions and molecular clusters mobility on the substrate. Sufficient mobility of ions can result in high crystalline films with an atomic flat surface. Although a high deposition temperature is preferred in many cases, as it is favourable for the crystallinity, there are several materials that are sensitive to temperature. For example, La above 850°C, Bi above 650°C and Pb above 600°C are known to be volatile elements which may cause non-stoichiometry in sample films. (This critical temperature for volatility also depends on oxygen pressure).[64]

In this work the deposition temperature is one of the major concerns that introduce thermal strain in PZT and this parameter is discussed in detail in the previous section 1.3.

1.4.2. Scanning probe microscopy (SPM)

SPM is a probe stage or a characterisation platform, by changing the probe and screening over sample, SPM can provide information about different specimen properties with an atomic resolution. Here we only discuss atomic force microscopy (AFM) and other measurement modules based on AFM.

Sample topography information is scanned by a probe tip. The height changes of the sample surface affect the tip through a compitition between an attractive and a repulsive Van der Waals forces. The forces cause a height changing and torque distortion in the cantilever. A laser is reflected by the cantilever top surface and lays a spot on a four segmented photodetector with a lateral resolution to detect the spot displacements. Distinguish from contact mode directly move tip on the sample surface, tapping mode is used in this thesis for a better probe preservation. As shown in Fig.1.6 top panel, a certain frequency AC drives resonance cantilever only engages sample surface from point to point with a set distance. It is extremely useful in this thesis work to check the surface of substrate before deposition and the nature of the substrates as showing in Fig. 1.7 a and e.

The regular probe tip radius is 10-25nm, which decides the minimum resolution of specimen surface feature is larger than 10nm.

It is extremely critical to recognise that PFM is active to all electromechanical coupling, which is an underlying functionality has been widely observed in large biological or organic cluster molecules, piezoelectric and ferroelectrics, for instance.

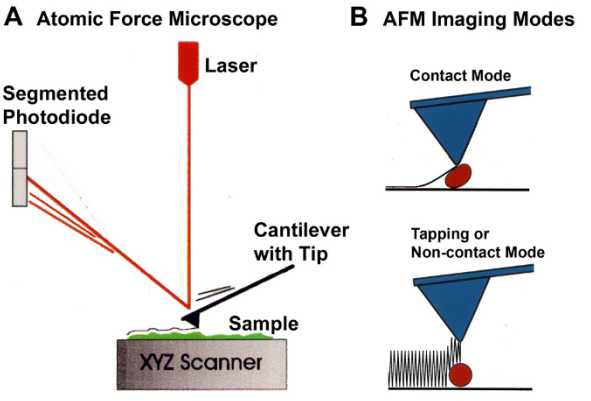

Figure 1.6. *Top panel is the schematic of AFM in contact mode in contrast with tapping mode.[66]*

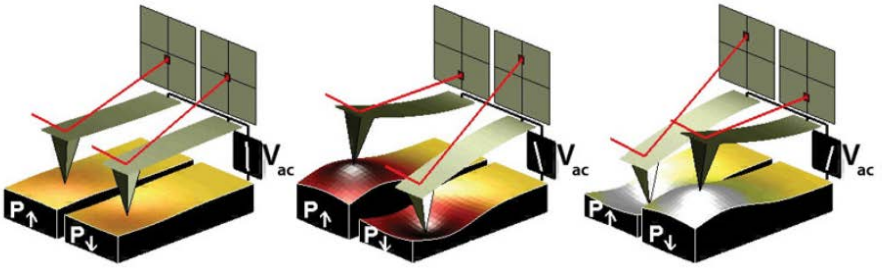

Figure 1.7. *A series of illustrations vertical polarised multi-domains detected by PFM with an applied voltage.[67]*

In conventional vertical PFM measurements, a DC is directly applied on the sample surface via a conductive tip and this results in a mechanical deformation in the sample. This effect between external electric stimulates and mechanical responses is described as inverse piezo-effect, also known as a rank-3 tensor d_{33}. The magnitude of d_{33} is therefore proportional to the magnitude at the oscillating frequency, since the cantilever driving voltage at a contact resonance frequency is desired to amplify the displacement amplitude in photodetector by an external lock-in amplifier. This modification enhances the small signal/noise ratio in weak piezoelectric/ferroelectrics, but sometimes it can also create a misguided false spontaneous polarisation in some non-polarised materials, such as an amorphous glass. This sort of illusions is caused by surface charge accumulation which can be

distinguished by two different stiffness probes or by KFPM.

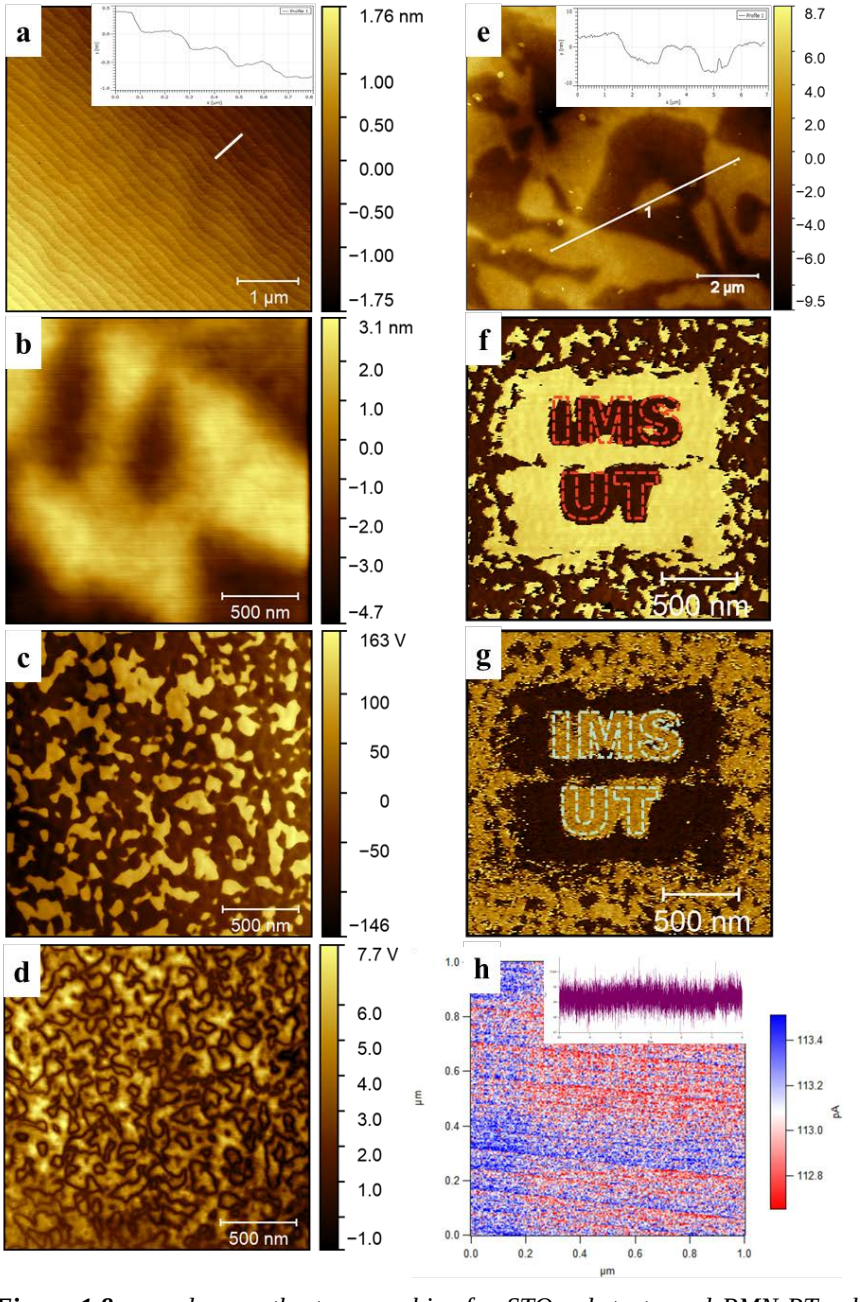

Figure 1.8. *a and e are the topographies for STO substrate and PMN-PT substrate, respectively. The insert plot in each graph is height profile, where a shows the trace on*

the top surface of treated STO and e shows 4-5 nm difference in height between different PMN-PT domains. b, c, d show the same scanning area of PZT on PMN-PT substrate. b is the height information, c is PFM phase channel and d is PFM amplitude. b shows the ferroelectric domains from PMN-PT is 500nm size, while c and d show the PZT thin film ferroelectric domains size is approximate 200nm. f and g are lithography by PFM on the rhombohedral PZT thin film. f is out-plane phase information while g gives the in-plane phase information. h is CAFM scanning result on a PZT thin film, shows no leakage current but only noise.

Vertical PFM is used to distinguish the ferroelectric domains from PZT thin film and PMN-PT substrate as shown in Fig. 1.7 b and c. The ferroelectric domains in PZT have a 200nm radius which is much smaller than PMN-PT, and it is the confirmation of a good ferroelectric quality PZT thin film on ferroelectric PMN-PT. Lithographed rhombohedral PZT thin film shows a relationship between out-plane phase (Fig. 1.7 f) and in-plane phase (Fig. 1.7 g), verifying that each of the polarisation of ferroelectric domain contains two components of dipole vectors, which a tetragonal phase cannot show.

To extract the effective d_{33} value from a sample, ideally a high quality factor (Q) along with the magnitude of amplifier at (or near) resonance frequency is sufficient. However, in practice the contact between probe tip and sample surface is not stable during the scan, because of elastic modulus, tip sharp and sample topography issues, this instability consequently leads to a constantly changing in resonance frequency.

In this thesis some of quantitively measurements parts were not available during the PFM measurements, but an alternative was available that by measuring the sample and a known d_{33} standard sample as a reference. This way can neglect the effects by the tip from sample to sample since the probe was intentionally kept the same. The measurements were taken by one touching down (point-shoot) from one pixel to another pixel, which removes the concern of the fluctuating resonance frequency that would be caused by a dynamic contact mode scan. During imaging, phase channel from PFM results gives the direction information (downwards or upwards) of the domain polarisation, while the amplitude channel gives the boundary information where the domain polarisations changes, and these boundaries are described as domain walls.

Conductive AFM (CAFM) is also used in this thesis to discover the conductivity of dislocations, defects and domain walls as presented in Fig. 1.7 h. The details will be thoroughly discussed in chapter 5.

1.4.3. Crystalline quality and symmetry characterisation

For crystalline quality and symmetry characterisation in this thesis, X-ray diffraction (XRD) is used. XRD is one non-destructive microstructure reciprocal space determination method for bulk materials and its experimental setup is given as follows:

The strong kinetic energy electron beam (generated by tungsten filament) hits the cathode (usually Cu for small lab setups) and excites X-ray (wavelength approximate 1.5406Å). Therefore, for single crystals characterisations, monochromators are better than Ni filter, to remove the resident peaks from the source, such as tungsten peak, K_α peak and K_β peak. The X-ray goes through shutter, divergence slit (DS), Soller slits (SS), a series of height(length)-limiting slits (IS) and a Ge monochromator (220 orientation) to reach the sample stage. On the receiving end, optionally the X-ray can go through a secondary limiting slits (RS), another SS and a secondary monochromator on the arm before incident into the detector. All these optical units aim to provide a coherent, parallel X-ray with a limited spot size on the sample. The detectors can be classified as 0d detector (point or scintillation detector), 1d detector (line detector) and 2d detector (area detector). In additional to the incident ω, the sample rotation is one Euler angle as defined as φ, and another Euler angle is χ as all showing in Fig. 1.8 b.

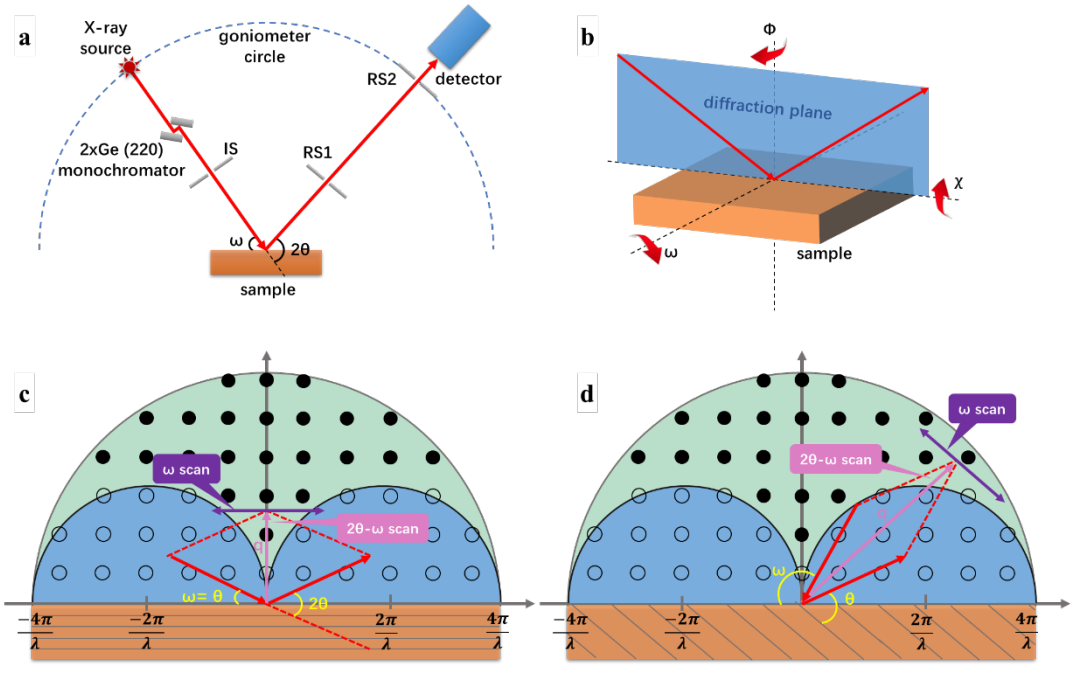

Figure 1.9. *a shows the schematic of XRD optical path from X-ray source to the detector. b illustrates all Euler angles in respect with the diffraction plane. Figure c and d are Ewald constructions showing the scattering geometry in symmetrical (c) and asymmetry (d), the pink arrows indicate 2θ-ω scan direction and purple arrows are ω scan direction. The grey lines in the orange sample stands for crystal planes. Only the scatterings in the light green area can be measured and light blue area is only possible for transmission in ordinary geometry.*

The characterisation in this thesis by high resolution XRD (HR-XRD) is intended to investigate the symmetry of sample crystalline. The position and width of X-ray reflexes are measured while the rotation of the sample around a Euler angle or the changing position of detector. Fig. 1.9 c and d show the scattering geometry for a symmetrical and asymmetrical single scan, individually, along with two scan directions. These two directions in this thesis are referring to 2θ-ω scan (θ/2θ scan in symmetry scan and 2θ-ω scan in asymmetry) and ω scan.

φ scan is used in this thesis to estimate the in-plane epitaxial relationship between in PZT thin film and CaF_2 substrate. By rotating the sample 360° in φ direction, while the ω and 2θ are kept constant, the asymmetric reflexes (110) of PZT and (220) of

CaF_2 show four peaks in each individual scan, but with 45° difference between these two scans.

For two-dimensional region scan mapping of reciprocal space (RSM), 1d detector (Panalytical Pixel) is used in this thesis, which means the diffraction intensity is achieved within a 2θ range in ω steps. A larger diffraction plane index shows a larger separation between reflections as Fig. 1.10 d indicts. Thus, in this thesis, two RSMs for PZT (103) plane and (204) plane in Fig. 1.10 c is presented to give support for an idea why (204) RSM is then used for further domain investigation.

Temperature dependent XRD is achieved by changing the sample stage temperature (Anton Paar 900DS), then perform the 2θ-ω scan or RSM at each temperature point as showing in Figure a.

X-ray diffraction with grazing incidence and/or exit angles contains both diffraction and reflection effects. If the incident angles are slightly larger than a critical angle, reflections from sample interfaces interfere with each other and occur interference fringes. [68] Those interference effects measurements are referred to as X-ray reflectivity (XRR) and used to determine the roughness and thickness of thin films in this thesis.

In contrast if the grazing incident angle is smaller than a critical angle α_c:

$$\alpha_c = \frac{N_A r_e \rho Z \lambda}{\pi A} \tag{1.3}$$

Where the N_A is Avogadro number, r_e is the electron radius, ρ is the density, Z is element number, λ is incident wavelength and A is average atom weigh. In this condition, the surface Bragg scattering is remarkably enhanced as the incident beam penetration depth is limited and described as L: [69]

$$L = \frac{\lambda}{2\pi[2(1-n)-sin^2\,\alpha_i]^{1/2}} \tag{1.4}$$

As n is the refraction index, α_i is the incident angle. In this thesis the grazing incidence diffraction (GI-XRD) was employed on PZT film that grew on STO

substrate, therefore the approximate critical angle is 0.23° at 8kV given by the equation. One type of GI-XRD is co-planar extremely asymmetric diffraction (EAD) which aims to measure the top layer out-plane structural information by either the incident or the exit angle near the critical angle. It generally faces difficulty in thin films with X-ray lab source, thus the other geometry of Bragg-Laue diffraction, extremely non-coplanar geometry, is used in this thesis to study the crystal structure changing against thin film thickness as shown in Fig. 1.10 b. Since this geometry requires both incident angle and one Euler angle changes during the measurement simultaneously, Bruker D8 2d detector was used to easier find diffraction peak position.

The interpretation of XRD or RSMs data relies on the Bragg equation. For 2θ-ω scan, the diffraction equation can be described as follows:

$$2d_{hkl}sin\theta = n\lambda \tag{1.5}$$

Where d_{hkl} is d-space between two diffraction planes, n is integer and λ is the wavelength of X-ray. In many cases, while the ω is equal to θ, the reflexes are on the [001] axis and labelled as q_c, these scans are symmetrical. In other occasions, the ω differs from θ with an offset angle, that is asymmetrical scans, as showing in Fig. 1.10e. [70] The component of the scattering vectors in asymmetry RSMs is perpendicular to the measured crystal plane, which is labelled q_a. while the component that parallel to the crystal plane, is q_c, then it gives:

$$q_c = 2\pi[cos(2\theta - \omega) - cos\omega]/\lambda \tag{1.6}$$

$$q_a = 2\pi[sin(2\theta - \omega) + sin\omega]/\lambda \tag{1.7}$$

With three independent asymmetric RSMs, it is possible to plot the thin films and substrate Bragg spots in 3-dimension HKL reciprocal space as Fig. 1.10 f. [71] This technique is used in this thesis to reveal the rich ferroelectric domains information of PZT.

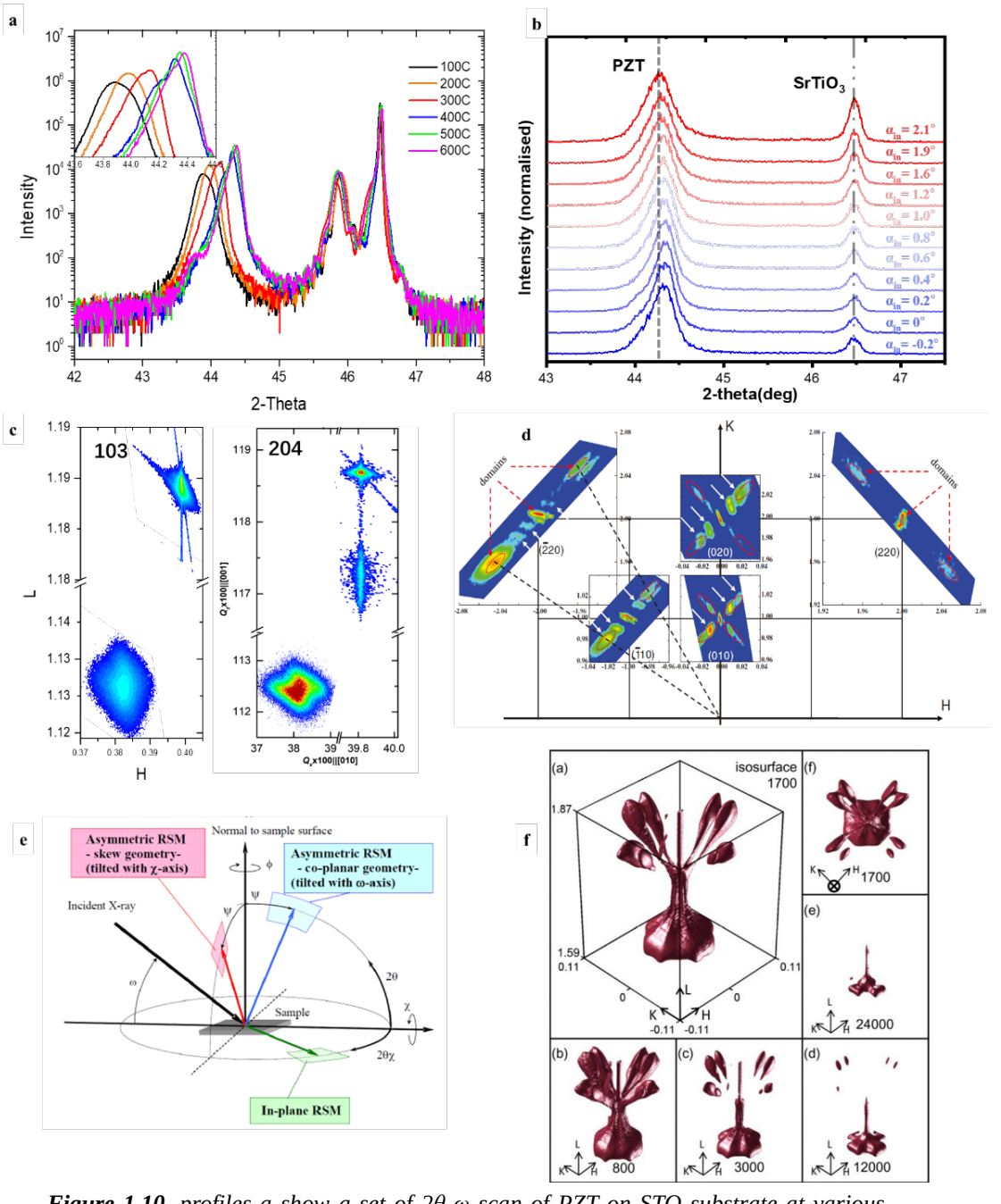

Figure 1.10. *profiles a show a set of 2θ-ω scan of PZT on STO substrate at various temperature. Insert plot is magnifiction of 2-theta of PZT diffraction peak. Figure b is*

the GI-XRD for PZT (200) Bragg peak with changing of incident angle. The left plot in c shows (103) RSM of PZT and STO substrate while the right panel shows (204). d is the schematic shows the relationship among different indexes in reciprocal space. Figure c illustrates the concept of two-dimensional mapping correspond with real space Euler angles and d shows an example of three-dimensional Bragg peak for $BiFeO_3$ tetragonal and rhombohedral domains.[70, 71]

1.5. The aims and the layout of this thesis

This project is based on Houwman three-domain model, and its extension to Vergeer's phenomenological model. Vergeer et al. have given a series of predictions, which have different Zr/Ti ratio PZT's piezoelectric and ferroelectric response against temperature.[3, 4, 65] The aim of this project is to formulate a feasible strategy and experimentally prove those predictions. Moreover, since the PZT is used and studied in actuators due to its high piezoelectric effect, the piezoelectric response is of particular interest, measured and discussed.

With this work, we experimentally demonstrate the applicability of the a three-domain model to strained thin films, and reveal the relationship between piezoelectric properties and thermal misfit strain. This knowledge optimises the piezoelectric performance by engineering the desired crystalline structure of the film along with a cooling procedure, which is important for many deposition processes, such as PLD. Moreover, expected RSM for different symmetries are mathematically and systematically described. This information would be helpful for the symmetry distinguishing.

In the later chapters, we focus on the solution of the leakage in the PZT thin films. A free-standing ionic gel was used as a dielectric layer to gate PZT. Ferroelectric domains were confirmed to be switched by gel induced electrostatic-field along with the depolarisation field. Furthermore, this ionic gel gated transistor was used to observe the single c-domain polarisation switching in tetragonal PZT. Interestingly, we found a ferroelastic switching from c-domain to a-domain during the polarisation switching, and anisotropic in-plane domains formation, which suggests anisotropy strain may be attributed by the bottom electrode layer $SrRuO_3$ (SRO). Although this knowledge deepened the fundamental understanding of ferroelectric domain switching and enabled many applications in flexible and leaky ferroelectric thin films, further research is still required.

This thesis consists of six chapters, involving one introduction containing overall background and motivation for the used techniques, four research chapters with results and discussions, followed by one chapter for the summary.

Chapter 1 is the background and introduction for this thesis.

Chapter 2 discusses the three-domain model and its following application calculations, several important conclusions were reviewed and presented. The strategy of experimentally falsifying the calculated predictions is explained. Si based PZT sample preparation is described. A 4-point bending set-up was attempted to determine transversal piezoelectric charge coefficient e_{31} from the PZT sample surface. Finite element analysis is also used for stress and strain simulation.

Chapter 3 mathematically discusses the ferroelectric domain peaks in reciprocal space. Tetragonal, rhombohedral and monoclinic A-type and C-type are addressed individually. The expected diffraction projections of five lattice symmetries in (001), (110) and (111) planes, respectively, and in comparisons with real measuremnts, are given in the end.

Chapter 4 focuses on the experimental validation of the predictions made by Vergeer's model centred on a series of temperature dependent RSMs. The differences in PZT RSM domain patterns among samples on varied CTE substrates, successfully validate the phenomenological predictions. For further supporting symmetry analysis in lattice scale, (Transmission electron microscopes) TEM and (Selected Area Electron Diffraction) SEAD results are addressed and discussed at the end of this chapter.

Chapter 5 concentrates on the solution of leaky ferroelectric thin films. The ionic gel assisted ferroelectric switching processing was validated by PFM. A tetragonal mono c-domain PZT film was used to test the maxium gating voltage and studied its swithing dynamic process.

Chapter 6 summarises the conclusions in this thesis and makes suggestions for further research.

Reference:

1. Valasek, J., *Piezo-electric and allied phenomena in Rochelle salt.* Physical review, 1921. **17**(4): p. 475.
2. Valasek, J., *The early history of ferroelectricity.* Ferroelectrics, 1971. **2**(1): p. 239-244.
3. Houwman, E., et al., *Modelling functional properties of ferroelectric oxide thin films with a three-domain structure.* arXiv preprint arXiv:1901.10883, 2019.
4. Vergeer, K., *Structure and functional properties of epitaxial PBZRxTI1-xO3 films.* 2017.
5. Debye, P., *Zur theorie der spezifischen wärmen.* Annalen der Physik, 1912. **344**(14): p. 789-839.
6. Von Hippel, A., *Ferroelectricity, domain structure, and phase transitions of barium titanate.* Reviews of Modern Physics, 1950. **22**(3): p. 221.
7. Schrodinger, E., *Studien uber Kinetik der Dielektrika, den Schmelzpunkt, Pyro-und Piezoelektrizitat.* Sitzungsberichte der kaiserlichen Akademie der Wissenschaften in Wien. Mathematisch-naturwissenschaftliche Klasse (IIa), 1912. **121**: p. 1937-1972.
8. Valasek, J., *Piezo-electric activity of Rochelle salt under various conditions.* Physical Review, 1922. **19**(5): p. 478.
9. Kanzig, W., *History of ferroelectricity 1938-1955.* Ferroelectrics, 1987. **74**(1): p. 285-291.
10. Newnham, R. and L.E. Cross, *Ferroelectricity: The foundation of a field from form to function.* MRS bulletin, 2005. **30**(11): p. 845-848.
11. Pohanka, R.C., P.L. Smith, and G. Haertling, *Recent advances in piezoelectric ceramics.* Electronic Ceramics—Properties, Devices and Applications, 1987.
12. Ginzburg, V., *Some remarks on ferroelectricity, soft modes and related problems.* Ferroelectrics, 1987. **76**(1): p. 3-22.
13. Megaw, H.D., *Crystal structure of barium titanate.* Nature, 1945. **155**(3938): p. 484-485.
14. Jaffe, B., W. Cook, and H. Jaffe, *The piezoelectric effect in ceramics.* Piezoelectric Ceramics, 1971: p. 7-21.
15. Shirane, G. and A. Takeda, *Phase transitions in solid solutions of PbZrO3*

and PbTiO3 (I) small concentrations of PbTiO3. Journal of the Physical Society of Japan, 1952. **7**(1): p. 5-11.

16. Shirane, G., K. Suzuki, and A. Takeda, *Phase transitions in solid solutions of PbZrO3 and PbTiO3 (II) X-ray study.* Journal of the Physical Society of Japan, 1952. **7**(1): p. 12-18.
17. Shirane, G. and K. Suzuki, *Crystal structure of Pb (Zr-Ti) O3.* Journal of the Physical Society of Japan, 1952. **7**(3): p. 333-333.
18. Jaffe, B., W. Cook, and H. Jaffe, *Piezoelectric ceramics, 101 London*. 1971, Academic Press.
19. Berlincourt, D., C. Cmolik, and H. Jaffe, *Piezoelectric properties of polycrystalline lead titanate zirconate compositions.* Proceedings of the IRE, 1960. **48**(2): p. 220-229.
20. Jaffe, B., R. Roth, and S. Marzullo, *Piezoelectric properties of lead zirconate-lead titanate solid-solution ceramics.* Journal of Applied Physics, 1954. **25**(6): p. 809-810.
21. Corker, D., et al., *A neutron diffraction investigation into the rhombohedral phases of the perovskite series.* Journal of Physics: Condensed Matter, 1998. **10**(28): p. 6251.
22. Noheda, B., et al., *A monoclinic ferroelectric phase in the Pb (Zr 1− x Ti x) O 3 solid solution.* Applied physics letters, 1999. **74**(14): p. 2059-2061.
23. Alberta, E., R. Guo, and A. Bhalla, *Structure–property diagrams of ferroic solid solutions. Part I: Perovskite relaxor ferroelectrics with morphotropic phase boundaries.* Ferroelectrics Review, 2001. **4**: p. 1-327.
24. Royen, P. and K. Swars, *Das System Wismutoxyd-eisenoxyd im bereich von 0 bis 55 Mol% eisenoxyd.* Angewandte Chemie, 1957. **69**(24): p. 779-779.
25. Inbar, I. and R.E. Cohen, *Origin of ferroelectricity in LiNbO3 and LiTaO3.* Ferroelectrics, 1997. **194**(1): p. 83-95.
26. Ding, R., X. Zhang, and X.W. Sun, *Organometal trihalide perovskites with intriguing ferroelectric and piezoelectric properties.* Advanced Functional Materials, 2017. **27**(43): p. 1702207.
27. Jain, P., et al., *Switchable electric polarization and ferroelectric domains in a metal-organic-framework.* Npj Quantum Materials, 2016. **1**(1): p. 1-6.
28. Ye, H.-Y., et al., *Metal-free three-dimensional perovskite ferroelectrics.* Science, 2018. **361**(6398): p. 151-155.

29. Denoyer, F., R. Comes, and M. Lambert, *Anisotropic critical X-ray diffuse scattering from NaNbO3 crystals.* Solid State Communications, 1970. **8**(23): p. 1979-1981.
30. Denoyer, F., et al., *Inelastic neutron scattering study in cubic NaNbO3.* Solid State Communications, 1976. **18**(4): p. 441-444.
31. Park, S.-E. and T.R. Shrout, *Ultrahigh strain and piezoelectric behavior in relaxor based ferroelectric single crystals.* Journal of Applied Physics, 1997. **82**(4): p. 1804-1811.
32. Bokov, A. and Z.-G. Ye, *Recent progress in relaxor ferroelectrics with perovskite structure.* Journal of materials science, 2006. **41**(1): p. 31-52.
33. Li, F., et al., *The origin of ultrahigh piezoelectricity in relaxor-ferroelectric solid solution crystals.* Nature communications, 2016. **7**(1): p. 1-9.
34. Li, F., et al., *Ultrahigh piezoelectricity in ferroelectric ceramics by design.* Nature materials, 2018. **17**(4): p. 349.
35. Li, F., et al., *Giant piezoelectricity of Sm-doped Pb (Mg1/3Nb2/3) O3-PbTiO3 single crystals.* Science, 2019. **364**(6437): p. 264-268.
36. Takahashi, H., et al., *Piezoelectric properties of BaTiO3 ceramics with high performance fabricated by microwave sintering.* Japanese journal of applied physics, 2006. **45**(9S): p. 7405.
37. Shulman, H.S., et al., *Microstructure, electrical conductivity, and piezoelectric properties of bismuth titanate.* Journal of the American Ceramic Society, 1996. **79**(12): p. 3124-3128.
38. Zheng, H., et al., *Effects of octahedral tilting on the piezoelectric properties of sr-doped lead zirconate titanate.* Ferroelectrics, 2002. **268**(1): p. 125-130.
39. Fu, H. and R.E. Cohen, *Polarization rotation mechanism for ultrahigh electromechanical response in single-crystal piezoelectrics.* Nature, 2000. **403**(6767): p. 281-283.
40. Kong, L.B., et al., *Ferroelectric ceramics (I).*
41. Gao, B., et al., *Unexpectedly high piezoelectric response in Sm-doped PZT ceramics beyond the morphotropic phase boundary region.* Journal of Alloys and Compounds, 2020. **836**: p. 155474.
42. Singh, V., et al., *Effect of lanthanum substitution on ferroelectric properties of niobium doped PZT ceramics.* Materials Letters, 2006. **60**(24): p. 2964-2968.

43. Park, K.-I., et al., *Piezoelectric BaTiO3 thin film nanogenerator on plastic substrates.* Nano letters, 2010. **10**(12): p. 4939-4943.
44. Muralt, P., et al., *Piezoelectric micromachined ultrasonic transducers based on PZT thin films.* IEEE transactions on ultrasonics, ferroelectrics, and frequency control, 2005. **52**(12): p. 2276-2288.
45. Mulvihill, M.L., et al., *Cryogenic cofired multilayer actuator development for a deformable mirror in the Next Generation Space telescope.* Journal of electroceramics, 2002. **8**(2): p. 121-128.
46. Muralt, P., et al., *Fabrication and characterization of PZT thin-film vibrators for micromotors.* Sensors and Actuators A: Physical, 1995. **48**(2): p. 157-165.
47. Bahr, D., et al., *Defects and failure modes in pzt films for a mems microengine.* MRS Online Proceedings Library, 2000. **657**(1): p. 441-446.
48. Robinson, M. and D. Bahr, *Failure strains in micromachined piezoelectric membranes.* Strain, 2009. **45**(1): p. 55-62.
49. Landau, L., *The intermediate state of supraconductors.* Nature, 1938. **141**(3572): p. 688-688.
50. Ginzburg, V., *ZhETF 15, 739 (1945).* Journ. Phys. USSR, 1946. **10**: p. 107.
51. Devonshire, A., *Theory of ferroelectrics.* Advances in physics, 1954. **3**(10): p. 85-130.
52. Bartasyte, A., et al., *Stability of the polydomain state in epitaxial ferroelectric PbTiO 3 films.* Applied Physics Letters, 2008. **93**(24): p. 242907.
53. Koukhar, V., N. Pertsev, and R. Waser, *Thermodynamic theory of epitaxial ferroelectric thin films with dense domain structures.* Physical Review B, 2001. **64**(21): p. 214103.
54. Kukhar, V., et al., *Polarization states of polydomain epitaxial Pb (Zr 1− x Ti x) O 3 thin films and their dielectric properties.* Physical Review B, 2006. **73**(21): p. 214103.
55. NORTON, D.R., *Pulsed Laser Deposition of Complex Materials: Progress.* Pulsed laser deposition of thin films: applications-led growth of functional materials, 2007: p. 1.
56. Dijkkamp, D., et al., *Preparation of Y-Ba-Cu oxide superconductor thin films using pulsed laser evaporation from high T c bulk material.* Applied

Physics Letters, 1987. **51**(8): p. 619-621.
57. Venkatesan, T., et al., *Observation of two distinct components during pulsed laser deposition of high T c superconducting films.* Applied physics letters, 1988. **52**(14): p. 1193-1195.
58. Clarke, J. and A.I. Braginski, *The SQUID handbook*. Vol. 1. 2004: Wiley Online Library.
59. Ferrari, M., et al., *Low magnetic flux noise observed in laser-deposited in situ films of YB 2 Cu 3 O y and implications for high-T c SQUIDs.* Nature, 1989. **341**(6244): p. 723-725.
60. Koster, G. and G. Rijnders, *In situ characterization of thin film growth*. 2011: Elsevier.
61. Chen, B., et al., *Spatially Controlled Octahedral Rotations and Metal–Insulator Transitions in Nickelate Superlattices.* Nano letters, 2021. **21**(3): p. 1295-1302.
62. Liao, Z., et al., *Controlled lateral anisotropy in correlated manganite heterostructures by interface-engineered oxygen octahedral coupling.* Nature materials, 2016. **15**(4): p. 425-431.
63. Groenen, R., et al., *Epitaxial growth of complex oxides on silicon by enhanced surface diffusion in large area pulsed laser deposition.* arXiv preprint arXiv:1607.05955, 2016.
64. Wu, M., et al., *Asymmetric response of electrical conductivity and V valence state to strain in cation-deficient Sr1–yVO3 ultrathin films based on absorption measurements at the V L2-and L3-edges.* Journal of synchrotron radiation, 2019. **26**(5): p. 1687-1693.
65. Nguyen, M.D., et al., *Misfit strain dependence of ferroelectric and piezoelectric properties of clamped (001) epitaxial Pb (Zr0. 52, Ti0. 48) O3 thin films.* Applied physics letters, 2011. **99**(25): p. 252904.
66. Hansma, H.G.
67. Johnston, H., *Force-microscopy firm finds success in 3D*. 2008.
68. Kiessig, H., *Interferenz von Röntgenstrahlen an dünnen Schichten.* Annalen der Physik, 1931. **402**(7): p. 769-788.
69. Dosch, H., *Evanescent absorption in kinematic surface Bragg diffraction.* Physical Review B, 1987. **35**(5): p. 2137.
70. Inaba, K., et al., *High resolution X-ray diffraction analyses of (La, Sr) MnO*

3/ZnO/Sapphire (0001) double heteroepitaxial films. 2013.

71. Luo, Z., et al., *Probing the domain structure of BiFeO3 epitaxial films with three-dimensional reciprocal space mapping*. Applied Physics Letters, 2014. **104**(18): p. 182901.

Chapter 2 Three-domain model, its functional predictions and previous experiments, e_{31} test;

In this chapter the phenomenological three-domain model, the resulting phase diagram and predictions of the strain dependent piezoelectric properties of $Pb(Zr,Ti)O_3$ (PZT) solid solution are reviewed. An experimental strategy of validating the phenomenological predictions is proposed.

Thin film samples of PZT are prepared by Pulsed Laser Deposition (PLD) to study the transversal piezoelectric coefficient e_{31} using a 4-point bending setup. Additional simulations by a Finite Element Analysis (FEA) commercial software Solidworks showed that the strain applied by bending cannot exceed 0.005 (tensile), which is below the values of interests. The strategy had therefore to be reconsidered.

The layout of this chapter is listed as followed:

- The motivation and progress of three-domain model;
- Thermal strain phase diagrams and property predictions of PZT thin films based on three-domain model;
- The first strategy is stated to validate three-domain model by measuring e_{31};
- e_{31} measurements and calculated results.

2.1. General introduction to three-domain model

As mentioned in chapter 1, Landau's phenomenological approach has been very successful in the description of phase transitions in superconductors, ferromagnetic materials and ferroelectrics. In case of ferroelectrics, using high quality single crystal materials, the experimental results successfully proved the phenomenological results.[1, 2]

However, there are still several concerns that make piezoelectric properties of thin films different from single crystals. In thin films, a few percent of bi-axial strain can be endured where the bulk would crack. Some early work regarding coherently

strained ferroelectric thin films, showed strain dependent transition temperature, symmetry and dielectric response.[3-9] Therefore, in the three-domain model, the relationship of symmetry and ferroelectricity to strain was discussed and studied.[10] Moreover, in particular case studies, PZT thin film phase transition and piezoelectric properties were computed by the three-domain model with mechanical thermal strain as boundary conditions.[11]

Clamped poly-domain single crystalline ferroelectric thin films experience the strain that is induced by the substrate, caused by epitaxial growth and thermal misfit. Additionally, the electrodes also affect the strain state of the piezo-materials. For example, thick film bottom electrodes (20-40 nm) can start to relax and only partially deliever the epitaxial strain onto the ferroelectric thin film material. Finally, domain wall movements, pinning effects and substrate crystal orientation should be considered.[12, 13] For instance, literature shows the largest value for e_{31} from a (110) oriented Morphotropic Phase Boundary (MPB) PZT film on Si with composition $x \approx 0.6$ instead of $x = 0.48$.[14] These discoveries indicate a further comprehensive understanding is required applying Landau-Ginzburg-Devonshire (LGD) theory to films.

Tetragonal ferroelectric domains can be classified based on the orientations of dipolar domains, a-domains (dipolar in [001] in-plane), b-domains (dipolar in [010] in-plane) and c-domains (dipolar in out-plane or [001]). For instance, $PbTiO_3$ films on $SrTiO_3$ showed a/b/c ferroelectric domains and these domains were experimentally observed in Reciprocal Space Maps (RSMs) plotted in 3D.[15] Koukhar, Pertsev et al. established a series of theorical papers on tetragonal poly-domain thin films in which the a-domains were assumed to be the same as b-domains.[16, 17] This approximation (2-Dimension model) simplified the calculations, but it is not applicable to systems with lower symmetry. For instance, relaxed $PbTiO_3$ film show a clear number of differences between a-domains and b-domains. Moreover, rhombohedral phases and monoclinic phases, such as $BiFeO_3$ at MPB, for example, cannot be sufficiently modelled in two dimensions.[18, 19] All these suggest a model, able to describe ferroelectric domains in all 3 lattice orientations.

Houwman et al. developed a what was called a ‘three-domain model’ based on Koukhar and Pertsev’s 2-Dimensional model. The present experimental study serves as support of the model. The three-domain model connects domain wall motion, external elastic and electric field to intrinsic ferroelectric and piezoelectric properties of a clamped films.[10] Using this model, the authors predicted the piezoelectric behaviour and crystal symmetry transition as function of the substrate misfit strain due to thermal expansion mismatch for different compositions.[11]

2.2. Functional properties predictions by three-domain model

For clamped $PbZr_xTi_{1-x}O_3$(PZT) films near MPB composition (x=0.4, 0.5, 0.6), Vergeer predicted functional properties, such as piezoelectric coefficient and dielectric coefficient, based on the three-domain model, where tetragonal domains have three differently oriented dipoles. In his thesis, model simulations were performed using temperature, misfit strain and external electrical field as control parameters.

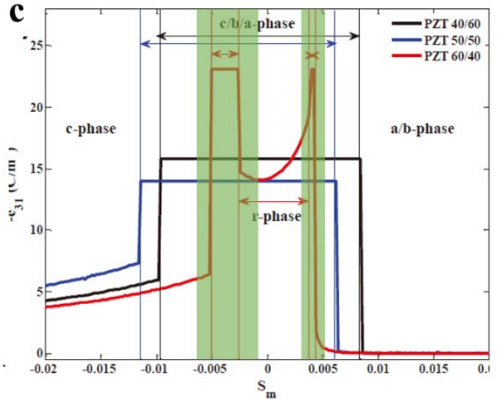

Figure 2.1. *The calculated e_{31} of PZT(Zr/Ti = 6/4) against thermal misfit strain Sm.*

The results of the simulations for PZT(Zr/Ti = 6/4) indicated that the co-existing a/b/c-phases, with the different dipole orientations, were stable at a tensile strain of 0.004 and at a compressive strain of approximately 0.0025 to 0.005. A stable rhombohedral phase was predicted at a misfit strain, between tensile 0.004 and compressive 0.0025. Furthermore, a tetragonal phase with in-plane orientated a/b-

domains was predicted for PZT for a tensile strain larger than 0.004. A c-domain tetragonal phase is predicted at a compressive strain lager than 0.004. The rich phase transitions as a function of strain benefit the polarisation rotation and domain wall movements in the film, which lead to a significant enhancement in piezoelectric and dielectric properties.

Furthermore, the domain fraction in the a/b/c-phase in PZT (x=0.6) is found to heavily depend on the external electric field. The amount of c-domain is increasing with increasing voltage, while the amounts of in-plane domains are decreasing.

In this project, the PZT composition x=0.6 is selected for our experimental study. For the PZT (x=0.6) simulations show the highest enhancement in piezoelectric coefficient (to 170 pm/V). Furthermore, this regime was predicted to show, the richest phase diagram (c-phase, a/b/c-phase, R phase and a/b-phase), which gives ample possibilities to tune and study the functional properties.

2.3. First strategy of demonstration

To verify the predictions of the functional properties in PZT (x=0.6) thin films, a first approach was chosen. By measuring the transversal piezoelectric charge coefficient e_{31} of a PLD deposited 400nm thickness PZT thin film on a silicon (001) single crystal substrate, it is possible to validate the predictions with quantitative experiments.

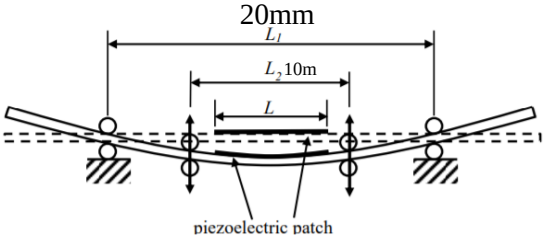

Figure 2.2. *The schematic of 4-point bending test. On the right picture shows the yielded Si beams.*

A four-point bending aixACCT setup (a commercial system for piezoelectric

property measurement) was used to apply strain and test the accumulated charges at the surface. In this measurement, two inner metallic rods apply the force perpendicular to the sample surface and simultaneously connect to the sample electrodes. The two outside rods beneath the sample are fixed and act as support. During the measurement, the inside rods are pushed downward, to form a bending curvature in the PZT. The displacement of the two inside rods is measured by a micro-meter, which can be used to estimate the deformation strain in the sample.

To estimate the strain value, both a theorical strain analysis as well as simulations were performed. The silicon wafer thickness is 0.5 mm, covered with a $CaNbO_3$ (CNO) nanosheet layer (used to achieve epitaxial growth on Si), on which layers of 40 nm $SrRuO_3$ (SRO) and 400 nm PZT were deposited. Due to the thickness of the whole sample, the classical mechanical Timoshenko beam theory can be used to analyse and to estimate the strain at the samples surfaces. Furthermore, the deformation strain was also simulated by the FEA software package to create a realistic boundary conditions.

With the increasing displacement of the rods, the sample surface strain will expand or compress the PZT film, which aligns the dipoles and attracts charges. The ability to continuously change the magnitude of the strain in the PZT film, allows us to measure the e_{31} and verify the PZT functional properties predicted by three-domain model.

2.4. Sample preparation

The bottom electrode SRO and the functional layer PZT (x=0.6) was deposited on CNO nanosheets that were transferred on a Si wafer. The substrate was glued on a resistive heater with silver paste and was dried by a plate heater to 100℃ for 2-5 mins in order to remove the organic residuals of the silver paste. Subsequently, the sample was placed into the PLD chamber, the targets were pre-ablated at 0.1mbar oxygen pressure for 5mins with 10Hz pulsed laser. Then the shutter was moved and the chamber was vacuumized until the background pressure was less than 10^{-5} mbar, after which the sample was heated up to 650℃ for 30mins to remove possible residuals on the nano-sheet surface.

The SRO layer was deposited at 600℃, 0.13 mbar oxygen pressure 2.5 J/cm^2 fluence and 4 Hz repetition rate for the laser during 12 mins. The PZT layer was deposited at 615℃, 0.1 mbar oxygen pressure 0.1 mbar and the repetition rate of the laser was set at 5 Hz for 40 mins. These parameters were optimised to achieve a good crystallinity in the films and a less than 1nm surface roughness. After deposition, the sample was kept in a static pressure of 100 mbar pure oxygen for 30 mins in order to anneal the sample after which the sample was cooled down to room temperature in the same pressure using a cooling rate of 10 ℃/min.

The sample went through a lithographic process to pattern the sputtered metal Pt top electrodes. Finally, the wafer was diced into small rectangular shapes and cleaned for bending test.

2.5. e_{31} four-point bending test

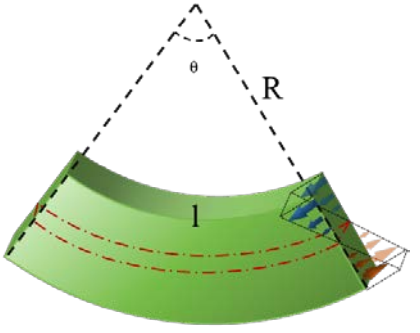

Figure 2.3. *The schematic of a classical mechanical beam model with neutral plane.*

The strain in PZT film introduced by bending can be calculated using the beam model in Timoshenko theory by assuming a strain neutral plane with a radius R, dependent on the bending curvature. This neutral plane length is l, and the equation for the strain is given as follow:

$$\varepsilon = \frac{\delta l}{l} \tag{2.1}$$

The measured displacement of inside rods is approximate 0.06 mm before the Si

wafer yield, it gives a max bending curvature angle for 0.688°, and leads to a maximum yield strain of approximatly 0.001, which is less than the predicted strain 0.004 to show an enhancement in piezoelectric e_{31}.

There are some concerns of this estimation. In this Timoshenko beam model, the PZT film thickness is small compared to the total thickness. This dimensional difference may create errors in the calculation. The lattices in the Si single crystal substrate and the PZT film both suffer from the three-dimensional deformation during the bending, Poisson's ratio should play a role here. The Si single crystal average elastic modulus is 130-170 GPa but the bending strength is only 3-10 GPa suggests a strong dimensional effect in Si wafer.[20, 21] Meanwhile, the Timoshenko theory is suitable for beams with relatively small length over thickness ratio, about 5-10. In contrast, transverse shear deformation is neglected in Euler-Bernoulli beam theory making this theory is more suitable for Si single crystal substrate. Furthermore, the inside rods displacement that press sample was measured by a micrometre and showed a large error tolerance in contrast of the sample thickness. In short summary, the bending test strategy could not fulfil the desire of prove the phase diagram, but it is still worthy of using a second method to confirm this.

To better estimate the strain that can be applied in the PZT film, finite element

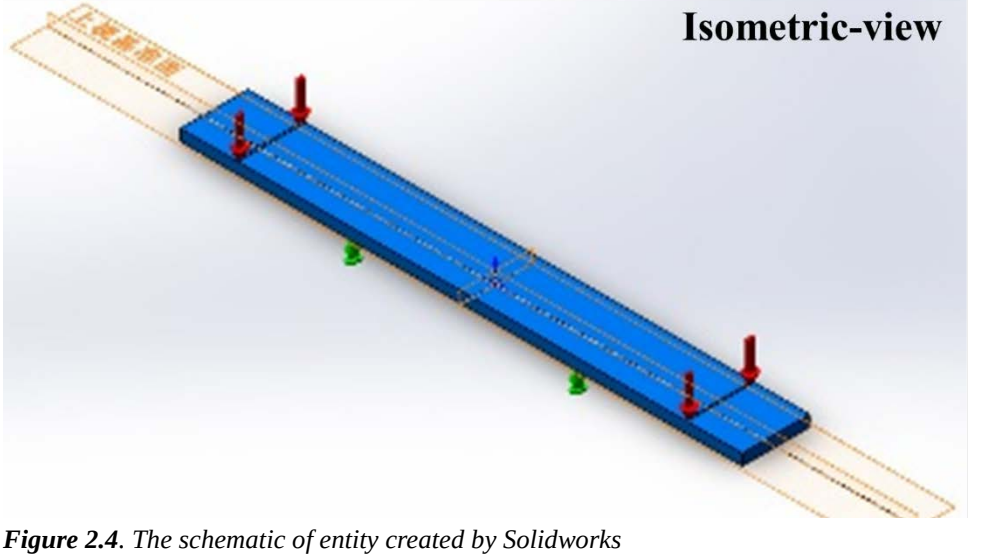

***Figure 2.4**. The schematic of entity created by Solidworks*

analysis is used for simulating the longitudinal axis strain by Solidworks cosmos plug-in. The sample was created in software with a 25mm total length, 5mm width and 0.5 mm thickness.

The red arrows indicate the locations of pressure on the entity as boundary conditions, while the green nods beneath the entity supports the whole beam. The areas were set to 5 mm x 0.1 mm to simulate the contact area of the rods with the sample. Si single crystal from Solidworks materials database was selected for the material property (Density 2330 kg/cm^3, Poisson's ratio 0.28, elastic module 1.124 x 1011 N/m^2 and yield strength 1.2x108 N/m^2 at room temperature). To a high-quality analysis, 20000 nods was set to give 11021 square shape mesh units, and each mesh unit is 0.28 mm as an average size.

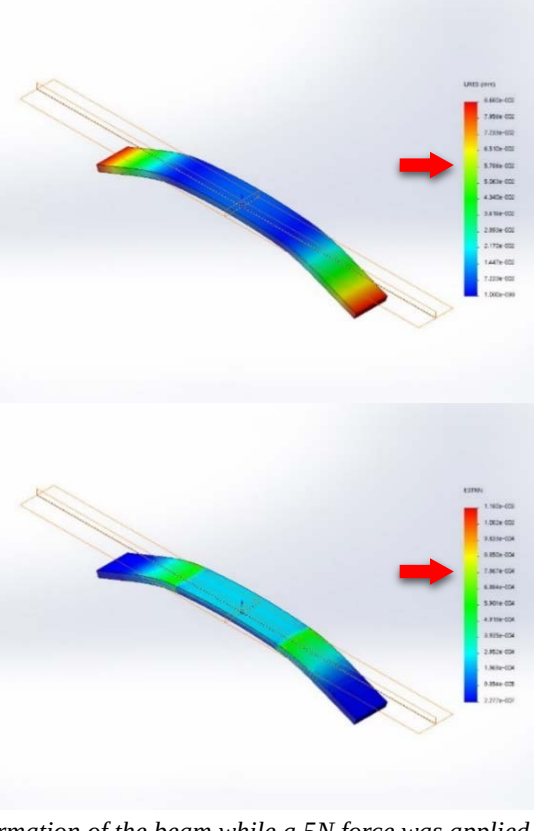

Figure 2.5. *The deformation of the beam while a 5N force was applied.*

5N is applied to the pressing region perpendicular to the sample top surface, see Fig.2.5 the deformations are exaggerated to show the displacements. The yield points are labelled in each figure. The simulation shows the Si substrate yields and breaks when the displacement reaches the limits, which are approximate 0.058 mm and the longitudinal strain is 0.0079. These results are in good agreement with practical measurements: the maximum displacement that can be applied by the rods is approximate 0.06mm. The simulation shows the maximal strain that can be applied is lower than the desired strain.

2.6. Conclusion

In summary, three-domain model has been developed for tetragonal a/b/c-phase in PZT, and PZT functional properties have been simulated for varies compositions and temperatures. The PZT composition with x=0.6 shows the most interesting piezoelectric properties, and was selected to experimentally validate the model.

400 nm thick PZT films on 40 nm SRO bottom electrodes on a nanosheet covered Si wafer samples were made to study e_{31} by a four-point bending tester. The e_{31} phase diagram required a tensile strain at 0.04 to show an enhancement in dielectric coefficient. It has been proven by the Timoshenko beam theory and finite element analysis that 0.04 tensile strain cannot be reached by such bending test. The Si substrate yields and breaks at strain approximate 0.0079 by simulation. Therefore, a new strategy was required to validate the model. In the next chapters this strategy will be shown.

Reference:

1. Zhang, Y., et al., Presence of a purely tetragonal phase in ultrathin BiFeO3 films: Thermodynamics and phase-field simulations. Acta Materialia, 2020. **183**: p. 110-117.
2. Huang, C. and L. Chen, *Landau Theory of Multiferroics.* Multiferroic Materials: Properties, Techniques, and Applications, 2016: p. 257.
3. Choi, K.J., et al., *Enhancement of ferroelectricity in strained BaTiO3 thin films.* Science, 2004. **306**(5698): p. 1005-1009.
4. Li, Y. and L. Chen, *Temperature-strain phase diagram for Ba Ti O 3 thin films.* Applied physics letters, 2006. **88**(7): p. 072905.
5. Li, Y., et al., Phase transitions and domain structures in strained pseudocubic (100) Sr Ti O 3 thin films. Physical Review B, 2006. **73**(18): p. 184112.
6. Yanase, N., et al., Thickness dependence of ferroelectricity in heteroepitaxial BaTiO3 thin film capacitors. Japanese journal of applied physics, 1999. **38**(9S): p. 5305.
7. Rijnders, G. and D.H. Blank, *Build your own superlattice.* Nature, 2005. **433**(7024): p. 369-370.
8. Nguyen, M.D., et al., Misfit strain dependence of ferroelectric and piezoelectric properties of clamped (001) epitaxial Pb (Zr0. 52, Ti0. 48) O3 thin films. Applied physics letters, 2011. **99**(25): p. 252904.
9. Koster, G., M. Huijben, and G. Rijnders, *Epitaxial growth of complex metal oxides*. 2015: Elsevier.
10. Houwman, E., et al., Modelling functional properties of ferroelectric oxide thin films with a three-domain structure. arXiv preprint arXiv:1901.10883, 2019.
11. Vergeer, K., Structure and functional properties of epitaxial PBZRxTI1-xO3 films. 2017.
12. Tagantsev, A.K., et al., Nature of nonlinear imprint in ferroelectric films and long-term prediction of polarization loss in ferroelectric memories. Journal of applied physics, 2004. **96**(11): p. 6616-6623.
13. Tagantsev, A.K., L.E. Cross, and J. Fousek, *Domains in ferroic crystals and thin films*. Vol. 13. 2010: Springer.
14. Wan, X., et al., Enhanced piezoelectric properties of (110)-oriented PbZr1−

xTixO3 epitaxial thin films on silicon substrates at shifted morphotropic phase boundary. Applied physics letters, 2014. **104**(9): p. 092902.

15. Xu, H., et al., Mixture domain states in PbTiO3 film with potentials for functional application. Applied Physics Letters, 2019. **114**(24): p. 242901.
16. Koukhar, V., N. Pertsev, and R. Waser, Thermodynamic theory of epitaxial ferroelectric thin films with dense domain structures. Physical Review B, 2001. **64**(21): p. 214103.
17. Kukhar, V., et al., Polarization states of polydomain epitaxial Pb (Zr 1− x Ti x) O 3 thin films and their dielectric properties. Physical Review B, 2006. **73**(21): p. 214103.
18. Xu, H., et al., Shear strain-induced anisotropic domain evolution in mixed-phase BiFeO3 epitaxial films. AIP Advances, 2019. **9**(2): p. 025114.
19. Luo, Z., et al., Probing the domain structure of BiFeO3 epitaxial films with three-dimensional reciprocal space mapping. Applied Physics Letters, 2014. **104**(18): p. 182901.
20. Guangping, H., L. Kai, and W. Xiuhong, *Bending test of single crystal silicon micro-bridge beams for mechanical properties.* Chinese Journal of Scientific Instrument, 2006. **27**(2): p. 176.
21. Zhu, X., et al., *An empirical equation for prediction of silicon wafer deformation.* Materials Research Express, 2017. **4**(6): p. 065904.

Chapter 3 Mathematical construction of reciprocal space maps of poly-domain PZT films

In chapter 3, reciprocal spacing mapping (RSM) was used to confirm the crystal symmetry and lattice constants of PZT films, which are key to explain ferroelectric polarisation behaviour and the piezoelectric properties. These results are also critical to validate the three-domain model and the applicability of the phenomenological phase diagrams. Therefore, it is important to correctly interpret the RSMs results. In this chapter, we present mathematical descriptions for the observed tetragonal symmetry, rhombohedral symmetry, and monoclinic symmetry. The calculated results, such as for rhombohedral (101) reflection, are validated by RSMs measurements in this thesis. The approach can be also quickly adopted into other crystal symmetries to produce expected reciprocal space patterns.

3.1. Tetragonal symmetry

The tetragonal phase by definition is where $a = b \neq c$, $\alpha = \beta = \gamma = 90°$. For PZT, in the tetragonal phase, the polarisation orientation for ferroelectric materials is along the elongated lattice direction. For micro-sized mono-domain ferroelectric thin films, the out-of-plane c-domain (lattice elongates in c-axis) is preferable. However, in-plane domains (lattice elongates in a/b-axis) may also be present, which are denoted as a-domain and b-domain as showing in Figure 3.1.

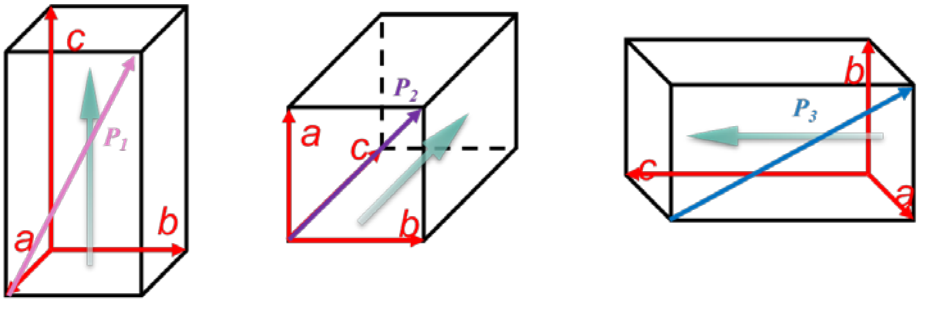

Figure 3.1 . *The out-of-plane tetragonal c-domain, in-plane a-domain and in-plane b-domain from left to right, respectively. The green arrow stands for the polarisation orientation. The red arrows are tetragonal lattice co-ordination axis and P_1, P_2 and P_3*

present the reciprocal vector [101] possibilities of tetragonal can exist in the thin films.

The green arrows represent the polarisation direction, the pink arrow, purple arrow and blue arrow presents the (101) reflection vectors for each domain.

First step is to establish the co-ordinates of tetragonal lattice in real space:

$$\vec{a} = a\begin{pmatrix}1\\0\\0\end{pmatrix} \qquad \vec{b} = b\begin{pmatrix}0\\1\\0\end{pmatrix} \qquad \vec{c} = c\begin{pmatrix}0\\0\\1\end{pmatrix}$$

$$\vec{C} = \frac{\vec{a} \times \vec{b}}{V} = \frac{1}{c}\begin{pmatrix}0\\0\\1\end{pmatrix} \qquad \vec{B} = \frac{1}{b}\begin{pmatrix}0\\1\\0\end{pmatrix} \qquad \vec{A} = \frac{1}{a}\begin{pmatrix}1\\0\\0\end{pmatrix}$$

Then convert these co-ordinates into reciprocal space vectors for tetragonal c-domain (P_1):
Hence:

$$\vec{G}(101) = \vec{A} + \vec{C} = (101) = \begin{pmatrix}1/a\\0\\1/c\end{pmatrix}$$

$$\vec{G}(111) = \vec{A} + \vec{B} + \vec{C} = (111) = \begin{pmatrix}1/a\\1/b\\1/c\end{pmatrix}$$

For tetragonal a-domain (P_2):

$$\vec{C} = \frac{\vec{a} \times \vec{b}}{V} = \frac{1}{a}\begin{pmatrix}0\\0\\1\end{pmatrix} \qquad \vec{B} = \frac{1}{c}\begin{pmatrix}0\\1\\0\end{pmatrix} \qquad \vec{A} = \frac{1}{b}\begin{pmatrix}1\\0\\0\end{pmatrix}$$

Gives:

$$\vec{G}(101) = \vec{A} + \vec{C} = (101) = \begin{pmatrix} 1/c \\ 0 \\ 1/b \end{pmatrix}$$

$$\vec{G}(111) = \vec{A} + \vec{B} + \vec{C} = (111) = \begin{pmatrix} 1/c \\ 1/a \\ 1/b \end{pmatrix}$$

For tetragonal b-domain (P_3):

$$\vec{C} = \frac{\vec{a} \times \vec{b}}{V} = \frac{1}{b}\begin{pmatrix} 0 \\ 0 \\ 1 \end{pmatrix} \qquad \vec{B} = \frac{1}{a}\begin{pmatrix} 0 \\ 1 \\ 0 \end{pmatrix} \qquad \vec{A} = \frac{1}{c}\begin{pmatrix} 1 \\ 0 \\ 0 \end{pmatrix}$$

Therefore:

$$\vec{G}(101) = \vec{A} + \vec{C} = (101) = \begin{pmatrix} 1/b \\ 0 \\ 1/a \end{pmatrix}$$

$$\vec{G}(111) = \vec{A} + \vec{B} + \vec{C} = (111) = \begin{pmatrix} 1/a \\ 1/b \\ 1/c \end{pmatrix}$$

Now asymmetrical RSM (101) and (111) can be constructed as follows:

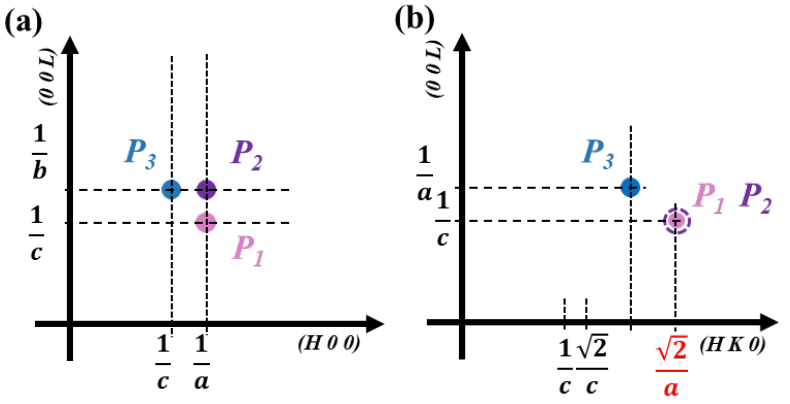

Figure 3.2. *The calculated RSMs of tetragonal poly-domain pattern in reciprocal plane (101) and (111).*

3.2. Rhombohedral symmetry

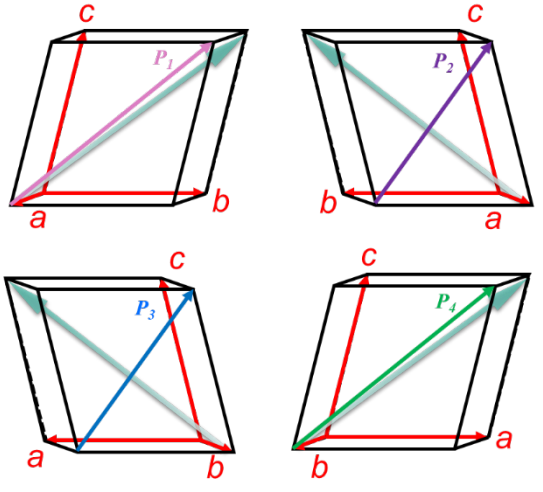

Figure 3.3. *The four possibilities of vector (101) in real rhombohedral thin films, respectively. The green arrow stands for the polarisation orientation. The red arrows are rhombohedral lattice co-ordination axis. The notions* P_1, P_2, P_3 *and* P_4 *present the reciprocal vector [101] possibilities.*

Rhombohedral symmetry can be considered as a cube that elongated in [111] direction. This deformation from cubic leaves rhombohedral symmetry to a = b = c,

$\alpha = \beta = \gamma \neq 90°$. In poly-domain rhombohedral ferroelectric materials, four possible [101] vectors are described in Figure 3.3. Rhombohedral lattice co-ordinates are not aligned with cubic co-ordinates; therefore, the construction of rhombohedral lattice co-ordinates require a new description:
Where x and y are integers from cubic co-ordinates, $x \neq y$.[1]

$$\vec{a} = \begin{pmatrix} x \\ y \\ y \end{pmatrix} \qquad \vec{b} = \begin{pmatrix} y \\ x \\ y \end{pmatrix} \qquad \vec{c} = \begin{pmatrix} y \\ y \\ x \end{pmatrix}$$

Then for P_1,

$$\vec{C} = \frac{\vec{a} \times \vec{b}}{V} = \begin{pmatrix} x \\ y \\ y \end{pmatrix} \begin{pmatrix} y \\ x \\ y \end{pmatrix} / V = 2\pi \begin{pmatrix} y^2 - xy \\ y^2 - xy \\ x^2 - y^2 \end{pmatrix} \Big/ (x^3 - 3xy^2 + 2y^3)$$

$$\vec{B} = \frac{\vec{a} \times \vec{c}}{V} = \begin{pmatrix} y \\ y \\ x \end{pmatrix} \begin{pmatrix} x \\ y \\ y \end{pmatrix} / V = 2\pi \begin{pmatrix} y^2 - xy \\ x^2 - y^2 \\ y^2 - xy \end{pmatrix} \Big/ (x^3 - 3xy^2 + 2y^3)$$

$$\vec{A} = \frac{\vec{b} \times \vec{c}}{V} = \begin{pmatrix} y \\ x \\ y \end{pmatrix} \begin{pmatrix} y \\ y \\ x \end{pmatrix} / V = 2\pi \begin{pmatrix} x^2 - y^2 \\ y^2 - xy \\ y^2 - xy \end{pmatrix} \Big/ (x^3 - 3xy^2 + 2y^3)$$

Hence, the asymmetrical (101) and (111) can be constructed as followed:

$$\vec{G}(101) = \vec{A} + \vec{C} = (101) = 2\pi \begin{pmatrix} x^2 - xy \\ 2y^2 - 2xy \\ x^2 - xy \end{pmatrix} \Big/ (x^3 - 3xy^2 + 2y^3)$$

$$\vec{G}(111) = \vec{A} + \vec{B} + \vec{C} = (111) = \begin{pmatrix} (x-y)^2 \\ (x-y)^2 \\ (x-y)^2 \end{pmatrix}$$

For P_2:

$$\vec{a} = \begin{pmatrix} -x \\ y \\ y \end{pmatrix} \qquad \vec{b} = \begin{pmatrix} -y \\ x \\ y \end{pmatrix} \qquad \vec{c} = \begin{pmatrix} -y \\ y \\ x \end{pmatrix}$$

Then results in the reciprocal space lattice vectors:

$$\vec{C} = \frac{\vec{a} \times \vec{b}}{V} = \begin{pmatrix} -x \\ y \\ y \end{pmatrix} \begin{pmatrix} -y \\ x \\ y \end{pmatrix} / V = 2\pi \begin{pmatrix} xy - y^2 \\ y^2 - xy \\ x^2 - y^2 \end{pmatrix} \Big/ (x^3 - 3xy^2 + 2y^3)$$

$$\vec{B} = \frac{\vec{a} \times \vec{c}}{V} = \begin{pmatrix} -y \\ y \\ x \end{pmatrix} \begin{pmatrix} -x \\ y \\ y \end{pmatrix} / V = 2\pi \begin{pmatrix} xy - y^2 \\ x^2 - y^2 \\ y^2 - xy \end{pmatrix} \Big/ (x^3 - 3xy^2 + 2y^3)$$

$$\vec{A} = \frac{\vec{b} \times \vec{c}}{V} = \begin{pmatrix} -y \\ x \\ y \end{pmatrix} \begin{pmatrix} -y \\ y \\ x \end{pmatrix} / V = 2\pi \begin{pmatrix} -x^2 + y^2 \\ y^2 - xy \\ y^2 - xy \end{pmatrix} \Big/ (x^3 - 3xy^2 + 2y^3)$$

Thus,

$$\vec{G}(101) = \vec{A} + \vec{C} = 2\pi \begin{pmatrix} xy - x^2 \\ 2y^2 - 2xy \\ x^2 - xy \end{pmatrix} \Big/ (x^3 - 3xy^2 + 2y^3)$$

$$\vec{G}(111) = \vec{A} + \vec{B} + \vec{C} = (111) = \begin{pmatrix} -(x-y)^2 \\ (x-y)^2 \\ (x-y)^2 \end{pmatrix}$$

For P_3:

$$\vec{a} = \begin{pmatrix} x \\ -y \\ y \end{pmatrix} \qquad \vec{b} = \begin{pmatrix} y \\ -x \\ y \end{pmatrix} \qquad \vec{c} = \begin{pmatrix} y \\ -y \\ x \end{pmatrix}$$

Gives:

$$\vec{C} = \frac{\vec{a} \times \vec{b}}{V} = \begin{pmatrix} -x \\ y \\ y \end{pmatrix} \begin{pmatrix} -y \\ x \\ y \end{pmatrix} / V = 2\pi \begin{pmatrix} -xy + y^2 \\ -y^2 + xy \\ x^2 - y^2 \end{pmatrix} \Big/ (x^3 - 3xy^2 + 2y^3)$$

$$\vec{B} = \frac{\vec{a} \times \vec{c}}{V} = \begin{pmatrix} -y \\ y \\ x \end{pmatrix} \begin{pmatrix} -x \\ y \\ y \end{pmatrix} / V = 2\pi \begin{pmatrix} -xy + y^2 \\ -x^2 + y^2 \\ y^2 - xy \end{pmatrix} \Big/ (x^3 - 3xy^2 + 2y^3)$$

$$\vec{A} = \frac{\vec{b} \times \vec{c}}{V} = \begin{pmatrix} -y \\ x \\ y \end{pmatrix} \begin{pmatrix} -y \\ y \\ x \end{pmatrix} / V = 2\pi \begin{pmatrix} x^2 - y^2 \\ -y^2 + xy \\ y^2 - xy \end{pmatrix} \Big/ (x^3 - 3xy^2 + 2y^3)$$

And lead to:

$$\vec{G}(101) = \vec{A} + \vec{C} = 2\pi \begin{pmatrix} -xy + x^2 \\ -2y^2 + 2xy \\ x^2 - xy \end{pmatrix} \Big/ (x^3 - 3xy^2 + 2y^3)$$

$$\vec{G}(111) = \vec{A} + \vec{B} + \vec{C} = (111) = \begin{pmatrix} (x-y)^2 \\ -(x-y)^2 \\ (x-y)^2 \end{pmatrix}$$

Finally, for P_4:

$$\vec{a} = \begin{pmatrix} -x \\ -y \\ y \end{pmatrix} \qquad \vec{b} = \begin{pmatrix} -y \\ -x \\ y \end{pmatrix} \qquad \vec{c} = \begin{pmatrix} -y \\ -y \\ x \end{pmatrix}$$

Thus, the reciprocal space vectors are:

$$\vec{C} = \frac{\vec{a} \times \vec{b}}{V} = \begin{pmatrix} -x \\ -y \\ y \end{pmatrix} \begin{pmatrix} -y \\ -x \\ y \end{pmatrix} / V = 2\pi \begin{pmatrix} xy - y^2 \\ -y^2 + xy \\ x^2 - y^2 \end{pmatrix} \Big/ (x^3 - 3xy^2 + 2y^3)$$

$$\vec{B} = \frac{\vec{a} \times \vec{c}}{V} = \begin{pmatrix} -y \\ -y \\ x \end{pmatrix} \begin{pmatrix} -x \\ -y \\ y \end{pmatrix} / V = 2\pi \begin{pmatrix} xy - y^2 \\ -x^2 + y^2 \\ y^2 - xy \end{pmatrix} \Big/ (x^3 - 3xy^2 + 2y^3)$$

$$\vec{A} = \frac{\vec{b} \times \vec{c}}{V} = \begin{pmatrix} -y \\ -x \\ y \end{pmatrix} \begin{pmatrix} -y \\ -y \\ x \end{pmatrix} / V = 2\pi \begin{pmatrix} -x^2 + y^2 \\ -y^2 + xy \\ y^2 - xy \end{pmatrix} \Big/ (x^3 - 3xy^2 + 2y^3)$$

and therefore:

$$\vec{G}(101) = \vec{A} + \vec{C} = 2\pi \begin{pmatrix} xy - x^2 \\ -2y^2 + 2xy \\ x^2 - xy \end{pmatrix} \Big/ (x^3 - 3xy^2 + 2y^3)$$

$$\vec{G}(111) = \vec{A} + \vec{B} + \vec{C} = (111) = \begin{pmatrix} -(x-y)^2 \\ -(x-y)^2 \\ (x-y)^2 \end{pmatrix}$$

Hence asymmetrical RSM (101) and (111) can be constructed as followed:

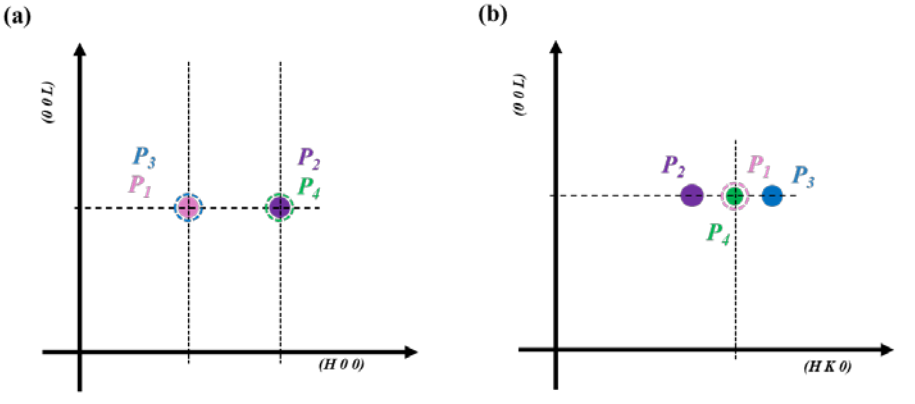

Figure 3.4. *The calculated RSMs of rhombohedral poly-domain pattern in reciprocal plane (101) and (111)*

3.3. Monoclinic symmetry (C-type)

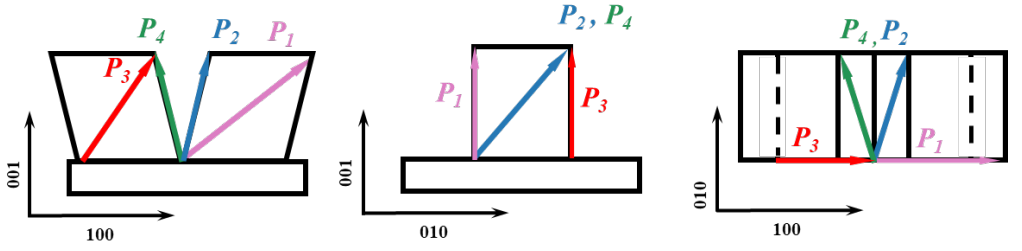

Figure 3.5. *The four possibilities of vector (101) in real monoclinic c-type thin films, respectively. The notions P_1, P_2, P_3 and P_4 present the reciprocal vector [101] possibilities.*

Monoclinic c-type symmetry is the group of lattices that elongates direction in (010) plane. $\vec{c}_m$-vector is tilted over angle δ from the z-axis in the ZX-plane, thus x-coordinate of this vector is $c_m sin\delta \approx c_m\delta$ and z-coordinate is $c_m cos\delta \approx c_m$ in lowest order in δ. The monoclinic unit cell vectors and volume are in the cubic lattice system given by (approximately).

We write the base vectors that form a right-handed frame, rotating a to b defines c-direction

$$\vec{a} = a_m\begin{pmatrix}1\\0\\0\end{pmatrix},\quad \vec{b} = b_m\begin{pmatrix}0\\1\\0\end{pmatrix},\quad \vec{c} = c_m\begin{pmatrix}\delta\\0\\1\end{pmatrix}\qquad V_m \approx a_m b_m c_m \text{ if all angles are small}$$

Reciprocal lattice vectors $\vec{A}$ etc from the cross-products with lowest order in δ

$$\vec{a}\times\vec{b} = a_m b_m\begin{pmatrix}1\\0\\0\end{pmatrix}\times\begin{pmatrix}0\\1\\0\end{pmatrix} \approx a_m b_m\begin{pmatrix}0\\0\\1\end{pmatrix} \qquad \vec{C} = \frac{\vec{a}\times\vec{b}}{V} = \frac{1}{c_m}\begin{pmatrix}0\\0\\1\end{pmatrix}$$

$$\vec{c}\times\vec{a} = c_m a_m\begin{pmatrix}\delta\\0\\1\end{pmatrix}\times\begin{pmatrix}1\\0\\0\end{pmatrix} \approx c_m a_m\begin{pmatrix}0\\1\\0\end{pmatrix} \qquad \vec{B} = \frac{1}{b_m}\begin{pmatrix}0\\1\\0\end{pmatrix}$$

$$\vec{b}\times\vec{c} = b_m c_m\begin{pmatrix}0\\1\\0\end{pmatrix}\times\begin{pmatrix}\delta\\0\\1\end{pmatrix} \approx b_m c_m\begin{pmatrix}1\\0\\-\delta\end{pmatrix} \qquad \vec{A} = \frac{1}{a_m}\begin{pmatrix}1\\0\\-\delta\end{pmatrix}$$

The reciprocal lattice vector $\vec{G}(hkl) = \begin{pmatrix} h/a_0 \\ k/a_0 \\ l/a_0 \end{pmatrix}$, with a_0 the length of the cubic lattice vector (e.g., with length 1 Å).

For example

$$\vec{G}(101) = \vec{A} + \vec{C} = (101)_{mC} = \begin{pmatrix} 1/a_m \\ 0 \\ -\delta/a_m + 1/c_m \end{pmatrix} \approx \begin{pmatrix} 1/a_{pc} \\ 0 \\ 1/a_{pc} \end{pmatrix}$$

$$\vec{G}(111) = \vec{A} + \vec{B} + \vec{C} = (111)_{mC} = \begin{pmatrix} 1/a_m \\ 1/b_m \\ -\delta/a_m + 1/c_m \end{pmatrix} \approx \begin{pmatrix} 1/a_{pc} \\ 1/a_{pc} \\ 1/a_{pc} \end{pmatrix}$$

The vector P_2 with approximately the same direction has different unit cell vectors, due to rotation of the unit cell in the XYZ-frame:

$$\vec{a} = b_m \begin{pmatrix} 1 \\ 0 \\ 0 \end{pmatrix}, \quad \vec{b} = a_m \begin{pmatrix} 0 \\ 1 \\ 0 \end{pmatrix}, \vec{c} = c_m \begin{pmatrix} 0 \\ \delta \\ 1 \end{pmatrix} \quad V_m \approx a_m b_m c_m$$

$$\vec{a} \times \vec{b} = a_m b_m \begin{pmatrix} 1 \\ 0 \\ 0 \end{pmatrix} \times \begin{pmatrix} 0 \\ 1 \\ 0 \end{pmatrix} \approx a_m b_m \begin{pmatrix} 0 \\ 0 \\ 1 \end{pmatrix} \qquad \vec{C} = \frac{\vec{a} \times \vec{b}}{V} = \frac{1}{c_m} \begin{pmatrix} 0 \\ 0 \\ 1 \end{pmatrix}$$

$$\vec{c} \times \vec{a} = c_m b_m \begin{pmatrix} 0 \\ \delta \\ 1 \end{pmatrix} \times \begin{pmatrix} 1 \\ 0 \\ 0 \end{pmatrix} \approx c_m b_m \begin{pmatrix} 0 \\ 1 \\ -\delta \end{pmatrix} \qquad \vec{B} = \frac{1}{a_m} \begin{pmatrix} 0 \\ 1 \\ -\delta \end{pmatrix}$$

$$\vec{b} \times \vec{c} = a_m c_m \begin{pmatrix} 0 \\ 1 \\ 0 \end{pmatrix} \times \begin{pmatrix} 0 \\ \delta \\ 1 \end{pmatrix} \approx a_m c_m \begin{pmatrix} 1 \\ 0 \\ 0 \end{pmatrix} \qquad \vec{A} = \frac{1}{b_m} \begin{pmatrix} 1 \\ 0 \\ 0 \end{pmatrix}$$

$$\vec{G}(101) = \vec{A} + \vec{C} = (101)_{mC} = \begin{pmatrix} 1/b_m \\ 0 \\ 1/c_m \end{pmatrix}$$

$$\vec{G}(111) = \vec{A} + \vec{B} + \vec{C} = (111)_{mC} = \begin{pmatrix} 1/b_m \\ 1/a_m \\ -\delta/a_m + 1/c_m \end{pmatrix} \approx \begin{pmatrix} 1/a_{pc} \\ 1/a_{pc} \\ 1/a_{pc} \end{pmatrix}$$

For P_3:

$$\vec{a} = a_m \begin{pmatrix} 1 \\ 0 \\ 0 \end{pmatrix}, \quad \vec{b} = b_m \begin{pmatrix} 0 \\ 1 \\ 0 \end{pmatrix}, \vec{c} = c_m \begin{pmatrix} -\delta \\ 0 \\ 1 \end{pmatrix} \qquad V_m \approx a_m b_m c_m$$

Reciprocal lattice vectors $\vec{A}$ etc from the cross-products in lowest order in δ

$$\vec{a} \times \vec{b} = a_m b_m \begin{pmatrix} 1 \\ 0 \\ 0 \end{pmatrix} \times \begin{pmatrix} 0 \\ 1 \\ 0 \end{pmatrix} \approx a_m b_m \begin{pmatrix} 0 \\ 0 \\ 1 \end{pmatrix} \qquad \vec{C} = \frac{\vec{a} \times \vec{b}}{V} = \frac{1}{c_m} \begin{pmatrix} 0 \\ 0 \\ 1 \end{pmatrix}$$

$$\vec{c} \times \vec{a} = c_m a_m \begin{pmatrix} -\delta \\ 0 \\ 1 \end{pmatrix} \times \begin{pmatrix} 1 \\ 0 \\ 0 \end{pmatrix} \approx c_m a_m \begin{pmatrix} 0 \\ 1 \\ 0 \end{pmatrix} \qquad \vec{B} = \frac{1}{b_m} \begin{pmatrix} 0 \\ 1 \\ 0 \end{pmatrix}$$

$$\vec{b} \times \vec{c} = b_m c_m \begin{pmatrix} 0 \\ 1 \\ 0 \end{pmatrix} \times \begin{pmatrix} -\delta \\ 0 \\ 1 \end{pmatrix} \approx b_m c_m \begin{pmatrix} 1 \\ 0 \\ \delta \end{pmatrix} \qquad \vec{A} = \frac{1}{a_m} \begin{pmatrix} 1 \\ 0 \\ \delta \end{pmatrix}$$

$$\vec{G}(101) = \vec{A} + \vec{C} = (101)_{mC} = \begin{pmatrix} 1/a_m \\ 0 \\ \delta/a_m + 1/c_m \end{pmatrix}$$

$$\vec{G}(111) = \vec{A} + \vec{B} + \vec{C} = (111)_{mC} = \begin{pmatrix} 1/a_m \\ 1/b_m \\ \delta/a_m + 1/c_m \end{pmatrix} \approx \begin{pmatrix} 1/a_{pc} \\ 1/a_{pc} \\ 1/a_{pc} \end{pmatrix}$$

For *P*$_4$:

$$\vec{a} = b_m \begin{pmatrix} 1 \\ 0 \\ 0 \end{pmatrix}, \quad \vec{b} = a_m \begin{pmatrix} 0 \\ 1 \\ 0 \end{pmatrix}, \quad \vec{c} = c_m \begin{pmatrix} 0 \\ -\delta \\ 1 \end{pmatrix} \qquad V_m \approx a_m b_m c_m$$

$$\vec{a} \times \vec{b} = a_m b_m \begin{pmatrix} 1 \\ 0 \\ 0 \end{pmatrix} \times \begin{pmatrix} 0 \\ 1 \\ 0 \end{pmatrix} \approx a_m b_m \begin{pmatrix} 0 \\ 0 \\ 1 \end{pmatrix} \qquad \vec{C} = \frac{\vec{a} \times \vec{b}}{V} = \frac{1}{c_m} \begin{pmatrix} 0 \\ 0 \\ 1 \end{pmatrix}$$

$$\vec{c} \times \vec{a} = c_m b_m \begin{pmatrix} 0 \\ -\delta \\ 1 \end{pmatrix} \times \begin{pmatrix} 1 \\ 0 \\ 0 \end{pmatrix} \approx c_m b_m \begin{pmatrix} 0 \\ 1 \\ \delta \end{pmatrix} \qquad \vec{B} = \frac{1}{a_m} \begin{pmatrix} 0 \\ 1 \\ \delta \end{pmatrix}$$

$$\vec{b} \times \vec{c} = a_m c_m \begin{pmatrix} 0 \\ 1 \\ 0 \end{pmatrix} \times \begin{pmatrix} 0 \\ -\delta \\ 1 \end{pmatrix} \approx a_m c_m \begin{pmatrix} 1 \\ 0 \\ 0 \end{pmatrix} \qquad \vec{A} = \frac{1}{b_m} \begin{pmatrix} 1 \\ 0 \\ 0 \end{pmatrix}$$

$$\vec{G}(101) = \vec{A} + \vec{C} = (101)_{mC} = \begin{pmatrix} 1/b_m \\ 0 \\ 1/c_m \end{pmatrix}$$

$$\vec{G}(111) = \vec{A} + \vec{B} + \vec{C} = (111)_{mC} = \begin{pmatrix} 1/b_m \\ 1/a_m \\ \delta/a_m + 1/c_m \end{pmatrix} \approx \begin{pmatrix} 1/a_{pc} \\ 1/a_{pc} \\ 1/a_{pc} \end{pmatrix}$$

Then the asymmetrical RSM (101) and (111) can be constructed as followed:

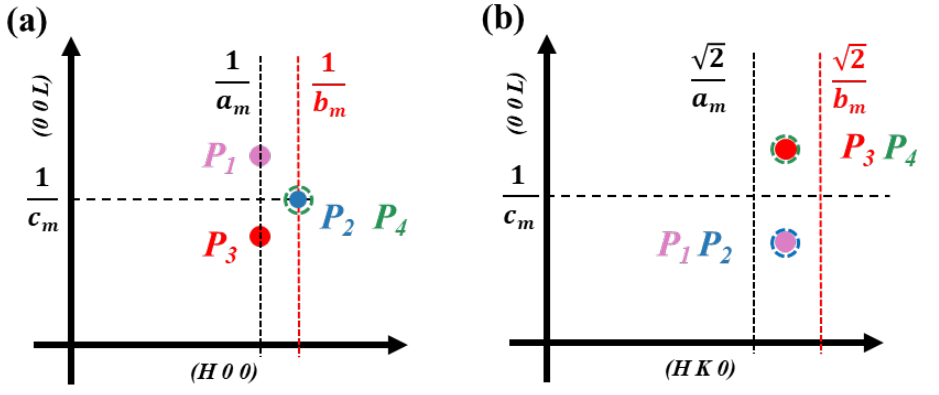

Figure 3.6. *The calculated RSMs of M_c poly-domain pattern in reciprocal plane (101) and (111)*

Considering the monoclinic c-type with tilting:

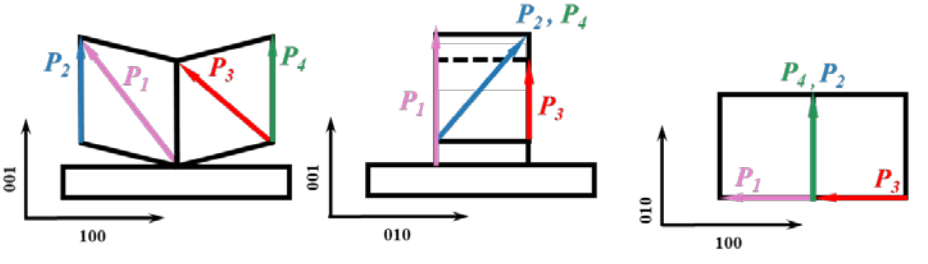

Figure 3.7. *The four possibilities of vector (101) in real monoclinic c-type thin films, respectively. The notations P_1, P_2, P_3 and P_4 represent the reciprocal vector [101] possibilities. With relaxation and tilting, the c-axis of M_c lattices are co-axial.*

Then it can give:

$\vec{a}$-vector is tilted over angle δ from the x-axis, thus x-coordinate of this vector is $a_m cos\delta \approx a_m$ and z-coordinate is $a_m sin\delta \approx a_m \delta$ in lowest order in δ.

$$\vec{a} = a_m \begin{pmatrix} 1 \\ 0 \\ \delta \end{pmatrix}, \quad \vec{b} = b_m \begin{pmatrix} 0 \\ 1 \\ 0 \end{pmatrix}, \vec{c} = c_m \begin{pmatrix} 0 \\ 0 \\ 1 \end{pmatrix} \qquad V_m \approx a_m b_m c_m$$

Now construct the (monoclinic)reciprocal lattice vectors $\vec{A}$ etc from the cross-products in lowest order in δ can be constructed

$$\vec{a} \times \vec{b} = a_m b_m \begin{pmatrix} 1 \\ 0 \\ \delta \end{pmatrix} \times \begin{pmatrix} 0 \\ 1 \\ 0 \end{pmatrix} \approx a_m b_m \begin{pmatrix} -\delta \\ 0 \\ 1 \end{pmatrix} \qquad \vec{C} = \frac{\vec{a} \times \vec{b}}{V} = \frac{1}{c_m} \begin{pmatrix} -\delta \\ 0 \\ 1 \end{pmatrix}$$

$$\vec{c} \times \vec{a} = c_m a_m \begin{pmatrix} 0 \\ 0 \\ 1 \end{pmatrix} \times \begin{pmatrix} 1 \\ 0 \\ \delta \end{pmatrix} \approx c_m a_m \begin{pmatrix} 0 \\ 1 \\ 0 \end{pmatrix} \qquad \vec{B} = \frac{1}{b_m} \begin{pmatrix} 0 \\ 1 \\ 0 \end{pmatrix}$$

$$\vec{b} \times \vec{c} = b_m c_m \begin{pmatrix} 0 \\ 1 \\ 0 \end{pmatrix} \times \begin{pmatrix} 0 \\ 0 \\ 1 \end{pmatrix} \approx b_m c_m \begin{pmatrix} 1 \\ 0 \\ 0 \end{pmatrix} \qquad \vec{A} = \frac{1}{a_m} \begin{pmatrix} 1 \\ 0 \\ 0 \end{pmatrix}$$

$$\vec{G}(101) = \vec{A} + \vec{C} = (101)_{mCt} = \begin{pmatrix} 1/a_m - \delta/c_m \\ 0 \\ 1/c_m \end{pmatrix}$$

$$\vec{G}(111) = \vec{A} + \vec{B} + \vec{C} = (111)_{mCt} = \begin{pmatrix} 1/a_m - \delta/c_m \\ 1/b_m \\ 1/c_m \end{pmatrix}$$

P_2:

$$\vec{a} = b_m \begin{pmatrix} 1 \\ 0 \\ 0 \end{pmatrix}, \quad \vec{b} = a_m \begin{pmatrix} 0 \\ 1 \\ \delta \end{pmatrix}, \vec{c} = c_m \begin{pmatrix} 0 \\ 0 \\ 1 \end{pmatrix} \qquad V_m \approx a_m b_m c_m$$

$$\vec{a} \times \vec{b} = a_m b_m \begin{pmatrix} 1 \\ 0 \\ 0 \end{pmatrix} \times \begin{pmatrix} 0 \\ 1 \\ \delta \end{pmatrix} \approx a_m b_m \begin{pmatrix} 0 \\ -\delta \\ 1 \end{pmatrix} \qquad \vec{C} = \frac{\vec{a} \times \vec{b}}{V} = \frac{1}{c_m} \begin{pmatrix} 0 \\ -\delta \\ 1 \end{pmatrix}$$

$$\vec{c}\times\ \vec{a} = c_m b_m \begin{pmatrix}0\\0\\1\end{pmatrix}\times\begin{pmatrix}1\\0\\0\end{pmatrix} \approx c_m b_m \begin{pmatrix}0\\1\\0\end{pmatrix} \qquad \vec{B} = \frac{1}{a_m}\begin{pmatrix}0\\1\\0\end{pmatrix}$$

$$\vec{b}\times\ \vec{c} = a_m c_m \begin{pmatrix}0\\1\\\delta\end{pmatrix}\times\begin{pmatrix}0\\0\\1\end{pmatrix} \approx a_m c_m \begin{pmatrix}1\\0\\0\end{pmatrix} \qquad \vec{A} = \frac{1}{b_m}\begin{pmatrix}1\\0\\0\end{pmatrix}$$

$$\vec{G}(101) = \vec{A} + \vec{C} = (101)_{mCt} = \begin{pmatrix}1/b_m\\-\delta/c_m\\1/c_m\end{pmatrix}$$

$$\vec{G}(111) = \vec{A} + \vec{B} + \vec{C} = (111)_{mCt} = \begin{pmatrix}1/b_m\\1/a_m - \delta/c_m\\1/c_m\end{pmatrix}$$

P_3 :

$$\vec{a} = a_m\begin{pmatrix}1\\0\\-\delta\end{pmatrix}, \qquad \vec{b} = b_m\begin{pmatrix}0\\1\\0\end{pmatrix},\ \vec{c} = c_m\begin{pmatrix}0\\0\\1\end{pmatrix} \quad V_m \approx a_m b_m c_m$$

$$\vec{a}\times\ \vec{b} = a_m b_m \begin{pmatrix}1\\0\\-\delta\end{pmatrix}\times\begin{pmatrix}0\\1\\0\end{pmatrix} \approx a_m b_m \begin{pmatrix}\delta\\0\\1\end{pmatrix} \qquad \vec{C} = \frac{\vec{a}\times\vec{b}}{V} = \frac{1}{c_m}\begin{pmatrix}\delta\\0\\1\end{pmatrix}$$

$$\vec{c}\times\ \vec{a} = c_m a_m \begin{pmatrix}0\\0\\1\end{pmatrix}\times\begin{pmatrix}1\\0\\-\delta\end{pmatrix} \approx c_m a_m \begin{pmatrix}0\\1\\0\end{pmatrix} \qquad \vec{B} = \frac{1}{b_m}\begin{pmatrix}0\\1\\0\end{pmatrix}$$

$$\vec{b}\times\ \vec{c} = b_m c_m \begin{pmatrix}0\\1\\0\end{pmatrix}\times\begin{pmatrix}0\\0\\1\end{pmatrix} \approx b_m c_m \begin{pmatrix}1\\0\\0\end{pmatrix} \qquad \vec{A} = \frac{1}{a_m}\begin{pmatrix}1\\0\\0\end{pmatrix}$$

$$\vec{G}(101) = \vec{A} + \vec{C} = (101)_{mCt} = \begin{pmatrix}1/a_m + \delta/c_m\\0\\1/c_m\end{pmatrix}$$

$$\vec{G}(111) = \vec{A} + \vec{B} + \vec{C} = (111)_{mCt} = \begin{pmatrix}1/a_m + \delta/c_m\\1/b_m\\1/c_m\end{pmatrix}$$

P_4 :

$$\vec{a} = b_m \begin{pmatrix} 1 \\ 0 \\ 0 \end{pmatrix}, \quad \vec{b} = a_m \begin{pmatrix} 0 \\ 1 \\ -\delta \end{pmatrix}, \qquad \vec{c} = c_m \begin{pmatrix} 0 \\ 0 \\ 1 \end{pmatrix} \qquad V_m \approx a_m b_m c_m$$

$$\vec{a} \times \vec{b} = a_m b_m \begin{pmatrix} 1 \\ 0 \\ 0 \end{pmatrix} \times \begin{pmatrix} 0 \\ 1 \\ -\delta \end{pmatrix} \approx a_m b_m \begin{pmatrix} 0 \\ \delta \\ 1 \end{pmatrix} \qquad \vec{C} = \frac{\vec{a} \times \vec{b}}{V} = \frac{1}{c_m} \begin{pmatrix} 0 \\ \delta \\ 1 \end{pmatrix}$$

$$\vec{c} \times \vec{a} = c_m b_m \begin{pmatrix} 0 \\ 0 \\ 1 \end{pmatrix} \times \begin{pmatrix} 1 \\ 0 \\ 0 \end{pmatrix} \approx c_m b_m \begin{pmatrix} 0 \\ 1 \\ 0 \end{pmatrix} \qquad \vec{B} = \frac{1}{a_m} \begin{pmatrix} 0 \\ 1 \\ 0 \end{pmatrix}$$

$$\vec{b} \times \vec{c} = a_m c_m \begin{pmatrix} 0 \\ 1 \\ -\delta \end{pmatrix} \times \begin{pmatrix} 0 \\ 0 \\ 1 \end{pmatrix} \approx a_m c_m \begin{pmatrix} 1 \\ 0 \\ 0 \end{pmatrix} \qquad \vec{A} = \frac{1}{b_m} \begin{pmatrix} 1 \\ 0 \\ 0 \end{pmatrix}$$

$$\vec{G}(101) = \vec{A} + \vec{C} = (101)_{mCt} = \begin{pmatrix} 1/b_m \\ \delta/c_m \\ 1/c_m \end{pmatrix}$$

$$\vec{G}(111) = \vec{A} + \vec{B} + \vec{C} = (111)_{mCt} = \begin{pmatrix} 1/b_m \\ 1/a_m + \delta/c_m \\ 1/c_m \end{pmatrix}$$

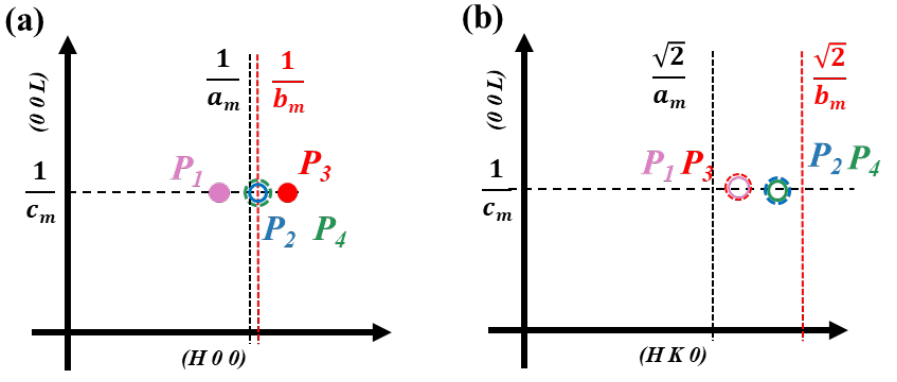

Figure 3.8. *The calculated RSMs of tilted M_c poly-domain pattern for the reciprocal planes (101) and (111)*

3.4. Monoclinic symmetry (A-type)

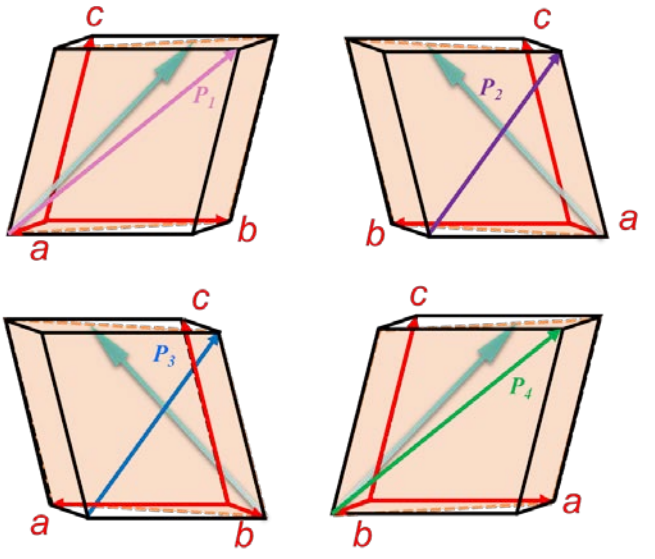

Figure 3.9. *The four possibilities of vector (101) in real M_A thin films, respectively. The green arrow represents the polarisation orientation in (110) plane. The red arrows are M_A lattice co-ordination axis. The notations P_1, P_2, P_3 and P_4 represent the possibilities for the [101] reciprocal vector.*

P_1 :

Monoclinic unit cell vectors in cubic coordinates

$\vec{c}_m$-vector is tilted over angle β from the z-axis in the $\vec{a}_m$ direction, thus x and y-coordinate of this vector are $c_m sin\delta \approx c_m \delta$ with and z-coordinate is $c_m cos\delta \approx c_m$ in lowest order in δ.

$$\vec{a} = a_m \begin{pmatrix} 1/\sqrt{2} \\ 1/\sqrt{2} \\ 0 \end{pmatrix}, \quad \vec{b} = b_m \begin{pmatrix} -1/\sqrt{2} \\ 1/\sqrt{2} \\ 0 \end{pmatrix}, \vec{c}_m = c_m \begin{pmatrix} \delta \\ \delta \\ 1 \end{pmatrix} \; V_m \approx a_m b_m c_m$$

Now construct the (monoclinic)reciprocal lattice vectors $\vec{A}$ etc from the cross-products in lowest order in δ

$$\vec{a} \times \vec{b} = a_m b_m \begin{pmatrix} 1/\sqrt{2} \\ 1/\sqrt{2} \\ 0 \end{pmatrix} \times \begin{pmatrix} -/\sqrt{2} \\ 1/\sqrt{2} \\ 0 \end{pmatrix} \approx a_m b_m \begin{pmatrix} 0 \\ 0 \\ 1 \end{pmatrix}$$

$$\vec{c} \times \vec{a} = c_m a_m \begin{pmatrix} \delta \\ \delta \\ 1 \end{pmatrix} \times \begin{pmatrix} 1/\sqrt{2} \\ 1/\sqrt{2} \\ 0 \end{pmatrix} \approx c_m a_m \begin{pmatrix} -1/\sqrt{2} \\ 1/\sqrt{2} \\ 0 \end{pmatrix}$$

$$\vec{b} \times \vec{c} = b_m c_m \begin{pmatrix} -1/\sqrt{2} \\ 1/\sqrt{2} \\ 0 \end{pmatrix} \times \begin{pmatrix} \delta \\ \delta \\ 1 \end{pmatrix} \approx b_m c_m \begin{pmatrix} 1/\sqrt{2} \\ 1/\sqrt{2} \\ -2\delta/\sqrt{2} \end{pmatrix}$$

$$\vec{C} = \frac{\vec{a} \times \vec{b}}{V} = \frac{1}{c_m} \begin{pmatrix} 0 \\ 0 \\ 1 \end{pmatrix} \vec{A} = \frac{1}{a_m} \begin{pmatrix} 1/\sqrt{2} \\ 1/\sqrt{2} \\ -\sqrt{2}\delta \end{pmatrix} \vec{B} = \frac{1}{b_m} \begin{pmatrix} -1/\sqrt{2} \\ 1/\sqrt{2} \\ 0 \end{pmatrix}$$

$$\vec{G}(201)_c = \left(\vec{A} - \vec{B} + \vec{C}\right)_m = (111)_{mA} = \begin{pmatrix} 1/\sqrt{2}a_m + 1/\sqrt{2}b_m \\ 0 \\ -\sqrt{2}\delta/a_m + 1/c_m \end{pmatrix} \approx \begin{pmatrix} 2/a_{pc} \\ 0 \\ -\delta/a_{pc} + 1/a_{pc} \end{pmatrix}$$

assuming $a_m \approx b_m \approx \sqrt{2} a_{pc} \approx \sqrt{2} c_m$.

$$\vec{G}(112)_c = 2\left(\vec{A} + \vec{C}\right)_m = (202)_{mA} = 2 \begin{pmatrix} 1/\sqrt{2}a_m \\ 1/\sqrt{2}a_m \\ -\sqrt{2}\delta/a_m + 1/c_m \end{pmatrix} \approx \begin{pmatrix} 1/a_{pc} \\ 1/a_{pc} \\ -2\delta/a_{pc} + 2/a_{pc} \end{pmatrix}$$

Thus in Qx-Qy plane the reflection is at half the Q-values of the (111) reflection of the substrate

P₂ :

$$\vec{a} = a_m \begin{pmatrix} -1/\sqrt{2} \\ 1/\sqrt{2} \\ 0 \end{pmatrix}, \qquad \vec{b} = a_m \begin{pmatrix} -1/\sqrt{2} \\ -1/\sqrt{2} \\ 0 \end{pmatrix}, \vec{c}_m = c_m \begin{pmatrix} -\delta \\ \delta \\ 1 \end{pmatrix} \qquad V_m \approx a_m b_m c_m$$

Now the (monoclinic)reciprocal lattice vectors $\vec{A}$ etc can be constructed from the cross-products in lowest order in δ

$$\vec{a} \times \vec{b} = a_m b_m \begin{pmatrix} -1/\sqrt{2} \\ 1/\sqrt{2} \\ 0 \end{pmatrix} \times \begin{pmatrix} -1/\sqrt{2} \\ -1/\sqrt{2} \\ 0 \end{pmatrix} \approx a_m b_m \begin{pmatrix} 0 \\ 0 \\ 1 \end{pmatrix}$$

$$\vec{c} \times \vec{a} = c_m a_m \begin{pmatrix} -\delta \\ \delta \\ 1 \end{pmatrix} \times \begin{pmatrix} -1/\sqrt{2} \\ 1/\sqrt{2} \\ 0 \end{pmatrix} \approx c_m a_m \begin{pmatrix} -1/\sqrt{2} \\ -1/\sqrt{2} \\ 0 \end{pmatrix}$$

$$\vec{b}\times\ \vec{c} = b_m c_m \begin{pmatrix} -1/\sqrt{2} \\ -1/\sqrt{2} \\ 0 \end{pmatrix} \times \begin{pmatrix} -\delta \\ \delta \\ 1 \end{pmatrix} \approx b_m c_m \begin{pmatrix} -1/\sqrt{2} \\ 1/\sqrt{2} \\ -(2\delta/\sqrt{2}) \end{pmatrix}$$

$$\vec{C} = \frac{\vec{a}\times\vec{b}}{V} = \frac{1}{c_m}\begin{pmatrix} 0 \\ 0 \\ 1 \end{pmatrix} \vec{A} = \frac{1}{a_m}\begin{pmatrix} -1/\sqrt{2} \\ 1/\sqrt{2} \\ -\sqrt{2}\delta \end{pmatrix}\ \vec{B} = \frac{1}{b_m}\begin{pmatrix} -1/\sqrt{2} \\ -1/\sqrt{2} \\ 0 \end{pmatrix}$$

$$\vec{G}(201)_c = \left(-\vec{A} - \vec{B} + \vec{C}\right)_m = (-1-11)_{mA} = \begin{pmatrix} 1/\sqrt{2}a_m + 1/\sqrt{2}b_m \\ 0 \\ \delta\sqrt{2}/a_m + 1/c_m \end{pmatrix}$$

$$\approx \begin{pmatrix} 2/a_{pc} \\ 0 \\ \delta/a_{pc} + 1/a_{pc} \end{pmatrix}$$

$$\vec{G}(112)_c = 2\left(-\vec{B} + \vec{C}\right)_m = (0-22)_{mA} = 2\begin{pmatrix} 1/\sqrt{2}b_m \\ 1/\sqrt{2}b_m \\ 1/c_m \end{pmatrix} \approx \begin{pmatrix} 1/a_{pc} \\ 1/a_{pc} \\ 2/a_{pc} \end{pmatrix}$$

P_3 :

$$\vec{a} = a_m \begin{pmatrix} -1/\sqrt{2} \\ -1/\sqrt{2} \\ 0 \end{pmatrix}\ \vec{b} = b_m \begin{pmatrix} 1/\sqrt{2} \\ -1/\sqrt{2} \\ 0 \end{pmatrix}\ \vec{c}_m = c_m \begin{pmatrix} -\delta \\ -\delta \\ 1 \end{pmatrix}\ \ V_m \approx a_m b_m c_m$$

$$\vec{a}\times\ \vec{b} = a_m b_m \begin{pmatrix} -1/\sqrt{2} \\ -1/\sqrt{2} \\ 0 \end{pmatrix} \times \begin{pmatrix} 1/\sqrt{2} \\ -1/\sqrt{2} \\ 0 \end{pmatrix} \approx a_m b_m \begin{pmatrix} 0 \\ 0 \\ 1 \end{pmatrix}$$

$$\vec{c}\times\ \vec{a} = c_m b_m \begin{pmatrix} -\delta \\ -\delta \\ 1 \end{pmatrix} \times \begin{pmatrix} -1/\sqrt{2} \\ -1/\sqrt{2} \\ 0 \end{pmatrix} \approx c_m a_m \begin{pmatrix} 1/\sqrt{2} \\ -1/\sqrt{2} \\ 0 \end{pmatrix}$$

$$\vec{b}\times\ \vec{c} = a_m c_m \begin{pmatrix} 1/\sqrt{2} \\ -1/\sqrt{2} \\ 0 \end{pmatrix} \times \begin{pmatrix} -\delta \\ -\delta \\ 1 \end{pmatrix} \approx b_m c_m \begin{pmatrix} -1/\sqrt{2} \\ -1/\sqrt{2} \\ -2\delta/\sqrt{2} \end{pmatrix}$$

$$\vec{C} = \frac{\vec{a}\times\vec{b}}{V} = \frac{1}{c_m}\begin{pmatrix} 0 \\ 0 \\ 1 \end{pmatrix}\ \vec{A} = \frac{1}{a_m}\begin{pmatrix} -1/\sqrt{2} \\ -1/\sqrt{2} \\ -\sqrt{2}\delta \end{pmatrix}\ \vec{B} = \frac{1}{b_m}\begin{pmatrix} 1/\sqrt{2} \\ -1/\sqrt{2} \\ 0 \end{pmatrix}$$

$$\vec{G}(201)_c = \left(-\vec{A} + \vec{B} + \vec{C}\right)_m = (-111)_{mA} = \begin{pmatrix} 1/\sqrt{2}a_m + 1/\sqrt{2}b_m \\ 0 \\ \delta\sqrt{2}/a_m + 1/c_m \end{pmatrix} \approx \begin{pmatrix} 2/a_{pc} \\ 0 \\ \delta/a_{pc} + 1/a_{pc} \end{pmatrix}$$

$$\vec{G}(112)_c = 2\left(-\vec{A}+\vec{C}\right)_m = (-202)_{mA} = 2\begin{pmatrix} 1/\sqrt{2}a_m \\ 1/\sqrt{2}a_m \\ \delta\sqrt{2}/a_m + 1/c_m \end{pmatrix} \approx \begin{pmatrix} 1/a_{pc} \\ 1/a_{pc} \\ 2\delta/a_{pc} + 2/a_{pc} \end{pmatrix}$$

P4:

$$\vec{a} = a_m\begin{pmatrix} 1/\sqrt{2} \\ -1/\sqrt{2} \\ 0 \end{pmatrix}, \qquad \vec{b} = b_m\begin{pmatrix} 1/\sqrt{2} \\ 1/\sqrt{2} \\ 0 \end{pmatrix}, \quad \vec{c}_m = c_m\begin{pmatrix} \delta \\ -\delta \\ 1 \end{pmatrix}$$

$$\vec{a} \times \vec{b} = a_m b_m\begin{pmatrix} 1/\sqrt{2} \\ -1/\sqrt{2} \\ 0 \end{pmatrix} \times \begin{pmatrix} 1/\sqrt{2} \\ 1/\sqrt{2} \\ 0 \end{pmatrix} \approx a_m b_m \begin{pmatrix} 0 \\ 0 \\ 1 \end{pmatrix}$$

$$\vec{c} \times \vec{a} = c_m a_m\begin{pmatrix} \delta \\ -\delta \\ 1 \end{pmatrix} \times \begin{pmatrix} 1/\sqrt{2} \\ -1/\sqrt{2} \\ 0 \end{pmatrix} \approx c_m a_m \begin{pmatrix} 1/\sqrt{2} \\ 1/\sqrt{2} \\ 0 \end{pmatrix}$$

$$\vec{b} \times \vec{c} = b_m c_m\begin{pmatrix} 1/\sqrt{2} \\ 1/\sqrt{2} \\ 0 \end{pmatrix} \times \begin{pmatrix} \delta \\ -\delta \\ 1 \end{pmatrix} \approx b_m c_m \begin{pmatrix} 1/\sqrt{2} \\ -1/\sqrt{2} \\ -2\delta/\sqrt{2} \end{pmatrix}$$

$$\vec{C} = \frac{\vec{a}\times\vec{b}}{V} = \frac{1}{c_m}\begin{pmatrix} 0 \\ 0 \\ 1 \end{pmatrix} \vec{A} = \frac{1}{a_m}\begin{pmatrix} 1/\sqrt{2} \\ -1/\sqrt{2} \\ -\sqrt{2}\delta \end{pmatrix} \vec{B} = \frac{1}{b_m}\begin{pmatrix} 1/\sqrt{2} \\ 1/\sqrt{2} \\ 0 \end{pmatrix}$$

$$\vec{G}(201)_c = \left(\vec{A}+\vec{B}+\vec{C}\right)_m = (111)_{mA} = \begin{pmatrix} 1/\sqrt{2}a_m + 1/\sqrt{2}b_m \\ 0 \\ -\delta\sqrt{2}/a_m + 1/c_m \end{pmatrix} \approx \begin{pmatrix} 2/a_{pc} \\ 0 \\ -\delta/a_{pc} + 1/a_{pc} \end{pmatrix}$$

$$\vec{G}(112)_c = 2\left(\vec{B}+\vec{C}\right)_m = (022)_{mA} = 2\begin{pmatrix} 1/\sqrt{2}b_m \\ 1/\sqrt{2}b_m \\ 1/c_m \end{pmatrix} \approx \begin{pmatrix} 1/a_{pc} \\ 1/a_{pc} \\ 2/a_{pc} \end{pmatrix}$$

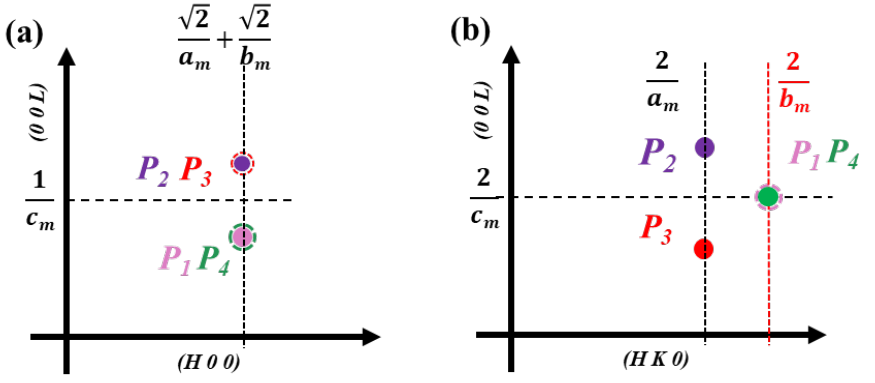

Figure 3.10. *The calculated RSMs of tilted M_A poly-domain pattern in reciprocal plane (101) and (111)*

3.5. Conclusion

To summarise, we established the mathematical expressions to predict the RSMs pattern of poly-domain thin films. Tetragonal symmetry with a/b/c domains, rhombohedral symmetry, monoclinic symmetry c-type and a-type are calculated and presented. Furthermore, reciprocal space maps of asymmetrical planes (101) and (111) are given. The calculated RSM patten results fit reported RSMs, such as tetragonal $BiFeO_3$ in a phase transition, rhombohedral $LaNiO_3$ with great compressive strain, rhombohedral $BiFeO_3$, monoclinic c-type $BiFeO_3$, monoclinic a-type $BiFeO_3$ and monoclinic c-type VO_2.[2-7] Moreover, this description system also should be the simple than other reciprocal space mathematical description, such as Niggli cell and Bravais lattice conversion, which involves a 6-dimensional Euclidean space. Hence this approach is potentially helpful as a guide to determine the symmetry from RSMs measurements.[8]

		101		111	
Tetragonal	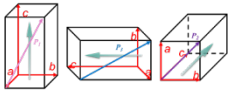	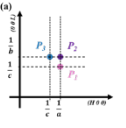	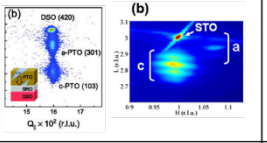	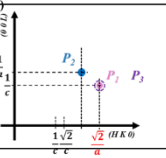	
rhombohedral	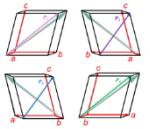	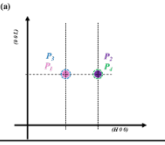	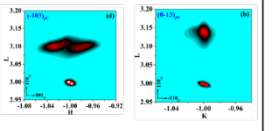	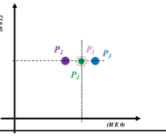	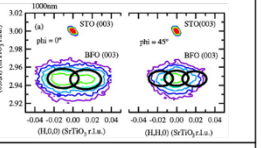
Monoclinic C-type	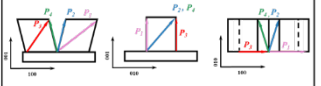	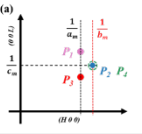	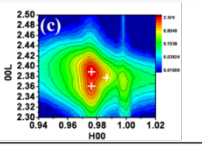	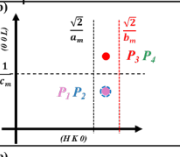	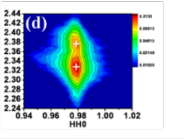
Monoclinic A-type	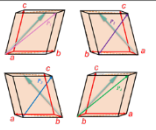	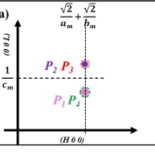	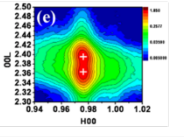	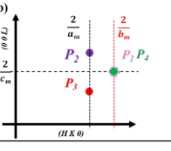	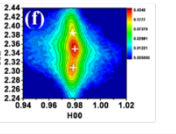

Table 3.1. *Reproduced from [9-12], with the permission of AIP Publishing, Reproduced from [13], with the permission of American Physical Society.*

Reference:

1. Neumayer, J., *The Rhombohedral Unit Cell.* Student Project, 06.01.2011.
2. Christen, H.M., et al., *Stress-induced R− M A− M C− T symmetry changes in BiFeO 3 films.* Physical Review B, 2011. **83**(14): p. 144107.
3. Chen, Z., et al., *Low-symmetry monoclinic phases and polarization rotation path mediated by epitaxial strain in multiferroic BiFeO3 thin films.* Advanced Functional Materials, 2011. **21**(1): p. 133-138.
4. Qiu, H., et al., *The tetragonal-like to rutile structural phase transition in epitaxial VO2/TiO2 (001) thick films.* New Journal of Physics, 2015. **17**(11): p. 113016.
5. Frano, A., et al., *Layer selective control of the lattice structure in oxide superlattices.* Advanced Materials, 2014. **26**(2): p. 258-262.
6. Liu, H., et al., *Growth rate induced monoclinic to tetragonal phase transition in epitaxial BiFeO 3 (001) thin films.* Applied Physics Letters, 2011. **98**(10): p. 102902.
7. Xu, H., et al., *Mixture domain states in PbTiO3 film with potentials for functional application.* Applied Physics Letters, 2019. **114**(24): p. 242901.
8. Yang, P., et al., *Unit-cell determination of epitaxial thin films based on reciprocal-space vectors by high-resolution X-ray diffractometry.* Journal of Applied Crystallography, 2014. **47**(1): p. 402-413.
9. Liu, H.-J., et al., *Structural study in highly compressed BiFeO3 epitaxial thin films on YAlO3.* Journal of Applied Physics, 2012. **112**(5): p. 052002.
10. Kan, D. and I. Takeuchi, *Effect of substrate orientation on lattice relaxation of epitaxial BiFeO 3 thin films.* Journal of Applied Physics, 2010. **108**(1): p. 014104.
11. Sarott, M.F., M. Fiebig, and M. Trassin, *Tracking ferroelectric domain formation during epitaxial growth of PbTiO3 films.* Applied Physics Letters, 2020. **117**(13): p. 132901.
12. Hubault, C., et al., *Inhibition of polydomain formation in PbTiO3/PbZr0. 2Ti0. 8O3 superlattices by intercalation of ultra-thin SrTiO3 layers.* Applied Physics Letters, 2011. **99**(5): p. 052905.
13. Chen, Z., et al., *Large tensile-strain-induced monoclinic M B phase in BiFeO 3 epitaxial thin films on a PrScO 3 substrate.* Physical Review B, 2013. **88**(5): p. 054114.

Chapter 4 Substrate induced thermal strain-enhanced piezoelectricity in $PbZr_{0.6}Ti_{0.4}O_3$ piezoelectric

Lead based bulk piezoelectrical materials, e.g. $PbZr_xTi_{1-x}O_3$(PZT) in sensors and transducers nowadays are widely used in electromechanical applications, for which optimally performing thin films are needed. Several theoretical reports were published on the influence of thermal strain on the piezoelectric properties (d_{33}) in PZT thin films, also predicting significant enhancement of this property.{Groenen, 2016 #63} In this work, we successfully demonstrate the applicability of these models for PZT(x=0.6) thin films grown on CaF_2, $SrTiO_3$(STO) and 70% $PbMg_{1/3}Nb_{2/3}O_3$-30%$PbTiO_3$(PMN-PT) substrates by pulsed laser deposition. The different substrates provide different thermal misfit strains, leading to experimentally observed and theoretically predicted d_{33} values of 32 pm/V, 140 pm/V and 81 pm/V, respectively. We characterised the PZT films with temperature dependent X-ray reciprocal space mapping (RSM) and grazing incidence diffraction (GI-XRD), transmission electron microscopy (TEM) in bright field (BF) and dark field (DF) modes as well as selected area diffraction (SEAD) convergent beam electron diffraction (CBED) and piezoresponse force microscopy (PFM). The Zr/Ti ratio has been confirmed by Rutherford Backscattering Spectrometry (RBS). The PZT(x=0.6) film which in bulk has a rhombohedral lattice symmetry, is at room temperature on STO in a relaxed monoclinic phase, which has been observed for the first time for this composition. With this research we demonstrate that the thermal misfit strain has a significant effect on the structural and piezoelectric properties of PZT films.

4.1. Introduction

PZT is one of the most used ferroelectric and piezoelectric solid solution materials because of the high values of its room temperature polarisation and piezo-electric coefficients, as compared to other ferroelectric materials, as for example $BaTiO_3$, and piezoelectric materials such as quartz. A successful strategy to improve the piezoelectric response of bulk PZT is to use the Zr/Ti composition ratio at the morphotropic phase boundary (MPB) in the PZT phase diagram.[1] Both the polarisation rotation mechanism[2, 3] and easy domain wall motions[4] attribute to

the enhancement of the piezoelectricity of this composition. The easy polarisation rotation in the (1-10) plane benefits from a lower energy barrier between two stable symmetries. It was about two decades ago when the stable monoclinic symmetry was first predicted and then found to be present at the MPB at low temperatures.[3] This discovery gave insight in the complex nature of the phase transition from the Zr-rich rhombohedral phase to the Ti-rich tetragonal side in the phase diagram.[5-7] Furthermore, it helped to deepen the understanding of the structural properties at the MPB and assisted the development of a phenomenological theory.

The Landau-Ginzburg-Devonshire (LGD) thermodynamic model of ferroelectric materials presents a tool to successfully analyse ferroelectric phase transitions and domain pattern formation in bulk material, especially in well-ordered single crystals. In ferroelectric thin films, multiple extrinsic effects play an important role that have been neglected in the general LGD equation. Limiting the discussion to epitaxially grown films, the ferroelectric structure consists of multiple domains, separated by domain walls; the film is usually under substrate induced thermal strain, and domain wall motion under influence of an applied field contributes significantly to the ferroelectric and piezoelectric properties of the film. Houwman et al. developed a what was called a 'three-domain model' (on the basis of earlier work by Khukar, Pertsev et al. of, what might be called a 'two-domain' model.[8-11] The boundary conditions applied to the formalism of Khukar et al. and which led to the three-domain model, were believed to be more realistic.) Early experimental work on films with tetragonal composition (PZT(x=0.4) supported the applicability of the model.[8] The present experimental study serves also as further support of the model. The three-domain model connects domain wall motion, external elastic and electric field to intrinsic ferroelectric and piezoelectric properties of a clamped films.[8] Using this model, Vergeer produced a series of predictions of the piezoelectric behaviour and crystal symmetry transition as function of the substrate misfit strain due to thermal expansion mismatch for different compositions.[12] Different from the well-known epitaxial misfit strain,[13, 14] the influence of thermal expansion misfit strain has not been discussed extensively in literature. The difference is that for thermal expansion misfit strain one assumes that the bulk of the film is fully relaxed at deposition temperature and the strain built up during cooling down to room temperature. Because the film is thick, the stress build up with varying

temperature, can be relaxed by domain formation in the bulk of the film. For epitaxial misfit strain one assumes that the film grows cube on cube to the substrate and the in-plane lattice constants of the film follow that of the substrate with varying temperature. The model calculations by Vergeer indicate that the thermal misfit strain is able to induce a stable monoclinic phase for x = 0.6 PZT at room temperature,[12] in contrast to the rhombohedral symmetry of the bulk phase diagram.[15] By changing the substrate Thermal expansion Coefficient (CTE), a different phase of PZT is expected. Here, it is shown that a tetragonal phase is expected when the film is grown on CaF_2; a monoclinic phase for STO and a rhombohedral phase for growth on PMN-PT. Especially for the monoclinic phase, one expects enhanced ferroelectric and piezoelectric properties, in analogy with the properties of PZT with a MPB composition. It is for this strong change in piezoelectric properties that we chose to study the PZT (x=0.6) composition. In this work, we show that the thermal expansion misfit strain influences the structural phases observed in PZT thin films. In addition, we show that one can use the thermal expansion misfit strain as an effective manipulation mechanism to enhance piezoelectric properties.

Pulsed laser deposition was applied to fabricate (001)-oriented, 1μm thick PZT (x=0.6) films, with a 40 nm bottom electrode $SrRuO_3$ (SRO) on single crystal substrates of CaF_2(001) (named PZT-C), on STO (001) (named PZT-S) and on PMN-PT (001) (named PZT-P), respectively. No top electrode is deposited. The thickness of 1 μm is deliberately chosen to ensure that the PZT is close to be free from the influence of epitaxial strain from the substrate. Cubic STO has a cubic lattice constant of 3.905Å at room temperature, with an almost constant CTE of $11\times10^{-6}\,K^{-1}$ down to -163°C.[16] The used rhombohedral PMN70-PT30 substrate material exhibits a paraelectric-ferroelectric phase transition when cooling through the Curie point of 125°C.[17] The CTE is highly temperature dependent and changes to $3.1\times10^{-6}\,K^{-1}$ at room temperature in the rhombohedral phase (lattice constants are a = 4.019Å, with α = 89.91° at 25°C), [18] to $10.7\times10^{-6}\,K^{-1}$ in the cubic phase(a = 4.020 Å, α = 90° approximately 300°C). [19, 20] Cubic CaF_2 has a cubic lattice structure with lattice parameter a = b = 5.45 Å at room temperature, and a constant CTE of $18\times10^{-6}\,K^{-1}$. The topographic information on the sample surface was obtained by atomic force microscopy (AFM) and, in addition, the ferroelectric domain pattern

was studied using piezoresponse force microscopy (PFM). The film thickness and quality of the films crystallisation were examined by X-ray diffraction (XRD). Temperature dependant reciprocal space maps (RSMs) were used to define the lattice strain and symmetry at different temperatures.

4.2. Results and Discussion

4.2.1. Phenomenological Approach and Phase Diagram

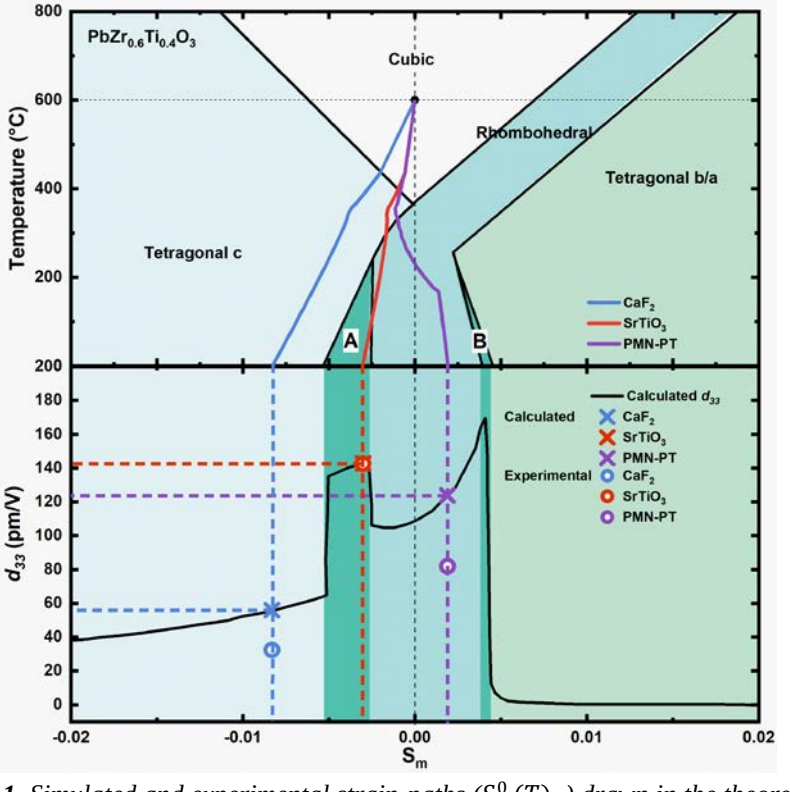

Figure 4.1. *Simulated and experimental strain-paths ($S_m^0(T)$) drawn in the theoretical phase diagram of PZT(x=0.6), derived from the three-domain model from Houwman and Vergeer et al.[8, 12] the model predicts a tetragonal single (out-of-plane oriented) domain c-phase for compressive thermal misfit strain larger than 0.005; The central region for stress around $S_m^0 = 0$ is predicted to have a rhombohedral symmetry, and for S_m^0 > 0.005 a tetragonal (in-plane) a/b domain and b domain. The intermediate regions*

are marked as region A and region B are predicted as mixture phase of tetragonal a/b/c and forming bridges between the rhombohedral and tetragonal phases. At high temperatures above T_c the PZT is in the cubic phase. The blue, red and purple paths stand for the temperature PZT misfit strain of PZT grown on CaF_2, STO and PMN-PT substrates at a deposition temperature of 600°C, respectively. The dashed lines indicate the simulated paths, the solid lines with data points are obtained from experimental data. Theoretical d_{33} as function of the room temperature strains of the three samples. Crosses stand for the predicted piezoelectric response upon each substrate, while the circles strand for the experimental d_{33} values. The plot is reused with permission[12].

In order to be able to interpret our experimental results in terms of the three-domain model, an estimate of the substrate induced thermal misfit strain as function of temperature, $S_m^0(T)$. In the supplementary information we summarize the analysis of Houwman et al. on how to calculate $S_m^0(T)$, including the effect of unit cell expansion due to the paraelectric-ferroelectric phase transition when cooling down through the Curie temperature.

We evaluated the thermal strain of PZT(x=0.6) at all temperatures between deposition temperature and room temperature for the used substrates and plotted this $S_m^0(T)$ path in the phase diagram evaluated by Vergeer. The different paths in the phase diagram are shown in **Figure 4.1**. [12]

In addition, Vergeer gives the piezoelectric response (d_{33}) as function of the thermal misfit strain for this PZT composition. The d_{33} (S_m^0) dependence shows large and stepwise changes of d_{33} as function of the strain in the strain range that is accessible with substrates on which PZT can be grown heteroepitaxially (S_m^0 can in practice be varied from about -0.01 to 0.005). The composition PZT (x = 0.6) was chosen for this reason. The calculations based on the three-domain model indicate that compositions with larger Ti-content show no variation in d_{33} in this strain range.[8]

The phase diagram indicates that, when using a STO substrate, on cooling from the deposition temperature at 600°C down to room temperature the film changes from the paraelectric cubic phase into a single domain, tetragonal c-domain (long axis perpendicular to the substrate) near 400°C. On further cooling, the film enters the

rhombohedral phase at approximately 300℃. The thermal misfit strain path ends on the phase boundary between the tetragonal a/b/c region and the rhombohedral phase. With the PMN-PT substrate, the PZT-P thermal misfit strain follows another path. The cubic phase to tetragonal c-phase transition is at a slightly higher temperature. The path ends at room temperature deep in the rhombohedral phase region with a small tensile strain. The strong curvature in the path is due to the strong temperature dependence of the CTE of the PMN-PT substrate. The model predicts that both PZT-S and PZT-P show an intermediate tetragonal c-phase before the structure becomes rhombohedral, which is very different from the well-know PZT phase diagram[15], in which there is no such intermediate tetragonal phase in the 300℃-400℃ temperature range for PZT at x = 0.6 composition, neither the existence of a mixture tetragonal a/b/c phase. The phase diagram also shows a compressive thermal misfit strain path if using CaF_2 substrate. The $S_m^0(T)$ path is from cubic phase into tetragonal c phase during the cooling at about 437℃, the then ends with a 0.0075 compressive thermal misfit strain at room temperature. The composition PZT(x=0.6) was particularly selected due to its highest d_{33} in the phase diagram prediction.

*4.2.2. Experimental results and discussion*s

4.2.2.1. PZT on PMN-PT substrate (PZT-P)

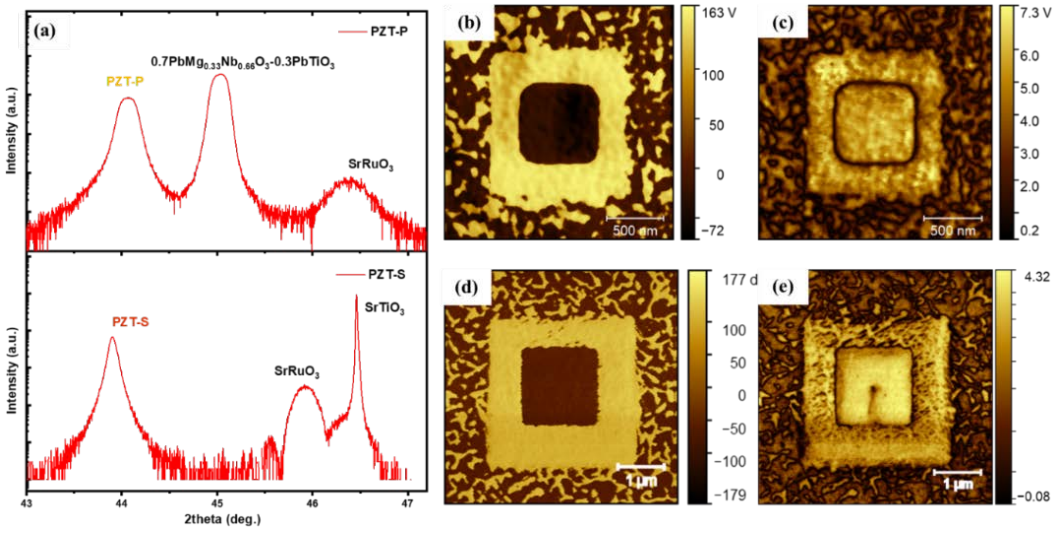

Figure 4.2. *(a) The XRD 2-theta (002) scan of PZT-P (top panel) and PZT-S (bottom panel). PFM vertical phase information of PZT-P (b) and PZT-S (d) after lithograph writing with upward oriented polarisation (inner dark square) and downward oriented polarisation (outer bright square loop), individually. The PFM amplitude of PZT-P (c) and of PZT-S. (e).*

The PZT on PMN-PT substrate is denoted as PZT-P here, the PZT film quality is characterised by XRD and PFM. From the PZT bulk phase diagram, we expect this (x=0.6) composition to be rhombohedral. With **Figure 4.2.a** top panel, XRD at room temperature shows a PMN-PT substrate around diffraction (002) peak at 45º, which is characterised by, unlike most single crystal substrates, a relatively broader full width at half maximum of about 0.2°. The large FWHM of the PMN-PT is copied in the large peak widths of the pseudocubic (220) peak of $SrRuO_3$(SRO) bottom electrode layer at 46.4º and the PZT-P layer at 44.0º. The broad XRD diffraction peaks of the substrate in PZT and Fig. 4.2.a top panel also indicate a rhombohedral symmetry and a poly-domain situation, similar to the case reported by Frano et al. for epitaxial $LaNiO_3$ thin film layer.[21] The observation that also the PZT-P layer shows a broad diffraction peak suggest that also these layers have a rhombohedral, polydomain structure, as is predicted by the position of the end point of the $S_m^0(T)$ path in the phase diagram ending in the rhombohedral phase at room temperature.

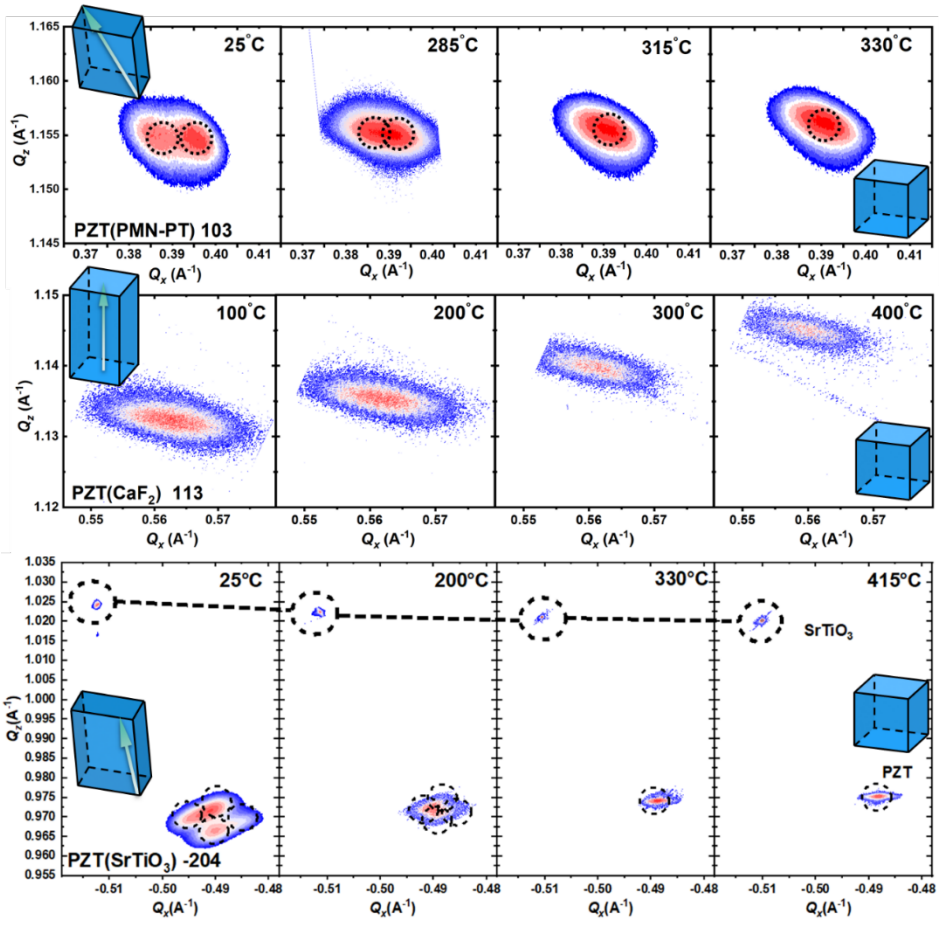

Figure 4.3. *Top panel: (103) RSMs of PZT-P at 25℃, 285℃, 315℃ and 330℃ elevated temperatures, respectively. The black dotted circles stand for the position of the fitted domain peaks. Two domain PZT domain peaks are visible at 25℃ in the first plot on the right, and two peaks move closer to each other at 285℃, then become single domain peak above 315℃. The middle panel: RSMs of the PZT-S (-204) reflection on STO substrate at 25℃, 200℃, 330℃ and 415℃ elevated temperatures, respectively. The black circles stand for domain peaks. Four PZT domain peaks are at 25℃ in the first plot on the right, four peaks move closer to each other at 200℃, then become a single domain peak above 330℃. The cash circle circles and lines indicate STO substrate diffraction peak at varies temperature. And the bottom panel is (113) RSMs of PZT-C at 100℃, 200℃, 300℃ and 400℃.*

PMN-PT single crystal is rhombohedral at room temperature and converts in the tetragonal phase at around 200℃, then becomes cubic at 250℃.[18, 20] The rhombohedral PZT is not directly imprinted from the rhombohedral PMN-PT substrate as in **Figure 4.3**. top panel. It is demonstrated that at 285℃, PZT still has a rhombohedral phase, whereas the PMN-PT substrate is cubic. It is therefore the rhombohedral is PZT intrinsic symmetry when the thermal misfit strain in PZT is 0.0025.

Figure 4.2.b and 4.2.c depict PFM results, where in a central square aera PZT is switched down by +7 V, whereas the surrounding square is poled up by a direct current (DC) bias of -7 V. The difference between the two phases is 180°. Surrounding nanoscale average domain size is around 130 nm. In the supporting materials, a AFM scan over the same area as showing in Figure 4.2.b and 4.2.c. The inserted surface roughness profile shows a height difference within 1nm in top surface topography. The hundred nanometres size of domains in Figure 4.2.a are PMN-PT substrate domains, which are easily distinguished from PZT domains regarding their respective domains sizes. Since the PZT is rhombohedral, an inevitable in-plane PFM signal was detected as shown in **Figure 4.2. b**.

RSMs of the PZT-P pseudocubic (103) at different temperatures were measured and plotted in the top row of panels of **Figure 4.3.**. It shows that the out-of-plane lattice component slightly decreases with increasing temperature (increasing Q_z), but secondly and more interestingly is that below about 300℃ a double peak is observed. The double peak (103) RSMs correspond to a mechanically relaxed PZT which would show 4-symmetry domain peaks in H-L plane[21]. However, due to the overlap in the projection plane, only two peaks can be seen. Above 300℃ there is a single diffraction as expected for a single domain tetragonal film. This corresponds with the strain-path for PZT-P in the model phase diagram. In the supplementary information the in-plane and out-of-plane lattice parameters and rhombohedral angles derived from RSMs of the PZT-P samples are shown as function of temperature in **Figure S4.1.** right panel.

The piezoelectric out-of-plane displacement-electric field hysteresis loops of PZT-P films, has been given in Figure 4.1. and **Figure 4.8.** Note that a series of tip

mechanical calibrations on a Periodically Poled Lithium Niobate (PPLN) standard sample with a known d_{33} value were used to quantify the PFM measurements. PZT-P shows a d_{33} is 81.9 pm/V which is lower than Vergeer's calculations.

The rhombohedral symmetry not only explains the appearance of an in-plane signal in the PFM scan in **Figure S4.2. b**, but also clarifies why the signal is relatively weak. The PZT rhombohedral angle α is smaller compared to the typical one for $BiFeO_3$, α only differs less than 0.5° from 90°. The small angle gives to small sub vector in-plane components and leading to barely observable in-plane domains information. The domain peaks have been converted into lattice parameters at various temperature and plotted in **Figure S4.1** right panel. The c/a ratio is 1.003 and the α is 89.95° at 415°C. All pervious measured results for PZT-P show agreements with the temperature v.s. thermal misfit phase diagram predicted in Figure 4.1.

4.2.2.2. PZT on CaF_2 substrate (PZT-C)

To further explore the effects of huge compressive thermal strain in PZT, CaF_2 substrate was chosen by its experimental CTE is 20.5×10^{-6} K^{-1}, which is slightly larger than the principle number mentioned previously. In **Figure 4.4. a** XRD confirms that the PZT on CaF_2 substrate (denoted as PZT-C) is well-ordered epitaxial film. The diffraction has been chosen since it is close to the (004) diffraction of the substrate, the bottom electrode $SrRuO_3$ cannot be seen in this scan range. A twinned crystal in CaF_2 substrate resulted in a splitting in its (004) diffraction peak. The PZT shows one single domain peak in Figure 4.3. middle panel at various temperatures, suggesting that the film is in a single domain state at all temperatures, excludes the influence of the twinned substrate. Figure 4.4. a phi-scan shows a 45° difference between CaF_2 (220) and PZT (110), hence a 45° cubic lattice in-plane lattice rotation can be deduced in **Figure 4.3. b**. From the Figure 4.3. d middle panel are temperature dependent RSMs of PZT-C the PZT 113 diffraction peaks indicate a tetragonal single domain symmetry. The lattice constants as described in **Figure 4.5.**, $\alpha = \beta = \gamma = 90°$ at all temperatures, and a = b = 4.046 Å and c = 4.148 Å at room temperature, giving the c/a ratio is 1.025 at room temperature. The c/a value decreased along the temperature arising, became to 1.006 at 400°C. The paraelectric-

ferroelectric phase transition temperature is therefore expected to be higher than for PZT-S and PZT-P.

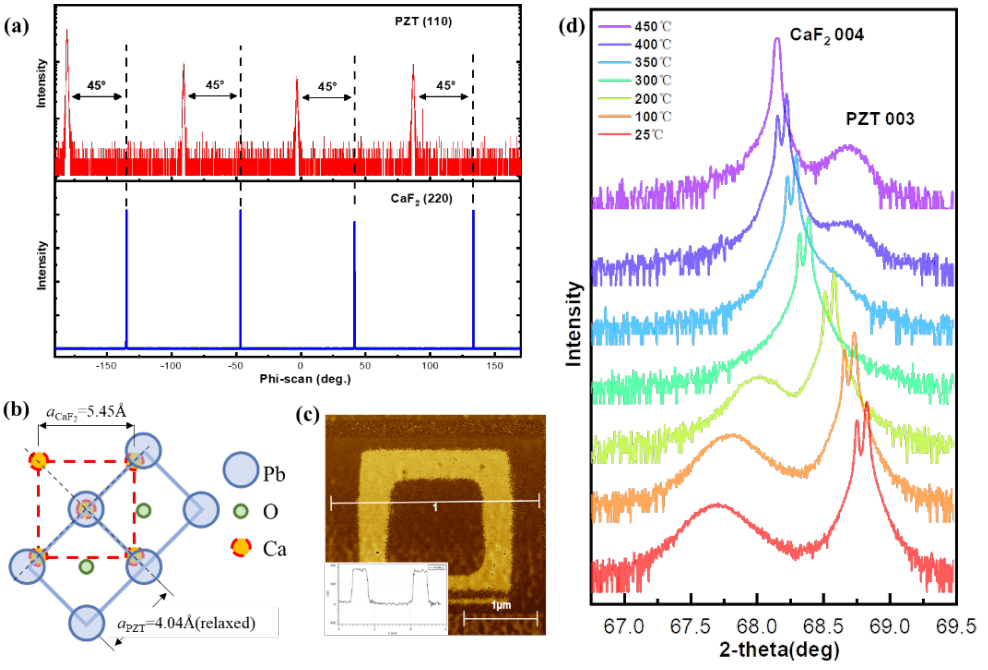

Figure 4.4. *(a) Phi-scan for (220) diffraction peak substrate CaF_2 and the (110) diffraction peak of PZT film, the difference between CaF_2 (220) and PZT (110) is 45°. (b) the schematic of PZT has a 45 ° in-plane rotation on CaF_2. (c) The XRD 2-theta 004 diffraction peak of CaF_2 and 003 diffraction peak of PZT, associate with the scans at varied temperatures.*

The PFM in **Figure 4.4. c** shows a single domain out-plane phase image. No in-plane domain information was measured indicates there is no a/b in-plane tetragonal domains. The d_{33} piezoelectric coefficient in PZT-C is presented in Figure 4.3. middle panel, the lowest value 32.4 pm/V among three samples is characterised.

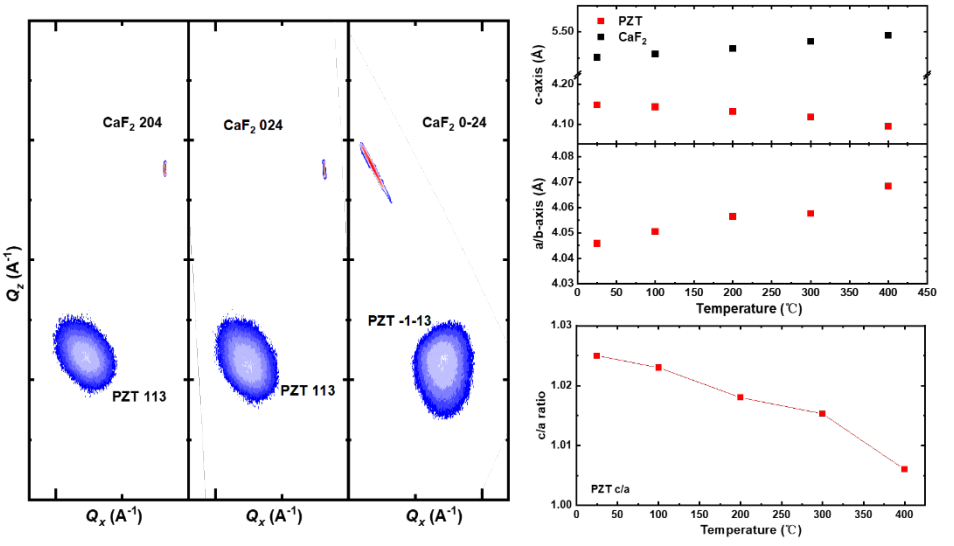

Figure 4.5. *CaF_2 (204), (024) and (0-24) RSMs of PZT-C in the right, middle and left panel, separately. PZT (113) single domain diffraction peak can also be seen at bottom of each panel. CaF_2 (113) RSMs at altered temperatures 100℃, 200℃, 300℃ and 400℃, respectively. Bottom right panel is the PZT-C out-plane(top) and in-plane(bottom) lattice constants abstracted from the RSMs. Bottom right is calculated c/a ratio, the value decreased against the temperature increased.*

4.2.2.3. PZT on $SrTiO_3$ substrate (PZT-S)

STO shows a CTE value between CaF_2 and PMN-PT, therefore an intermediate thermal misfit strain is expected in PZT film on STO substrate (denoted as PZT-S). In Figure 4.2. bottom panel XRD confirms that the PZT grown on the STO substrate is a well-ordered epitaxial film. The diffraction peak of the bottom electrode $SrRuO_3$ (002) peak with Laue fringes is observed around 46°. Compared to the PZT diffraction peak of PZT-P in Figure 4.2. top panel, PZT in PZT-S shows a much sharper diffraction peak at 2-theta of 43.91°. The topography in the **Figure 4.2.d** AFM image shows a peak-to-peak roughness of 1nm, demonstrating a very smooth surface. Contrary to PZT-P in Figure 4.3. top panel, where only two peaks are visible,

in PZT-S, all four closely spaced domain peaks are identical, although the peak intensities are not equal.

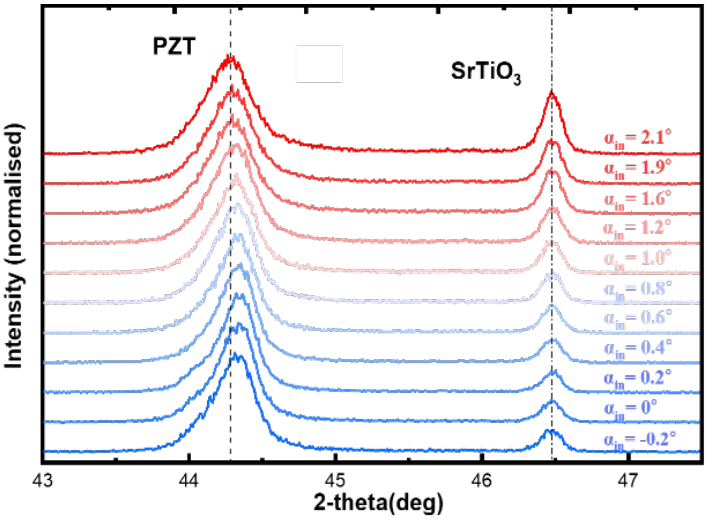

Figure 4.6. *Grazing incidence XRD patterns at (200) peaks of PZT and STO, dashed line indicates the 2q of PZT (200) when incident angle α_{in} is 2.1° and dashed dots line gives the diffraction peak positions of STO.*

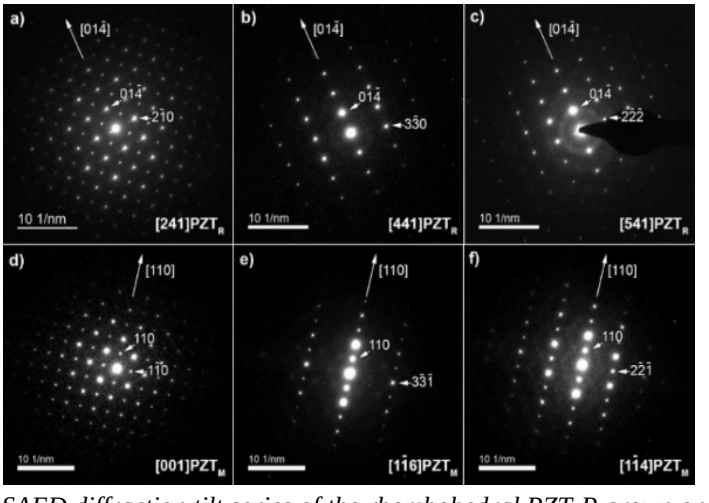

Figure 4.7. *SAED diffraction tilt series of the rhombohedral PZT-P grown on PMN-PT substrate.*

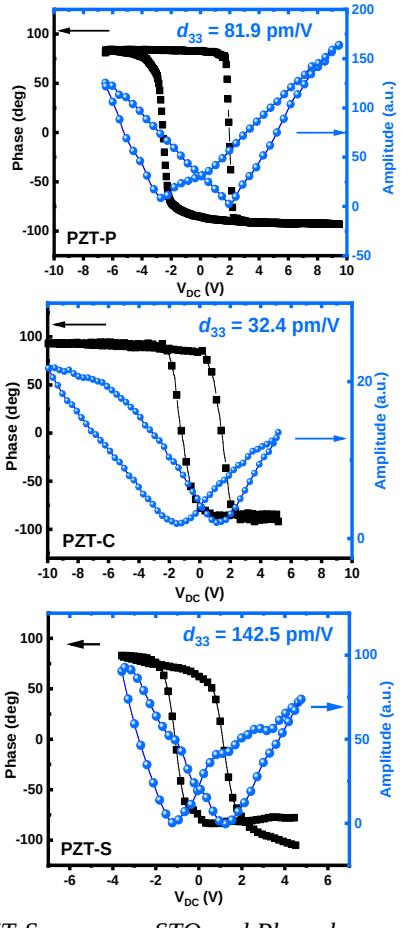

Figure 4.8. *Monoclinic PZT-S grown on STO and Phase loop and amplitude measured by PFM for PZT-P (right-top panel), PZT-S (right-middle panel) and PZT-C (right-bottom panel), respectively. The measured d_{33} value is inserted at the top right.*

Figure 4.3. bottom panel demonstrates an entirely different epitaxial strain level between substrate and deposited films at higher temperatures, in contrasts to the misfit strain at room temperature. The results are not conclusively showing a tetragonal c-phase at 330°C, α is deviating from 90°, nevertheless, a notable change is observed compared to room temperature, and it is clear that a single domain phase is achieved. For PZT-S at 415°C, a, b and c are all equal, and α is closer to 90°, but not exactly 90°. Near the phase boundaries, phenomenological calculations have

difficulty in dealing with the slight Gibbs free energy differences between the two symmetries, and this may lead to an uncertainty of the exact location of the phase boundary in the phase diagram.

In order to deepen our understanding of the relaxation of the strain in the PZT-S film as a function of the distance from the substrate-film interface, grazing incidence XRD (GI-XRD) was utilised for investigating the (200) in-plane diffraction peaks, see **Figure 4.6.**. With increasing the X-ray incident angle α_{in}, the beam penetrates deeper into the sample. For the STO substrate, the critical α angle is 0.23°. Note that the intensities of substrate peaks slightly rise with α increasing, suggests a higher contribution from the substrate. For α = 2.1°, the PZT diffraction peak is at 44.272°, and for α = 0°, the PZT diffraction peak is at 44.322°. This peak shift corresponds to an increase of the PZT in-plane lattice constant by about 0.004 Å, indicating slow stress relaxation over the thickness. The data will be discussed in the discussion section.

Figure 4.2. e and **f** depict PFM measurements for PZT-S. For the central solid square area -7 V was applied and for its surrounding square +7 V was applied. The phase difference between these two aeras is 180º. Outside the switched aera, the average diameter of the PZT domains is about 200 nm. No up or down oriented domains are observed as the majority in the phase channel image, neither 45º or 180º oriented domains are observed. The piezoelectric response is measured and shows in **Figure 4.8.** bottom panel, the PZT gives the highest d_{33} 142.5 pm/V among three PZT samples.

Thus far, this section has shown the PFM, XRD and piezoelectric response experimental data for PZT-P, PZT-C and PZT-S. PZT-P, PZT-C and PZT-S show their microstructures, symmetries, phase transition temperatures and properties are in agreement with the predicted phase diagram in Figure 4.1. We will discuss the connections behind these data in the followed section.

4.3. Discussion

The structural symmetry and properties are discussed in the following section.

Regarding the symmetry of PZT, For PZT-P, Figure 4.3. gives a series of asymmetric RSMs at 25℃, 285℃, 315℃ and 330℃, respectively. A typical rhombohedral symmetry (103) at room temperature as previously described, shows a α angle around 86.31°. At 285℃, two domain peaks are still visible, however, they start to merge into one peak. At both 315℃ and 330℃ only one single domain peak is seen. In this temperature range, the c/a ratio slightly decreases from 1.001 to 1.000, pointing to the fact that the thermal strain brings the PZT close to or at the phase boundary at cubic, tetragonal c and rhombohedral triple point.

In contrast, the situation for PZT-S is much more complicated compared to PZT-P. The four monoclinic polydomain peaks merges into one high intensity peak at 330℃, where α equals 89.61°, c = 4.1057Å and $a = b$ = 4.1055Å in bottom panel of Figure 4.3. At 415℃, c/a is was reduced to 1, α was increased to 89.88° as can be seen in the right panel of Figure S4.1.. Figure 4.3. bottem panel also shows the linear expansion of STO substrate with a decreasing Q_z value. More data details of PZT lattice constants can be found in **Figure S4.1.** right panel.

PZT-C has a single domain tetragonal symmetry at room temperature. A greater in-plane compressive thermal misfit strain forces the B site ions displacing further in c direction, gives rise a bigger c/a ratio in PZT-C as comparing with PZT-S and PZT-P. Single c-oriented domain also faces higher free energy barrier between the cubic phase and the tetragonal phase, resulting in the highest phase transition temperature among these three PZT samples.

Figure 4.3. bottom panel PZT-S [-204] asymmetric RSMs display a very interesting domain pattern, which is different from the PZT-P and PZT-C films. Based on the location of the four domain peaks, it can be interpreted as monoclinic c type (denoted as M_c), which is the polarisation orientation is landed in 100 plane, whereas $c > a$. **Figure 4.9.** shows the schematic stacks of PZT sample. The ω_{it} stands for the angle of M_c c-axis deviated from the normal of the substrate surface. As the PZT thickness increases, the plane of the M_c 110 plane is no longer parallel to the substrate surface due to the relaxation. The angle ω_{ot} stands for the tilting angle between PZT 001 plane and substrate 001 plane, give rises a disequilibrium four domain peaks in HL plane.

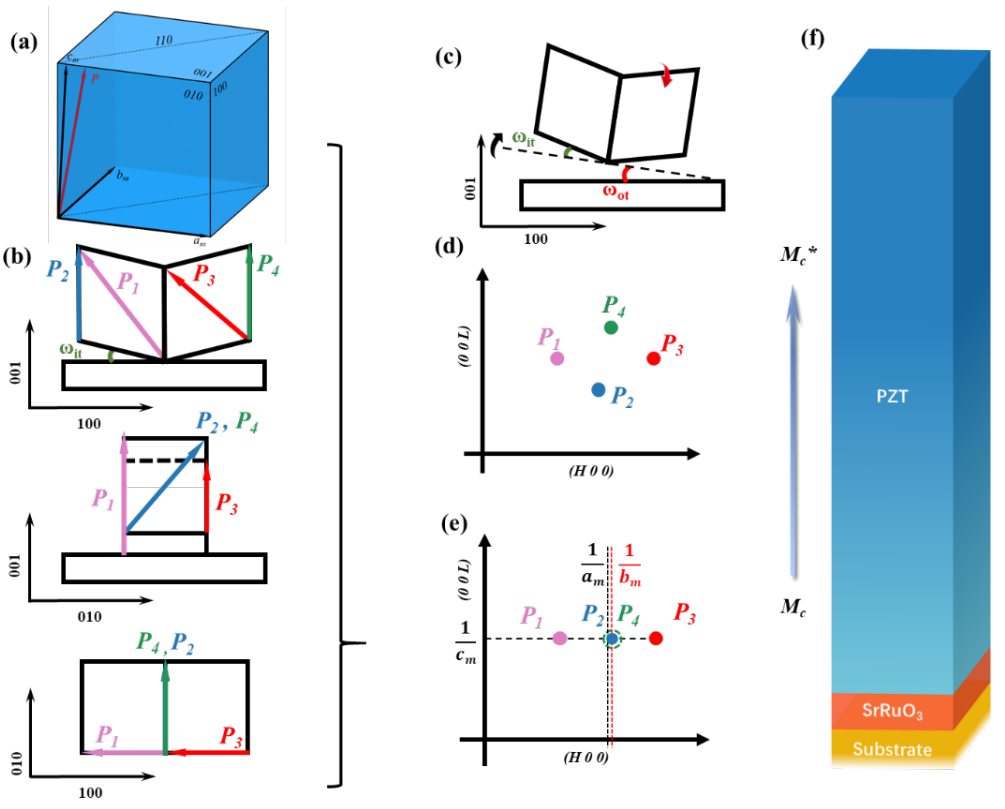

Figure 4.9. *Illustrations of M_c explaining the domain peak pattern and the possible observed intensity variations. (a) The schematic M_c in cubic mode, shows the polarisation as red arrow P and labels the sub-vector in [100] as a_m, the sub-vector in [010] direction is b_m and the sub-vector along [001] monoclinic lattice unit cell is c_m; (b) Four possible real space lattice vectors for monoclinic c-type are labelled as P_1, P_2, P_3 and P_4, separately. The ω_{it} stands for the angle of M_c c-axis deviates from the normal of the substrate surface. All lattice vectors are given in front-view (top), side-view (middle) and top-view (bottom); (f) shows a gradually relaxation with PZT, the lattice close to PZT/SRO interface is labelled as M_c and the lattice away from the PZT/SRO interface is labelled as M_c*; (e) shows the expected RSM of M_c. $1/a_m$ (black dots line) is the middle value for P_1 and P_3 in [H00], and $1/b_m$ (red dots line) is the [H00] value for P_2 and P_4. P_2 is out and above (H0L) plane, labelled with solid blue dot. P_4 is below (H0L) plane, labelled by a green dash circle. $1/c_m$ is the projection value in [00L] direction for P_1, P_2, P_3 and P_4; (d) is experimentally RSM for PZT-S in (204), can be achieved by a tilting of the angle ω_{ot} as showing in (c).*

For the piezoelectric behaviour, Figure 4.1. bottom panel also represents the calculated piezoelectric response d_{33} versus the level of thermal misfit strain of the substrate. The red solid line shows the profile of d_{33} for PZT (x = 0.6), with a steep enhancement of the piezoelectric coefficient around 140 pm/V at the $\mathbf{S}_m$ value marked by the light blue line in Figure 4.1. right panel. Different from bulk ceramic, sol-gel and single crystal PZT (x = 0.6), this extraordinary high d_{33} has not been reported for this thin film thickness range before. On the other hand, PZT (x = 0.6) d_{33} is around 110 pm/V at the $\mathbf{S}_m$ marked by the orange arrow, which in this case denotes the thermal misfit strain between the PZT and PMN-PT. The calculated d_{33} value of PZT-P is in agreement with previous studies[22] [23].

There are a number of similarities between the PZT (x = 0.52) bulk ceramic and the PZT-S (x = 0.6) thin film. First, the monoclinic phase has first been reported for the low temperature side PZT(x = 0.52) phase boundary on the low temperature side[6], and both compositions the monoclinic phase is c type. The monoclinic symmetry has been very well classified and studied in the many other ferroelectric materials[24, 25]. For instance, with the aid of epitaxial strain engineering, $BiFeO_3$ thin films were reported to be M_B phase on a $PrScO_3$ substrate under a tensile strain[26], and M_c and M_A phases coexists on $LaSrAlO_4$ substrate under a compressive strain[27]. In another report, a 400nm $BiFeO_3$ film showed a notable rotation of the intrinsic spontaneous polarisation (P_s) from the M_A to the M_B phase induced by in-plain strain[28]. In addition, a $BiFeO_3$ phase transition was observed from the lower-temperature M_c phase to a tetragonal phase at higher-temperature via a M_A phase[29]. In should be noted here that several researchers refer to the distorted monoclinic as a triclinic phase[30, 31] [31] or simplified it to a distorted rhombohedral symmetry[32] [33]. In this work, the monoclinic PZT is in-plane partially relaxed from the thermal misfit strain and shows shear distortions[34] and could be regarded as an intermediate phase towards to a rhombohedral phase for thicker films. Strong PZT lattice rotation and tilting in the entire film, associated with tilted twin domain walls, lead to a four-fold symmetric poly domain peak, which differs from thinner M_c films. **Figure 4.6.** the GI-XRD illustrates the slight in-plane relaxation of the PZT near the top of the layer versus the PZT near the bottom interface. The figure also proves the transition from M_c towards the rhombohedral phase, which can give rise to an in-plane lattice constant which is decreased at the PZT film top surface. These

distortions are a consequence of the thermal misfit strain of STO substrate, in comparison to the PZT-P and other rhombohedral symmetry observed in PZT films[35]. In addition, one interesting assumption is that a monoclinic A-type phase may exist between the M_c and rhombohedral phase, due to lower Gibbs free energy and similar polarisation orientation, which demands for a further investigation.

One criticism of the previous interpretation of the XRD analysis on the PZT-S sample in terms of the monoclinic phase is that XRD gives the average information over the whole film, so that impurity phases may contribute[6, 36]. We therefore decided to perform transmission electron microscopy imaging (TEM) in bright field (BF) and dark field (DF) modes as well as selected area diffraction (SEAD) and convergent beam electron diffraction (CBED) to investigate the symmetry differences between the specimen grown on STO (PZT-S) and the one grown on PMN-PT (PZT-P). Furthermore, scanning transmission electron microscopy energy dispersive x-ray spectroscopy (STEM-EDX) was performed to rule-out composition difference to be the source of the difference in physical properties observed between the two films.

High similarities are observed in both Bright Field (BF) images of PZT-S and PZT-P, taken along the [110] direction, as seen on **Figure S4.4 a** and **c** respectively. For both samples, a columnar structure is observed with column widths between 50 and 100nm. Dark Field (DF) using the (1-11) reflection, as displayed on panels **b** and **d** of **Figure 4.7.**, reveals similar domain structure for both films. FiguresS4.4**e** and f show respectively an overlap of a selected area diffraction patterns taking from a 50 nm monodomain region of PZT-S (blue) and from the PZT-P (orange). Diffraction patterns were taken along the [100] and [110] zone axis respectively. Comparison of diffraction patterns shows almost no differences between the two films. Furthermore, as shown in panel Figure S4.5.-S4.6., no major chemical composition difference is seen between the two films as shown by overlapping the EDX spectra of both films. The signals from Cu and Mo are a typical artefact usually observed due to the FIB grid and a spacer, which are made of copper and molybdenum respectively.

To gain insight on the crystal structure of PZT-S and PZT-P, a more detailed diffraction analysis was performed. Since the main difference between the monoclinic PZT(x=0.52) phase and the rhombohedral PZT(x=0.60) phase is the symmetry of the unit cell, a tilt series of SAED patterns were acquired. Diffraction patterns were taken from the same grain of the film by careful tracking its positions during the sample rotation. For each diffraction pattern, the experimental angles of a double tilt holder were recorded, which later were compared those calculated for two PZT phases. Calculation of the angles between the zone axis was performed using the ALPHABETA software[37]. **Figure S4.4. (a-c)** shows a series of diffraction patterns for varying tilt angles, when rotating around the [01-4] direction of PZT-S film. A comparison of experimental and calculated angles between the zone axis showed good agreement for the rhombohedral structure (**Table S4.1.**). However, due to the symmetry of the rhombohedral unit cell, there are several possible (crystallographically equivalent) solutions to index the diffraction patterns, but they are all confirming the rhombohedral structure (a list of other zone axis can be found in Supplementary Materials). Similar procedure was applied for the diffraction patterns of PZT-S that rotated around the [110] direction (Figure. 4.6. d-f). A good agreement was found for the monoclinic structure (**Table S4.2.**).

Second, both monoclinic phases in PZT-S and PZT(x=0.52) exist at the rhombohedral and tetragonal phase boundary, which is also as known as the morphotropic phase boundary. These monoclinic low symmetry phases mentioned previously of $BiFeO_3$, are interpreted as a structural transition between rhombohedral and tetragonal, and contribute to an enhanced piezoelectric response due to the ease of polarisation rotation[38][39]. In Vergeer's calculations, the d_{33} profile for PZT (x = 0.6) in Figure 4.1. have also demonstrated how this low symmetry can result into the enhanced piezoelectric property. Here one has realised that for these simulations only single domain piezoelectric response was considered. That is why PFM is the best approach of verifying the d_{33} expectations, since the probe tip radius size is only 25 nm, far smaller than one single domain of the PZT. It was already noted that PZT-S satisfies the expectations while PZT-C and PZT-P shows a much lower d_{33} value. One possible explanation is the PZT film was still clamped by the substrate, the substrate intends to restore the unit cell distortion and compensate the polarised interface between the film and substrate.

In this work, the monoclinic c-type observed for PZT(x = 0.6) is quite different from the monoclinic phase known from the temperature-composition phase diagram.[15] To be really sure, it would be necessary to verify the Zr/Ti composition ratio in the deposited film. **Figure 4.3.** describes a RBS measurement, confirming the Zr/Ti composition ratio in the film to be 60/40.

4.4. Conclusion

In conclusion, we have looked into the thermal misfit strain effect of PZT (x=0.6) thin films using different CTE substrates. Using PLD deposition at high temperature, PZT-C, PZT-S and PZT-P samples were prepared then characterised by AFM and XRD, showing a crystalline and phase pure structure. The different symmetries observed in the RSMs of these three samples, taken at room temperature, give a clear picture of the major role of thermal misfit strain in the resulting phases that can occur in clamped thin films. Moreover, the phase transitions seen as a function of temperature also matched the theoretical predictions obtained from calculations. These important discoveries are crucial to materials developments and film devices design toward a fundamental understanding, which is that in epitaxial films grown by PLD, not only the mechanical clamping strain effects should be considered, but also the thermal strain.

4.5. Experimental Section

The experiments of PZT and $SrRuO_3$ films were carried out on CaF_2, $SrTiO_3$ and PMN-PT substrates by pulsed laser deposition (PLD). 0.1° miscut $SrTiO_3$ substrate from CrysTec GmbH were etched by the buffered HF, left single TiO_2 termination with well-defined terrace features. The PMN-PT substrates were from SurfaceNet GmbH with typical surface features of 10-20 nm height differences caused by its domains structures. The films were deposited at 600°C, under a pressure of 0.13mbar oxygen pressure. A pulsed KrF excimer laser with a 248nm wavelength was focused on at $SrRuO_3$ and PZT polycrystalline ceramic targets at a repetition rate of 4 Hz and 10 Hz, respectively. The fluences of laser measured on the targets was 2.5 J/mm^2. The crystallisation of the films was checked by θ-2θ scan, obtained by a Panalytical X'pert MRD lab system. Asymmetry RSMs were both taken by Panalytical X'pert

MRD with an Aton Paar DHS 900 module and Rigaku Smartlab 9 kW, individually. The AFM and PFM were conducted by a Bruker Icon atom force microscope using a Cr/Pt conductive coating. Square substrate of periodically-poled lithium niobite (PPLN) from Bruker is used as a standard PFM sample for calibration purposes.

Supporting Information

the following expression is derived

$$S_m^0(T) \equiv \left(\frac{a_s^* - a_0}{a_0}\right)_T \approx \big(\alpha_f - \alpha_s(T)\big)(T_d - T) + Q^* P_S^2(T)$$

$S_m^0(T)$ is defined as the strain of a film with an equivalent cubic lattice parameter a_0 (which can be read as the lattice parameter at temperature T without paraelectric-ferroelectric phase transition) on a substrate with effective lattice parameter a_s^* at temperature T. α_f and $\alpha_s(T)$ are the constant, respectively temperature dependent CTE's of film and substrate. T_d is the deposition temperature (in our experiments 600 °C). The additional term $Q^* P_S^2(T)$ arises from the volume increase of the unit cell (and thus the pseudocubic lattice parameter) when going over from the paraelectric to the ferroelectric phase. The effective electrostriction constant $Q^* \approx (Q_{11} + 2Q_{12})/3 = 0.0011$ for PZT (x = 0.6). This term is temperature dependent through its dependence on the polarization and is here approximated by the LDG-approximation, $P_S^2(T) \approx P_S^2(0)(1 - T/T_C)$, with T_C the Curie temperature of the film [note in ref. Strictly speaking $P_S^2(0)$ and T_C also depend on the strain in the film, but the changes are small and can be neglected for the present calculations.]

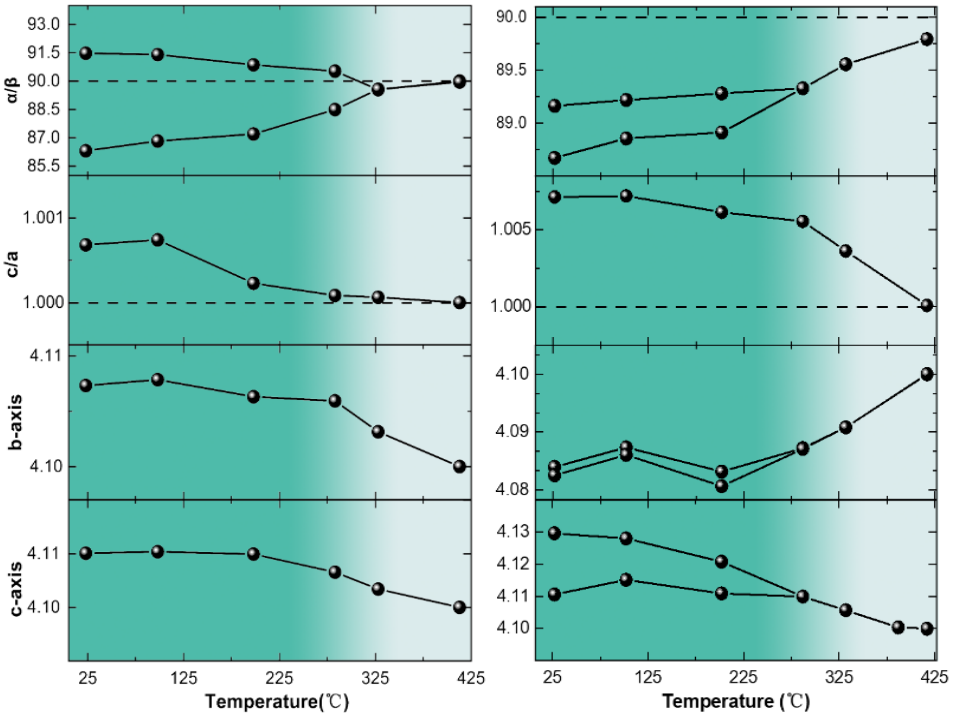

Figure S4.1. *Lattice parameters of PZT-P at varies temperature. The α is PZT lattice angle between c axis (110) plane, the β is also between c and (001), but 90° differs from α in the (001) plane. α and β are not equal. The α and β started to equal above 300℃ and only one domain has been left. c/a ratio is not 1 until 400℃. PZT-S lattice constants at varied temperatures. The α is PZT lattice angle between c axis (110) plane, the β is also between c and (001), but 90° differs from α in the (001) plane. α and β are not equal demonstrates an asymmetry relaxation along the polarisation direction in (110) plane. The α and β started to equal above 300℃ and only one domain has been left. c/a ratio is not 1 until 400℃. The topographic and in-plane PFM phase image of PZT-P.*

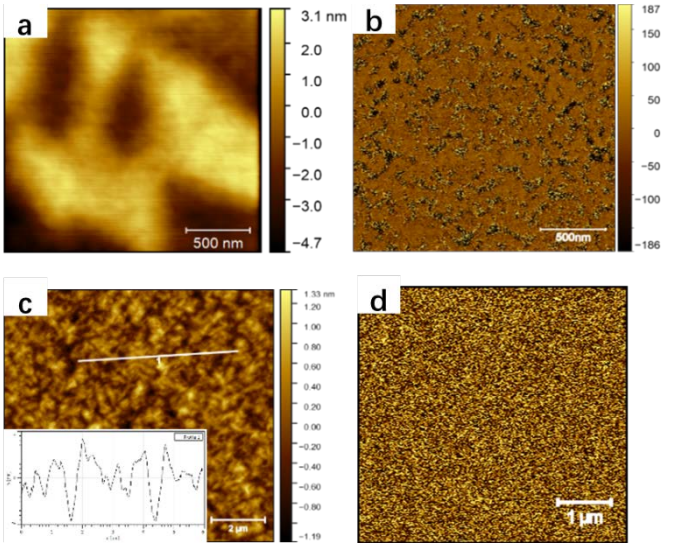

Figure S4.2. *(a) The dark and highlighted domains in micrometres scale are attributed by the PMN-PT substrate. The PZT in-plane nano domains is scanned with 500 mV DC in (b), darken regions are corresponded with out-plane domains, indicating the PFM in-plane signals were generated from a ferroelectric domain, that the domain contains two sub polarisation vectors. The topographic and in-plane PFM phase image of PZT-S. (a) The inserted profile is the PZT-S surface roughness. The PZT in-plane nano domains is scanned with 500 mV DC, there was only noise detected for PFM in-plane scan in (b).*

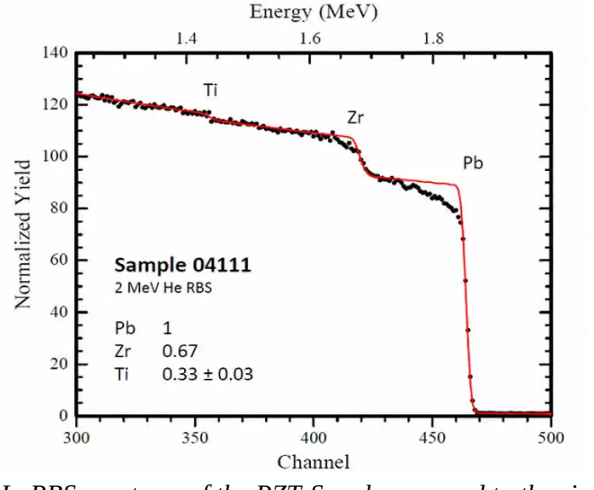

Figure S4.3*. MeV He-RBS spectrum of the PZT-S and compared to the simulation. The composition ratio among lead, Zr and Ti were labelled in the plot. The noted Zr : Ti =*

0.67 : 0.33 which was fitted the expected composition from the deposition process.

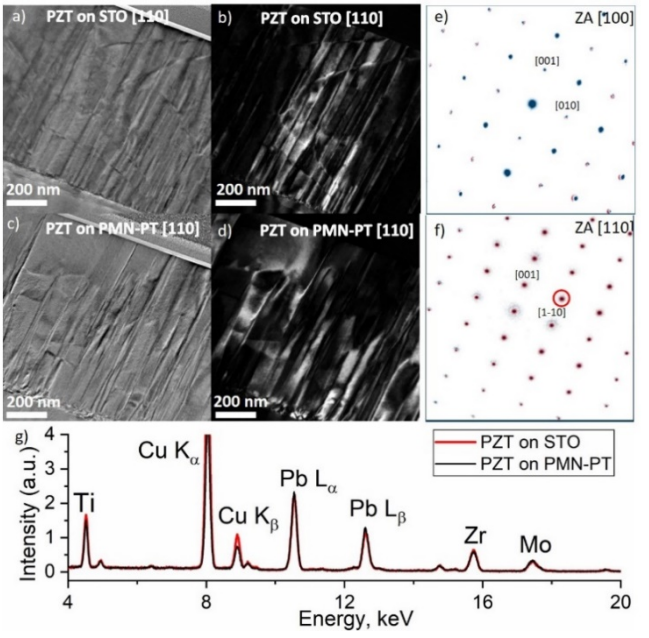

Figure S4.4. *TEM images of the full film grown on STO and on PMN-PT, a) and c) are BF-TEM of a lamella of the sample showing similar contrast for the two specimens. b) and d) are Dark Field (DF-TEM) images using the (1-11) reflection showing similar domain structure and columnar growth for both films. Panels e) and f) are overlay of an SAED pattern of the PZT-S in blue and PZT-P in orange taken in both the [100] and the [110] zone axis showing almost no differences between the two films. g) EDX spectra of the two films showing a similar average composition in cations.*

SAED Phase identification

As was mentioned in the main text of the paper, a careful calculation of the angle between each two-zone axis was performed using the ALPHABETA software [1]. This software allows to calculated the angle based on the alpha and beta tilt of the double-tilt holder. The results of experimental angles are given in the Table S1 and S2 for films grown on STO and PMN-PT substrates. As can be seen from the data, a good agreement was found for several solutions of the rhombohedral PZT structure and one solution for the monoclinic PZT structure. All six solutions of rhombohedral

structure are crystallography equivalent. A slight discrepancy between the experimental and calculated angles can be explained by the imperfection of the double-tilt holder and possible distortions of the crystal.

Experiment		
ZA 1	ZA 2	23.48
ZA 2	ZA 3	11.05
ZA 1	ZA 3	34.44

Solution 1		
[2, 4, 1]	[4, 4, 1]	25.16
[4, 4, 1]	[5, 4, 1]	10.01
[2, 4, 1]	[5, 4, 1]	35.17

Solution 2		
[2, 4, 1]	[0, 4, 1]	25.16
[0, 4, 1]	[-1, 4, 1]	10.01
[2, 4, 1]	[-1, 4, 1]	35.17

Solution 3		
[-4, -2, 1]	[-4, -4, 1]	25.16
[-4, -4, 1]	[-4, -5, 1]	10.01
[-4, -2, 1]	[-4, -5, 1]	35.17

Solution 4		
[-4, -2, 1]	[-4, 0, 1]	25.16
[-4, 0, 1]	[-4, 1, 1]	10.01
[-4, -2, 1]	[-4, 1, 1]	35.17

Solution 5		
[2, -2, 1]	[4, 0, 1]	25.16
[4, 0, 1]	[5, 1, 1]	10.01
[2, -2, 1]	[5, 1, 1]	35.17

Solution 6		
[2, -2, 1]	[0, -4, 1]	25.16
[0, -4, 1]	[-1, -5, 1]	10.01
[2, -2, 1]	[-1, -5, 1]	35.17

Table S4.1. *Comparison of experimental and calculated angles between the zone axis of*

diffraction tilt series shown in fig. 4.7. a-c of the main text.

Experiment		
ZA 1	ZA 2	17.2
ZA 2	ZA 3	8.05
ZA 1	ZA 3	25.25

Solution 1		
[0, 0, 1]	[1, -1, 6]	18.05
[1, -1, 6]	[1, -1, 4]	8.02
[0, 0, 1]	[1, -1, 4]	26.07

Table S4.2. *Comparison of experimental and calculated angles between the zone axis of diffraction tilt series shown in fig. 4.7. d-f of the main text.*

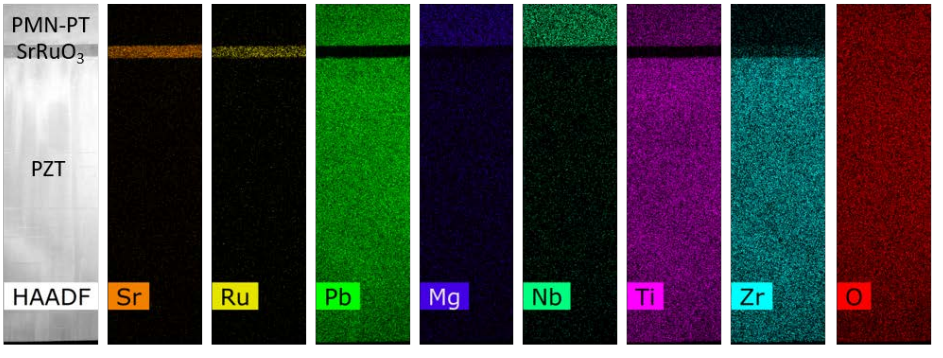

Element/Measure	Zr, atom%	Ti, atom%
1	71.83	28.17
2	71.42	28.58
3	71.40	28.60

Figure S4.5. *EDX analysis of the sample on PMN-PT*

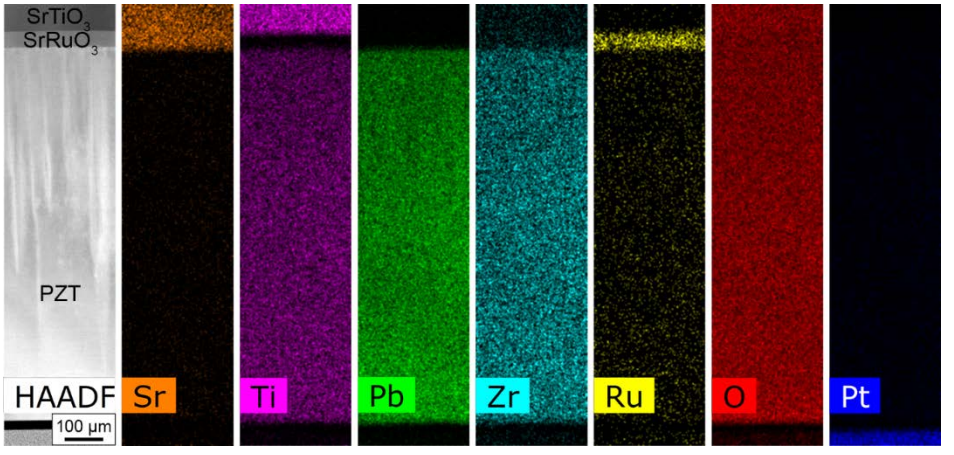

Element/Measure	Zr, atom%	Ti, atom%
1	70.54	29.46
2	71.63	28.37

Figure S4.6. *EDX analysis of the sample on STO*

References:

1. Jaffe, B., W. Cook, and H. Jaffe, *Piezoelectric ceramics, 101 London*. 1971, Academic Press.
2. Fu, H. and R.E. Cohen, *Polarization rotation mechanism for ultrahigh electromechanical response in single-crystal piezoelectrics.* Nature, 2000. **403**(6767): p. 281-283.
3. Noheda, B., et al., *A monoclinic ferroelectric phase in the Pb (Zr 1− x Ti x) O 3 solid solution.* Applied physics letters, 1999. **74**(14): p. 2059-2061.
4. Xu, F., et al., *Domain wall motion and its contribution to the dielectric and piezoelectric properties of lead zirconate titanate films.* Journal of Applied Physics, 2001. **89**(2): p. 1336-1348.
5. Zhang, N., et al., *The missing boundary in the phase diagram of PbZr 1− x Ti x O 3.* Nature communications, 2014. **5**: p. 5231.
6. Noheda, B., et al., *Stability of the monoclinic phase in the ferroelectric perovskite PbZr 1− x Ti x O 3.* Physical Review B, 2000. **63**(1): p. 014103.
7. Noheda, B., et al., *Tetragonal-to-monoclinic phase transition in a ferroelectric perovskite: The structure of PbZr 0.52 Ti 0.48 O 3.* Physical Review B, 2000. **61**(13): p. 8687.
8. Houwman, E., et al., *Modelling functional properties of ferroelectric oxide thin films with a three-domain structure.* arXiv preprint arXiv:1901.10883, 2019.
9. Bartasyte, A., et al., *Stability of the polydomain state in epitaxial ferroelectric PbTiO 3 films.* Applied Physics Letters, 2008. **93**(24): p. 242907.
10. Koukhar, V., N. Pertsev, and R. Waser, *Thermodynamic theory of epitaxial ferroelectric thin films with dense domain structures.* Physical Review B, 2001. **64**(21): p. 214103.
11. Kukhar, V., et al., *Polarization states of polydomain epitaxial Pb (Zr 1− x Ti x) O 3 thin films and their dielectric properties.* Physical Review B, 2006. **73**(21): p. 214103.
12. Vergeer, K., *Structure and functional properties of epitaxial PBZRxTI1-xO3 films.* 2017.
13. Schlom, D.G., et al., *Strain tuning of ferroelectric thin films.* Annu. Rev.

Mater. Res., 2007. **37**: p. 589-626.

14. Nguyen, M.D., et al., *Misfit strain dependence of ferroelectric and piezoelectric properties of clamped (001) epitaxial Pb (Zr0. 52, Ti0. 48) O3 thin films.* Applied physics letters, 2011. **99**(25): p. 252904.
15. Corker, D., et al., *A neutron diffraction investigation into the rhombohedral phases of the perovskite series.* Journal of Physics: Condensed Matter, 1998. **10**(28): p. 6251.
16. de Ligny, D. and P. Richet, *High-temperature heat capacity and thermal expansion of SrTiO 3 and SrZrO 3 perovskites.* Physical Review B, 1996. **53**(6): p. 3013.
17. Arndt, H. and G. Schmidt, *Thermal expansion in relaxor ferroelectrics.* Ferroelectrics, 1988. **79**(1): p. 149-152.
18. Wongmaneerung, R., et al., *Thermal expansion properties of PMN–PT ceramics.* Journal of Alloys and Compounds, 2008. **461**(1-2): p. 565-569.
19. Noheda, B., et al., *Phase diagram of the ferroelectric relaxor (1− x) PbMg 1/3 Nb 2/3 O 3− x PbTiO 3.* Physical Review B, 2002. **66**(5): p. 054104.
20. Bai, F., et al., *X-ray and neutron diffraction investigations of the structural phase transformation sequence under electric field in 0.7 Pb (Mg 1/ 3 Nb 2/ 3)-0.3 PbTiO 3 crystal.* Journal of Applied Physics, 2004. **96**(3): p. 1620-1627.
21. Frano, A., et al., *Layer selective control of the lattice structure in oxide superlattices.* Advanced Materials, 2014. **26**(2): p. 258-262.
22. Wang, Y., et al., *Epitaxial ferroelectric Pb (Zr, Ti) O 3 thin films on Si using SrTiO 3 template layers.* Applied Physics Letters, 2002. **80**(1): p. 97-99.
23. Lian, L. and N.R. Sottos, *Effects of thickness on the piezoelectric and dielectric properties of lead zirconate titanate thin films.* Journal of Applied Physics, 2000. **87**(8): p. 3941-3949.
24. Janolin, P.-E., *Strain on ferroelectric thin films.* Journal of materials science, 2009. **44**(19): p. 5025-5048.
25. Vanderbilt, D. and M.H. Cohen, *Monoclinic and triclinic phases in higher-order Devonshire theory.* Physical Review B, 2001. **63**(9): p. 094108.
26. Chen, Z., et al., *Large tensile-strain-induced monoclinic M B phase in BiFeO 3 epitaxial thin films on a PrScO 3 substrate.* Physical Review B, 2013. **88**(5): p. 054114.
27. Chen, Z., et al., *Low symmetry monoclinic Mc phase in epitaxial BiFeO 3*

thin films on LaSrAlO 4 substrates. Applied Physics Letters, 2010. **97**(24): p. 242903.

28. Jang, H., et al., *Strain-induced polarization rotation in epitaxial (001) BiFeO 3 thin films.* Physical review letters, 2008. **101**(10): p. 107602.
29. Beekman, C., et al., *Phase transitions, phase coexistence, and piezoelectric switching behavior in highly strained BiFeO3 films.* Advanced Materials, 2013. **25**(39): p. 5561-5567.
30. Yan, L., et al., *Triclinic phase in tilted (001) oriented BiFeO 3 epitaxial thin films.* Applied Physics Letters, 2009. **94**(13): p. 132901.
31. Chen, Z., et al., *Coexistence of ferroelectric triclinic phases in highly strained BiFeO 3 films.* Physical Review B, 2011. **84**(9): p. 094116.
32. Folkman, C.M., S.-H. Baek, and C.-B. Eom, *Twin wall distortions through structural investigation of epitaxial BiFeO 3 thin films.* Journal of Materials Research, 2011. **26**(22): p. 2844-2853.
33. Zhang, S., et al., *Electric-field control of nonvolatile magnetization in Co 40 Fe 40 B 20/Pb (Mg 1/3 Nb 2/3) 0.7 Ti 0.3 O 3 structure at room temperature.* Physical review letters, 2012. **108**(13): p. 137203.
34. Kan, D. and I. Takeuchi, *Effect of substrate orientation on lattice relaxation of epitaxial BiFeO 3 thin films.* Journal of Applied Physics, 2010. **108**(1): p. 014104.
35. Schmitt, L.A., et al., *Composition dependence of the domain configuration and size in Pb (Zr 1− x Ti x) O 3 ceramics.* Journal of applied physics, 2007. **101**(7): p. 074107.
36. Wei, X.-K., et al., *Néel-like domain walls in ferroelectric Pb (Zr, Ti) O 3 single crystals.* Nature communications, 2016. **7**: p. 12385.
37. Cautaerts, N., R. Delville, and D. Schryvers, *ALPHABETA: a dedicated open-source tool for calculating TEM stage tilt angles.* Journal of microscopy, 2019. **273**(3): p. 189-198.
38. Du, X.-h., et al., *Crystal orientation dependence of piezoelectric properties of lead zirconate titanate near the morphotropic phase boundary.* Applied physics letters, 1998. **72**(19): p. 2421-2423.
39. Nagata, H., et al., *Large piezoelectric constant and high Curie temperature of lead-free piezoelectric ceramic ternary system based on bismuth sodium titanate-bismuth potassium titanate-barium titanate near the morphotropic*

phase boundary. Japanese journal of applied physics, 2003. **42**(12R): p. 7401.

Chapter 5 Reversible polarisation switching in leaky ferroelectrics through "Cut and Stick" ionic gel induced electrostatic field effect

In this chapter, a transparent and free-standing ionic gel as the dielectric layer for polarisation switching in leaky ferroelectric thin films is reported. While typically ionic liquids are used in electrical field gating experiments to probe fundamental properties of materials, here it is used to circumvent electronic transport through the leaky ferroelectric thin films. The association of an electrical double layer (EDL) with depolarisation at the solid-liquid interface contributes to the successful reversible switching in $PbZr_xTi_{1-x}O_3$ (PZT). For mechanical stability reasons, we used an ionic gel instead of a liquid. Using such ionic gels, the anisotropic ferroelastic switching from mono c-domain towards a-domain is studied in PZT grown on CaF_2 substrates. Our results demonstrate that an electrostatic field, induced by the free-standing ionic gel is an effective and promising way to investigate leaky ferroelectrics.

5.1. Introduction

Perovskite ferroelectric thin films, such as PZT, have drawn a lot attention in both research with focus on the physics as well as applications due to their spontaneous polarisations, which can be reversed switched by external fields, such as an electrical field, optical fields, or mechanical strain and so forth.[1-10] The fundamental understanding of both the polarisation switching process and the functional control mechanisms for switching are the main topics when investigating ferroelectrics devices.[11, 12] Switching by an electrical field is mainly used in these investigations, and one of the primary obstacles is the potential electrical conductivity that can occur in ferroelectric thin films caused by structural defects such as vacancies. This has significantly hampered the investigation of ultra-thin ferroelectric films or high voltage transistors.[13, 14] Contrary to the electric field effect, one can use an ionic liquid as the gated dielectrics for the electrostatic field modulation, and obtain a charge accumulation or depletion layer at the interface of the functional thin films.[15-18] The merits of this method include effective electron confinements, high ionic conductivity and excellent electrochemical stability.[19]

Lately, the successes in electrostatic modulation of correlated electron behaviours in “iontronics” was used to study gated high capacitance ferroelectric transistors.[20-23] Here we have studied this methodology to switch ferroelectric thin films.

In order to attach the electrolyte layer on PZT surface during a vertical alignment in XRD, in this work, an ionic gel (IG) was made. It contains a three-dimensional organic network, immersed with an ionic liquid matrix.[24-26] When a gating voltage is applied, over the IG, the cations and the anions are separated, mobilised, and charge accumulates at the surface of the gate electrode and the surface of the ferroelectrics.[27] While an electric double layer (EDL) is formed inside the IG to screen the charges at those interfaces, the polarisation can be switched in the ferroelectric film to compensate for the surface charges.[28] The IG with pre-deposited metal electrodes can be cut into a suitable size and placed on the ferroelectric thin films surface to form a device.[29] In this way, a large area of the ferroelectric layer can be reversibly and uniformly switched. The top surface of the ferroelectric film can also be studied after switching and upon removal of the IG without any etching damage. As a side note, the IG shares the benefits of an ionic liquid, and also shows the unique tensile strength as a free-standing polymer film. These advantages make IG gated ferroelectric transistor suitable for a comprehensive study of ferroelectric switching in leaky capacitors.

In this work, we successfully demonstrated the fabrication of a transparent free-standing IG, composed of poly(vinylidene fluoride-*co*-hexafluoropropylene) (P(VDF-HFP)) and 1-ethyl-3-methylimidazolium bis(trifluoromethylsulfonyl)imide ([EMI][TFSI]) on a Si wafer substrate with sputtered gold electrodes. The IG was subsequently cut and laminated on a pulsed laser deposited PZT thin film and used for reversible polarisation switching experiments. Finally, the gel was peeled off from the PZT surface enabling the study of ferroelectric domains by piezoelectric force microscopy (PFM). The PFM results showed remarkable contrast among regions of pristine nano-scale ferroelectric domains, switched up-ward domains and reversibly switched down-ward domains in one scan image. In a separate experiment, the IG gated capacitor resistance was tested at high voltage and ferroelectric switching dynamics were studied. In order to achieve this, an IG covered tetragonal

monodomain PZT thin film was poled up to 20V and measured *in-situ* using X-ray diffraction (XRD) and reciprocal space mapping (RSM).

5.2. Experimental methods

P(VDF-HFP) (CAS: 9011-17-0) average molecular weight 400,000 and [EMI][TFSI] (CAS: 174899-82-2) purchased from Merck are both mixed in acetone solvent with weight ratio in 1:4:7, respectively. The solution was stirred at 50℃ for 1h to achieve a proper viscosity for spin coating and vacuumed for 1h in order to remove air bubbles. An 8-inch radius Si wafer was used as a substrate. 4000 rpm for spinning was employed to acquire a uniform gel thickness, which thickness of the gel was then measured by atomic force microscopy (AFM). The gel was placed into a DC sputter deposition tool to create 400 nm thick patterned gold electrodes. Afterwards the gel was placed in a vacuum oven at 60℃ for 24h to remove residual solvent and absorbed water. After fabrication, the gel was stored in the atmospheric pressure oven at 80℃, in order to prevent absorption of water from the air.

The poly-domain monoclinic PZT and single-domain tetragonal PZT samples used in this chapter were made as described in Chapter 4. The gel was cut and placed on the PZT surface; the top gold electrodes were connected to the voltage supply Keithley 2400 through copper wires while the $SrRuO_3$ layers were grounded by silver paste.

The ferroelectric properties of the PZT films were studied by switching the polarisation electrostatically using an IG as described in steps in Fig. 5.2 e-g. A negative 1 V was applied to the top gold electrode, separating the cations and anions leading to a poled PZT. Then the gel was peeled off as shown in Fig. 5.1c, followed by direct measurement of the PZT top surface using PFM. Subsequently, the gel was placed back on the PZT surface at a slightly different position, followed by the application of a positive 1V on the IG. The polarisation PZT was measured by PFM upon removal of the gel once more.

In a separate experiment, we characterised the PZT domain switching using the gel

by measuring the changes in tetragonal mono c-domain performing 2theta-omega scans on a Malvern Panalytical's X'Pert³ MRD as a function of the IG gate voltage. Voltages ranging from positive 20 V to negative 20 V were applied and from the PZT reflections, the lattice parameters were extracted. RSM was used to identify the in-plane a-domain.

5.3. Experimental results

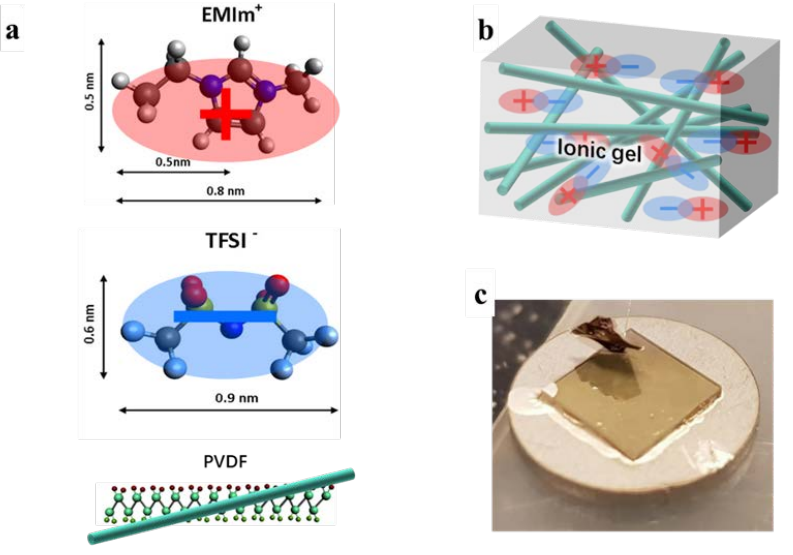

Figure 5.1. *(a) - (b) the schematics of organic molecular cross-linked in the transparent gel; (c) is the moment when ionic gel is peeled off from the PZT surface for PFM characterisation;*

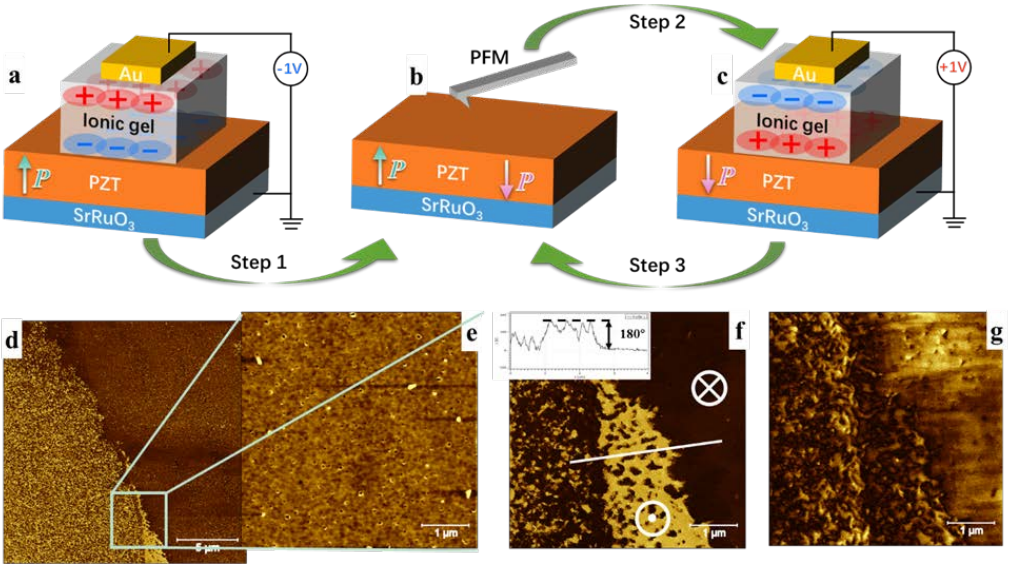

Figure 5.2. *(a) - (c) stand for the procedures for IG gated polarisation switching and the PFM; (d) – (g) present the results measured by AFM and PFM. (d) is the PFM phase in 20μm size image. a series of zoomed in scan is showed as topography in (e), the PFM phase in (f) and amplitude in (g), respectively. The inserted profile in the phase image (f) describes the phase difference before switching is less than 180°, which fits the features of M_c in our previous work. The phase difference after switching is 180°.*

Fig. 5.2 a-c show the measurements by AFM and PFM. In Fig. 5.2d the PFM phase image shows three different regions of 20μm size. Also, a series of zoomed-in scans are shown with topography in **e**, the PFM phase in **f** and the amplitude in **g**, respectively. **Fig. 5.2e** shows a smooth surface of PZT after peeling off the gel and cleaning with ethanol; The magnified phase image **f** shows on the left side a region consisting of pristine 100-200 nm PZT domains without any switching, while the middle a bright region shows up-ward switched polarisation by the first poling, and the right dark region on the right side represents the down-ward reversibly switched polarisation by a second poling. The inserted profile in the phase image describes the phase information of M_c is same as our previous work in Chapter 4. The phase difference after switching is 180° proving a full electrostatic switching that was induced by the IG. It is noteworthy that there are several nano-scale dark areas visible in the centre up-wards polarised region, indicating that those regions (denoted as

PZT-a) are different in their ferroelectric behaviour, which will be discussed in the next section.

Summarizing, the topography indicates that the original PZT surface can be restored after peeling off the gel and any residual particles could be removed by wiping with ethanol. The PFM amplitude channel shows that the domain boundaries are the result of the intrinsic signal without any cross-talk from PFM phase channel. In addition, the reversible switching in the down-wards region shows no boundaries indicating a large sized mono domain being formed by switching.

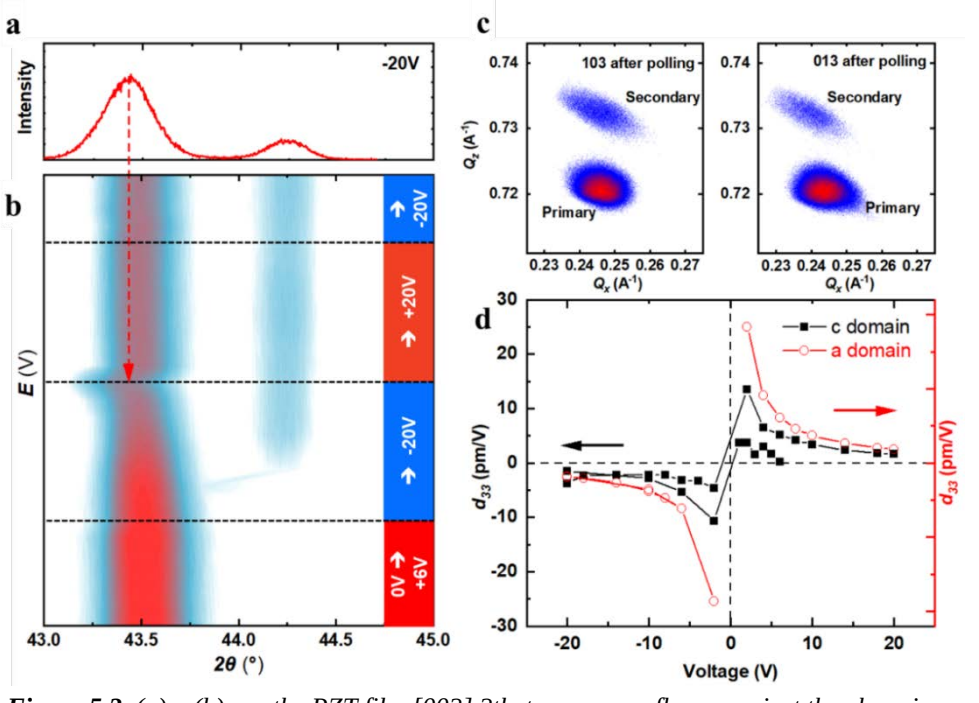

Figure 5.3. *(a) – (b) are the PZT film [002] 2theta-omega reflexes against the changing voltage form 20V to -20V; (a) particularly points to the maximum 002 peak shifting at -20V; (c) shows the RSMs of PZT primary peak (c-domain) and the secondary peak (a-domain) in (103) plane; (d) gives the calculated results of piezoelectric coefficient contributed by c-domain and a-domain, respectively.*

The mono-domain tetragonal c PZT thin film polarisation switching was measured

in-situ by XRD. **Fig. 5.3a** and **b** show the contours of PZT of the (002) reflections in 2theta-omega scan. Here it can be seen that the PZT (002) diffraction peak slightly changed from 43.522° to 43.436° during the switching. It is noteworthy that a secondary peak (PZT-se) at approximate 44.25° appears in **Fig. 5.3b** while a negative voltage is applied. The latter was not reversible, at least during the measurement time of about 2h. The primary PZT peak (PZT-pr) however showed a reversible change when changing the voltage from +20V to -20V. For better understanding of the nature of primary and secondary reflections, the RSM measurements were performed see **Fig. 5.3c**. From these measurements, the PZT lattice constants at -20V state in contrast with the original PZT lattice constant before poling were extracted as following in Table 1:

Table 5.1. the tetragonal c PZT lattice constants before and after polling

	a (Å)	**b (Å)**	**c (Å)**	**Volume (Å^3)**
Original	4.04(6)	4.04(6)	4.14(8)	67.90(3)
PZT-pr	4.11(6)	4.06(1)	4.16(5)	69.61(8)
PZT-se	4.20(1)	4.06(1)	4.09(7)	67.89(6)

The out-plane piezoelectric coefficient d_{33} was calculated and separated into contributions from c-domains and a-domains, respectively, (PZT-se) as plotted in **Fig. 5.3d**. The amount of a-domain fraction was unclear and therefore the exact number of d_{33} linked to a-domain is not given. These observations by PFM and XRD will be thoroughly discussed in the following section.

In a short summary:

- PFM observed a phase changed after IG poling;
- 2theta-omega scans showed changing against gate voltage;
- A PZT secondary peak appears in the RSMs.

5.4. Discussion

The PFM results demonstrate that reversible switching in a leaky ferroelectric thin

film can be successfully controlled by an IG induced electrostatic field placed. The phase channel showed phase contrasts, representing 100-200 nm sized up-ward and down-ward domains. These results are in agreement with our previously reported monoclinic c-type PZT on STO substrate. (Chapter 4) The observation of the up-wards and down-wards switching proves that reversible switching is possible by a 1V external field. This differs from the approximate +/-2V switching voltage that was reported in the past, which is enabled by the contribution from the interfacial electrostatic component. The voltage mobilises ions and causes a new arrangement in the IG, the accumulation of ionic potential at interface could much higher than 1V.[18, 23] Meantime, the depolarisation field at the interface of the ferroelectric film could also play a role in here. In generally the depolarisation field can be neglected for a 400 nm thick film. Such thickness of PZT film in principle is also difficult to be switched by electrostatic effects. But in case of the electrostatically controlled solid-liquid interface, the depolarisation field also contributes to polarisation switching.[30] It has been reported that a 87nm thick ferroelectric layer was switched, when the depolarisation field orientation is in the switching direction.

Now we continue with the dark regions (PZT-a) in the up-ward region. In the study of high-resolution transmission electron microscopy (HR-TEM), the dark field images showed there are threading dislocations through the whole thickness of the PZT thin film as shown in **Fig. 5.4a**. In the plane-view image, the point burgers vector of these dislocations can be confirmed using Fourier transformation, see the insert of **Fig. 5.4b**. The dislocations are distributed non-uniformly. Some of the distances are smaller than 10 nm, which is within the typical strain influence radius from the threading dislocation.[31, 32] It is logical to assume the crystal planes between these two threading dislocations are locally strained and distorted. There is maximum 20% volume of PZT-a in overall PZT could be the result of the part of the PZT that surrounds this accumulated line defects. The strain level could be entirely different from the matrix of the PZT and could lead to differences in the structure as well as the local ferroelectric behaviour. The phase difference between PZT-a and the poled up-ward matrix PZT is 180°, suggests the PZT-a preferential polarisation orientations may be down-wards.

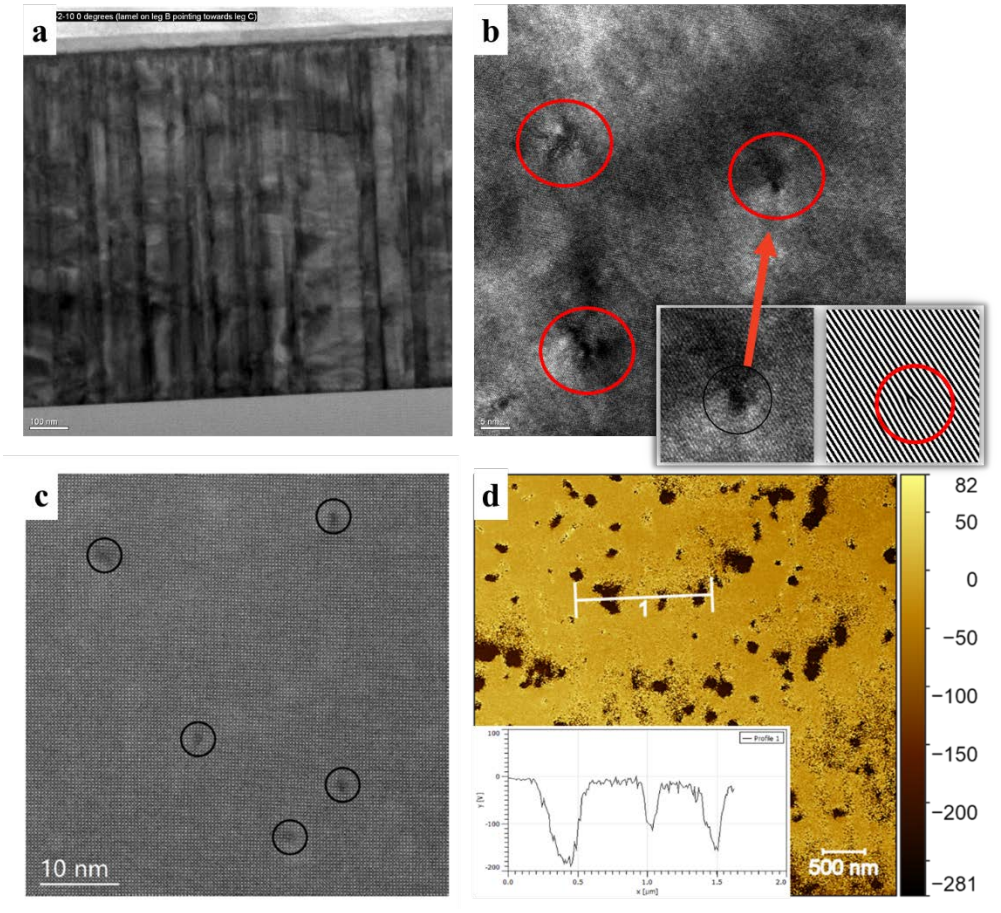

Figure 5.4. *(a) is the cross-section TEM bright field image for PZT growth on STO, the dark lines are thread dislocations through the entire PZT film; (b) is planar-view TEM image, the small inserted FFT image for one of the point defect shows a single burger vector, confirming the defects type is thread dislocation; With a smaller scale image in planar-view, (c) indicates the relative distances between the thread dislocations; the dislocations within each other affect radius may create an abnormal PZT regions (PZT-a) and PZT-a may be responsible for the unswitchable regions in (d), the inserted profile shows the phase difference between the switched up-wards PZT and the unswitchable PZT-a regions.*

As an additional demonstration of IG, for mono c-domain PZT, the appearance of secondary reflections at a negative voltage correspond to a-domains, with an

elongated a-axis. This is probably because of a ferroelastic process occurring during the c-domain 180° switching. A 90° domain wall is formed to reduce the free energy in the overall system and therefore a metastable poly-domain thin film could form. It is interesting to mention that only one a-domain was measured in the RSMs. This anisotropic in-plane ferro-elasticity switching has been seen for PZT(x=0.2) growth on $GdScO_3$ (110) and $DyScO_3$ (110) substrates.[33, 34] However, there should be no anisotropy arising from the CaF_2 cubic substrate, leaving the possibility that anisotropy comes from a relaxed SRO layer. (SRO a = 5.567Å; b = 5.530Å)[35] Meanwhile, the formation of a-domain shows a lower piezoelectric coefficient, which means the more c-domain transforms to a-domain, the lower overall d_{33} value should be measured, which leads to a significant d_{33} dropping around -/+2 V.

As a final consideration, as the external voltage was increased, electrochemical effects may dominate the interface reaction instead of electrostatic effects.[16, 36, 37] Many reports suggested the organic anions and cations may decompose and cause H^+ and O^{2-} immigration or ions doping cross the thin films underline a high electrical field modulation. Lately in 2017, Nianpeng et al. used D_2O and O_{18} to successfully demonstrated that the H^+ and O^{2-} originated from the residual water absorbed by the ionic liquid.[38] This ionic doping can change the lattice constants dramatically and it is not desired for “iontronics” in this situation. Note that, when IG of -/+ 20V was used, no significant changes in the PZT unit cell were seen. This could be caused by the fact that a dense, low defect perovskite ABO_3 is not as prone to defect migration as for example a material like $SrCoO_{2.5}$ that tolerates ions migration with a voltage lower than 20V.

In a brief summary:

- We discussed the demonstration of ferroelectric switching by IG;
- The polarisation switching by electrostatic effect is reversible;
- The tested maximum gating voltage without break-down is 20V;
- A ferroelastic switching was observed as a step of tetragonal c-domain went through a 180° polarisation switching;
- Only one direction in-plane domain was observed, it is proposed that it was due to the anisotropic strain from $SrRuO_3$ layer.

5.5. Conclusion

In this chapter, the polarisation switching was investigated in leaky ferroelectric thin films. because of the high electronic conductivity of the ferroelectric, electrostatic fields applied by a flexible IG was used for studying the switching behaviour of monoclinic c-type PZT grown on $SrTiO_3$.

PFM measurements revealed regions within the PZT that could not be switched using the IG gating and a mechanism is proposed to link the existence of threading dislocations through the whole film to these regions. Moreover, an anisotropic ferroelastic switching was studied in this work by IG gated mono c-domain PZT on CaF_2 as an additional demonstration. The assumption is that this single a-domain could be attributed to a potential anisotropy of the bottom electrode $SrRuO_3$ layer. The $SrRuO_3$ layer should be studied in more detail to confirm this hypothesis. Furthermore, a full cycle switching may be interesting to perform with the purpose of understanding the next ferroelastic switching, from in-plane a-domain to complete 180° switching. The electrostatic potential also requires more detailed study to understand the interaction between the DEL and ferroelectric depolarisation field at different external voltages. Finally, we would like to point out that with our proof of principle of the usage of the transparent and flexible IG to be functional to ferroelectric polarisation switching, the elegant and simple cut and stick dielectric IG shows great potential for research in ultra-thin, leaky film transistors.

Reference:

1. Scott, J., *Applications of modern ferroelectrics.* science, 2007. **315**(5814): p. 954-959.
2. Auciello, O., J.F. Scott, and R. Ramesh, *The physics of ferroelectric memories.* Physics today, 1998. **51**(7): p. 22-27.
3. Kimura, T., et al., *Magnetic control of ferroelectric polarization.* nature, 2003. **426**(6962): p. 55-58.
4. Mundy, J.A., et al., *Atomically engineered ferroic layers yield a room-temperature magnetoelectric multiferroic.* Nature, 2016. **537**(7621): p. 523-527.
5. Dussan, S., et al., *Magnetic control of ferroelectric interfaces.* Journal of Physics: condensed matter, 2011. **23**(20): p. 202203.
6. Yang, M.M. and M. Alexe, *Light-induced reversible control of ferroelectric polarization in BiFeO3.* Advanced Materials, 2018. **30**(14): p. 1704908.
7. Janolin, P.-E., *Strain on ferroelectric thin films.* Journal of materials science, 2009. **44**(19): p. 5025-5048.
8. Nguyen, M.D., et al., *Misfit strain dependence of ferroelectric and piezoelectric properties of clamped (001) epitaxial Pb (Zr0. 52, Ti0. 48) O3 thin films.* Applied physics letters, 2011. **99**(25): p. 252904.
9. Steenwelle, R.J.A., *Strain and composition effects in epitaxial PZT thin films.* 2012.
10. Mathews, S., et al., *Ferroelectric field effect transistor based on epitaxial perovskite heterostructures.* Science, 1997. **276**(5310): p. 238-240.
11. Wang, J.-J., B. Wang, and L.-Q. Chen, *Understanding, predicting, and designing ferroelectric domain structures and switching guided by the phase-field method.* Annual Review of Materials Research, 2019. **49**: p. 127-152.
12. Chanthbouala, A., et al., *Solid-state memories based on ferroelectric tunnel junctions.* Nature nanotechnology, 2012. **7**(2): p. 101.
13. Fong, D.D., et al., *Ferroelectricity in ultrathin perovskite films.* Science, 2004. **304**(5677): p. 1650-1653.
14. Kim, Y., et al., *Critical thickness of ultrathin ferroelectric ba ti o 3 films.* Applied Physics Letters, 2005. **86**(10): p. 102907.

15. Goldman, A., *Electrostatic gating of ultrathin films.* Annual Review of Materials Research, 2014. **44**: p. 45-63.
16. Leighton, C., *Electrolyte-based ionic control of functional oxides.* Nature materials, 2019. **18**(1): p. 13-18.
17. Ahn, C., J.-M. Triscone, and J. Mannhart, *Electric field effect in correlated oxide systems.* Nature, 2003. **424**(6952): p. 1015-1018.
18. Sharma, Y., et al., *Ionic gating of ultrathin and leaky ferroelectrics.* Advanced Materials Interfaces, 2019. **6**(5): p. 1801723.
19. Cui, B., et al., *Reversible Ferromagnetic Phase Transition in Electrode-Gated Manganites.* Advanced Functional Materials, 2014. **24**(46): p. 7233-7240.
20. Chun, H. and T.D. Chung, *Iontronics.* Annual Review of Analytical Chemistry, 2015. **8**: p. 441-462.
21. Ge, C., et al., *Metal–insulator transition induced by oxygen vacancies from electrochemical reaction in ionic liquid-gated manganite films.* Advanced Materials Interfaces, 2015. **2**(17): p. 1500407.
22. Chhetry, A., et al., *Ultrasensitive interfacial capacitive pressure sensor based on a randomly distributed microstructured iontronic film for wearable applications.* ACS applied materials & interfaces, 2018. **11**(3): p. 3438-3449.
23. Herklotz, A., et al., *Reversible control of interfacial magnetism through ionic-liquid-assisted polarization switching.* Nano letters, 2017. **17**(3): p. 1665-1669.
24. Susan, M.A.B.H., et al., *Ion gels prepared by in situ radical polymerization of vinyl monomers in an ionic liquid and their characterization as polymer electrolytes.* Journal of the American Chemical Society, 2005. **127**(13): p. 4976-4983.
25. Lee, K.H., et al., *"Cut and stick" rubbery ion gels as high capacitance gate dielectrics.* Advanced Materials, 2012. **24**(32): p. 4457-4462.
26. Song, D., et al., *Freestanding ion gels for flexible, printed, multifunctional microsupercapacitors.* ACS applied materials & interfaces, 2019. **11**(10): p. 9947-9954.
27. S. Barbosa, M., et al., *Structure of the Electrical Double Layer at the Interface between an Ionic Liquid and Tungsten Oxide in Ion-Gated*

Transistors. The journal of physical chemistry letters, 2020. **11**(9): p. 3257-3262.

28. Ferris, R.J., et al., *Electric double layer formed by polarized ferroelectric thin films.* ACS applied materials & interfaces, 2013. **5**(7): p. 2610-2617.
29. Shao, X., et al., *Low-Voltage Large-Current Ion Gel Gated Polymer Transistors Fabricated by a "Cut and Bond" Process.* ACS applied materials & interfaces, 2015. **7**(8): p. 4759-4762.
30. Xu, D.-D., et al., *Ion adsorption-induced reversible polarization switching of a van der Waals layered ferroelectric.* Nature communications, 2021. **12**(1): p. 1-9.
31. Jia, C., et al., *Effect of a single dislocation in a heterostructure layer on the local polarization of a ferroelectric layer.* Physical review letters, 2009. **102**(11): p. 117601.
32. Marrocchelli, D., L. Sun, and B. Yildiz, *Dislocations in SrTiO3: easy to reduce but not so fast for oxygen transport.* Journal of the American Chemical Society, 2015. **137**(14): p. 4735-4748.
33. Khan, A.I., et al., *Voltage-controlled ferroelastic switching in Pb (Zr0. 2Ti0. 8) O3 thin films.* Nano letters, 2015. **15**(4): p. 2229-2234.
34. Yuan, G., et al., *Ferroelastic-Domain-Assisted Mechanical Switching of Ferroelectric Domains in Pb (Zr, Ti) O3 Thin Films.* Advanced Electronic Materials, 2020. **6**(7): p. 2000300.
35. Gan, Q., et al., *Lattice distortion and uniaxial magnetic anisotropy in single domain epitaxial (110) films of SrRuO 3.* Journal of applied physics, 1999. **85**(8): p. 5297-5299.
36. Gu, Y., et al., *Oxygen-Valve Formed in Cobaltite-Based Heterostructures by Ionic Liquid and Ferroelectric Dual-Gating.* ACS applied materials & interfaces, 2019. **11**(21): p. 19584-19595.
37. Li, H.-B., et al., *Electric-field control of ferromagnetism through oxygen ion gating.* Nature communications, 2017. **8**(1): p. 1-7.
38. Lu, N., et al., *Electric-field control of tri-state phase transformation with a selective dual-ion switch.* Nature, 2017. **546**(7656): p. 124-128.

Supplementary materials

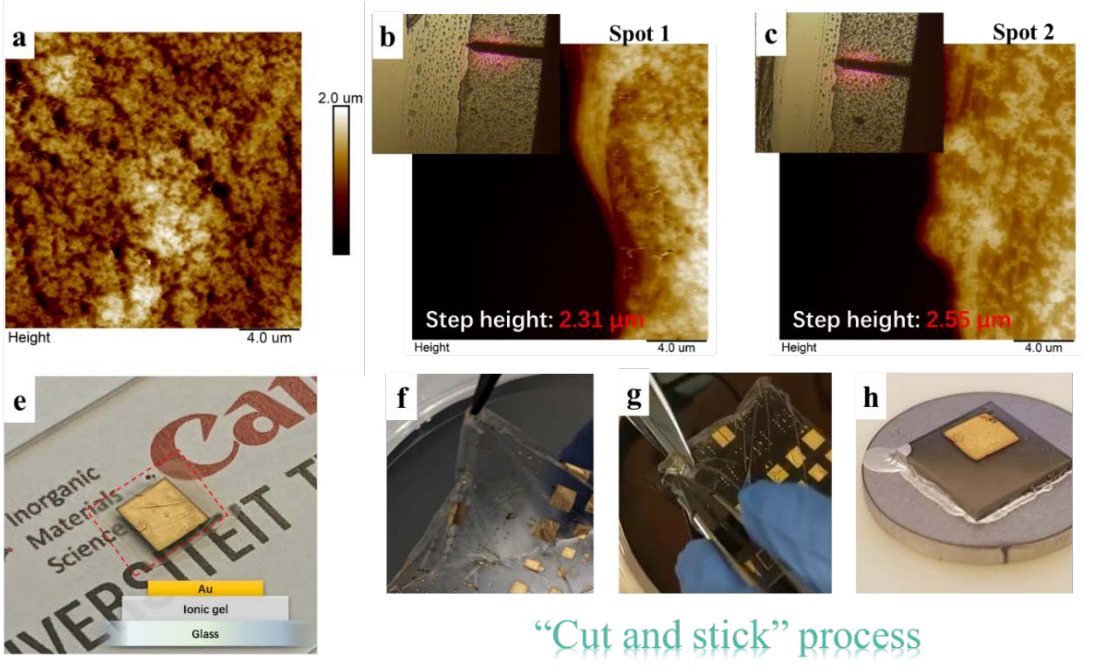

Figure S5.1. *(a) is the topography of the IG scanned by AFM; (b) and (c) selected two different locations and measured the thickness of the IG is given inside the images; (e) gives an example of the transparent IG with gold top electrode; (f) – (h) indicate the "cut and stick" process and from this series of image.*

Chapter 6 Summary and outlook

6.1. Research summary

The aim of this thesis is to experimentally verify a phenomenological three-domain model for clamped ferroelectric thin films, along with its piezoelectric properties extensions specified in $PbZr_xTi_{1-x}O_3$(PZT) thin films under different boundary conditions (strains, temperature or electrical field). The thin film samples are produced by pulsed laser deposition (PLD), and the effect of thermal misfit strain induced during the cooling process after deposition was studied. In contrast with the epitaxial strain in thin films (less than 50nm thick), thin films with typical device device thickness are frequently dominated by the thermal strain. The three-domain model results show an enhancement in piezoelectric properties of thermal strained PZT (composition x=0.6) in compared with its bulk properties. Two strategies were followed to validate the three-domain model and the predicted properties. Moreover, I was able to derive a PZT film phase diagram.

First an introduction and experimental section, describe the details of the three-domain model and the most important model results, as well as tests of the experimental strategy. The PZT film was deposited on a Si wafer and made into a cantilever for a 4-points bending test. By applying a longitudinal tensile strain, the measured accumulated polar surface charges enabled to derive the transversal piezoelectric coefficient e_{31}. However, bending calculations and finite element analysis (FEA) simulations show that the desired tensile strain can not be reached using a Si substrate. Under all tested circumstances, the Si yielded before PZT film showing any changes for e_{31} as was predicted by three-domain model. The details of the calculations and simulations setups are presented in **Chapter 2**.

The experimental evidence presented in Chapter 4, RSMs showed a definitive confirmation of the PZT symmetry. However, for relaxed thin films, the interpretation of the RSMs should be different for the case of epitaxially strained films. In **Chapter 3**, a mathematical description for relaxed thin films was established with a significant contribution from Dr. E. Houwman. It includes the

tetragonal phase, the rhombohedral phase and the A-type, C-type monoclinic phase. The calculations allowed me to explain the RSMs measurements in Chapter 4, and most interestingly pointed at a distorted C-type monoclinic symmetry for PZT-S. Furthermore, this description shows universal applications for all RSM interpretation, as the results are in agreement with other publications.

In the alternative strategy presented in **Chapter 4**, temperature dependent reciprocal space mapping (RSM) was used to identify the crystal symmetry of a PZT (x=0.6) film grown on a 70% $PbMg_{1/3}Nb_{2/3}O_3$-30%$PbTiO_3$ (PMN-PT) substrate, a $SrTiO_3$ substrate and a CaF_2 substrate. Due to the thermal strain, at room temperature, the PZT on PMN-PT (PZT-P) has the rhombohedral symmetry, while the PZT on STO (PZT-S) is monoclinic and the PZT on CaF_2 (PZT-C) is single domain tetragonal. The paraelectric phase to ferroelectric phase transitions for each sample take place as predicted by the calculated phase diagram when tracing the thermal misfit strain path during the cooling. Moreover, the piezoelectric component for each sample was measured using piezoelectric force microscopy (PFM) with a reference sample. Qualitatively, the trend of found for the d_{33} values agree with the model, the quantitative differences can be explained by the limitations of measurement method. It was concluded that I successfully proved the validity of the three-domain model. However, based on the obtained results of the experiments, I propose further refinements of the phase diagram. The meta-stable, monoclinic phase for PZT-S was measured instead of the predicted tetragonal a/b/c phase.

As for the measurements of the properties, the threading dislocations in PZT films that are possibly created by misfit strain, limited the direct DC electrical field strength due to a high leakiness of the capacitors. Therefore, an ionic gel (IG) was used to induce an electrostatic field. The IG shows benefits such as being effectively an electronic insulator, but with a high ionic conductivity, and additionally a strong mechanical strength and transparency. A free-standing IG was prepared with sputtered gold as a top electrode, subsequently cut and stuck onto a functional film to complete the transistor, known as “cut and stick” process. The PZT-S was successfully reversibly switched by this method as was verified by PFM. Moreover, the IG poled PZT-C was *in-situ* measured by X-ray diffraction (XRD) under

application of a variable voltage to be able to determine the out-of-plane piezoelectric coefficient. A maximum of 20V was applied without observing any leakage, and the ferroelastic switching from c-domain to a-domain was discovered. Since the CaF_2 substrate itself is cubic, the observation of a single a-domain was speculated to be linked to the anisotropic in-plane strain induced by bottom $SrRuO_3$ layer. These results in **Chapter 5** demonstrated the merits using an IG and its potential applications in leaky ferroelectric transistors or flexible wearable devices.

6.2. Outlook

It is an achievement that this thesis fulfils its project subject with solid experimental evidence and several discoveries. However, some problems require further study. First of all, the three-domain model should be tested for other secondary order phase transitions of clamped thin films. In Chapter 4, the thermal strain applied was mostly compressive, a 0.005 tensile thermal strain is desired due to its larger predicted enhancement in piezoelectric response compares with PZT-S. Secondly, the origin of the threading dislocations remains unclear, but no near nucleation point was observed at the PZT/SRO interface. Thirdly, in Chapter 5 the motion of ions inside IG while applying a gating voltage is not clear. A series of impedance measurements are required to understand the underlying mechanisms. Besides, as the PZT-C was not fully switched, it remains a question on how a-domains switch to c-domains, although, some studies suggest that a b-domain would appear if the gating voltage is increased and finally both a-domain and b-domain become to c-domain. Last but not least, the possible anisotropy induced from the $SrRuO_3$ is worth studying.

Hoofdstuk 6 Samenvatting en vooruitzichten

6.1. Onderzoekssamenvatting

Het doel van deze thesis is om experimenteel een fenomenologisch 3-domeinmodel voor geklemde, ferro-elektrische dunne films te verifiëren, samen met de bijbehorende piëzo-elektrische eigenschappen van $PbZr_xTi_{1-x}O_3$ (PZT) dunne films bij verschillende omstandigheden (rek, temperatuur of elektrisch veld). De dunnefilmmonsters zijn geproduceerd met gepulseerde laser depositie (PLD), en het effect van de thermische rek door verschillende roosterconstanten, geïnduceerd tijdens het afkoelproces na depositie is bestudeerd. In tegenstelling tot de dunne films (minder dan 50 nm dik) met epitaxiale rek, speelt bij monsters met typische toepassingsafmetingen thermische rek meestal een dominante rol. De resultaten van het 3-domeinmodel laten een verhoging van de piëzo-elektrische eigenschappen van thermisch gerekte PZT (compositie x=0.6) zien, vergeleken met bulk eigenschappen. Er zijn twee strategieën gevolgd om het 3-domeinmodel en de voorspelde eigenschappen te valideren. Daarbij is het gelukt om een PZT-film fasediagram op te stellen.

Ten eerste worden de details van het 3-domeinmodel en de belangrijkste resultaten van het model beschreven in de introductie en experimentele sectie. Hierbij worden ook de tests beschreven die gedaan zijn om de experimentele strategie te bepalen. De PZT-films zijn gedeponeerd op siliciumwafels en omgevormd tot een vrijdragende balk om een vierpuntsbuigtest te kunnen doen. Door longitudinale rek aan te brengen maken de gemeten polaire oppervlakteladingen het mogelijk om de transversale piëzo-elektrische coëfficiënt e_{31} af te leiden. Echter, buigberekeningen en eindige-elementenanalyse (FEA) simulaties laten zien dat de gewenste rek niet bereikt kan worden door gebruik van een silicium (Si) substraat. Bij alle geteste omstandigheden begaf het Si het voordat de PZT-film enige verandering in de e_{31}

liet zien, zoals voorspeld door het 3-domeinmodel. De details van de berekeningen en simulaties zijn te lezen in **Hoofdstuk 2**.

In deze thesis zijn röntgendiffractiemetingen gebruikt om de PZT-symmetrie te bevestigen. Echter, voor gerelaxeerde dunne films is de interpretatie van röntgendiffractie anders dan voor epitaxiaal gerekte films. In **Hoofdstuk 3** wordt een wiskundige beschrijving gegeven voor gerelaxeerde films. Mede dankzij een grote bijdrage van dr. E. Houwman. Deze beschrijving behelst de tetragonale, rhombohedrische en de type-A en -C monokliene fases. De berekeningen maakten het mogelijk de röntgendiffractiemetingen te verklaren, zoals beschreven in Hoofdstuk 4, en wezen in de richting van een vervormde type-C monokliene symmetrie voor PZT gedeponeerd op $SrTiO_3$ (STO) substraten. Daarbij is deze beschrijving universeel toe te passen op de interpretatie van röntgendiffractiemetingen, aangezien de resultaten in overeenstemming zijn met andere publicaties.

Bij de alternatieve strategie in **Hoofdstuk 4** zijn temperatuurafhankelijke röntgendiffractiemetingen gebruikt om de kristalsymmetrie van PZT (x=0.6) films te achterhalen. Deze films zijn gegroeid op een $70\%PbMg_{1/3}Nb_{2/3}O_3$-$30\%PbTiO_3$ (PMN-PT) substraat, een $SrTiO_3$ substraat en een CaF_2 substraat. Door de thermische rek op kamertemperatuur heeft de PZT op PMN-PT (PZT-P) een rhombohedrische symmetrie, terwijl de PZT op STO (PZT-S) een monokliene symmetrie heeft en de PZT op CaF_2 (PZT-C) een tetragonale symmetrie. De faseovergang van para-elektrisch naar ferro-elektrisch vindt voor elk monster plaats zoals voorspeld werd door het berekende fasediagram, bij het volgen van de thermische rek tijdens het afkoelen. Daarbij is de piëzo-elektrische component gemeten voor elk monster doormiddel van piëzoresponskrachtmicroscopie (PFM) en een referentiemonster. Kwalitatief klopt de gevonden trend voor de d_{33}-waarden met het model. The kwantitatieve verschillen kunnen verklaard worden door de

limiet van de gebruikte meetmethode. Al met al kan er geconcludeerd worden dat het 3-domeinmodel succesvol is bewezen. Echter, gebaseerd op de gevonden resultaten is het aan te raden om het PZT fasediagram verder te verfijnen. De metastabiele, monokliene fase van PZT-S is tegenstrijdig met de voorspelde tetragonale a/b/c-fase**.**

Het meten van de eigenschappen werd gelimiteerd door schroefdislocaties in de PZT dunne films. Deze dislocaties zijn mogelijk ontstaan door de grote rek in de PZT films. Hierdoor is de DC elektrische veldsterkte sterk gelimiteerd, aangezien de gemaakte structuren een hoge lekstroom hadden. Daarom is gebruik gemaakt van een ionische gel (IG) om een elektrostatisch veld te induceren. De IG is effectief een isolator, maar heeft wel een hoge ionische geleiding en daarbij een hoge mechanische sterkte en transparantie. Een vrijstaande IG is gemaakt met gesputterd goud als topelektrode. Vervolgens is de gel gesneden en op een functionele film aangebracht om een transistor te maken. De PZT-S is op deze manier reversibel omgeschakeld en dit is bevestigd door PFM. Bovendien is de IG-gepoolde PZT-C *in-situ* gemeten met röntgendiffractie terwijl er een variabel voltage aangelegd werd over het monster. Hiermee is de piëzo-elektrische coëfficiënt achterhaald. Bij het aanleggen van maximaal 20 V, zonder dat er enige lekstroom gemeten is, is de ferro-elastische omschakeling van c-domeinen naar a-domeinen ontdekt. Aangezien het CaF_2 substraat kubisch is, is de observatie van een enkel a-domein wellicht veroorzaakt door de anisotropische rek geïnduceerd in de $SrRuO_3$ laag. Deze resultaten in **Hoofdstuk 5** demonstreren het voordeel van het gebruik van IGs en de potentiële toepassingen in flexibele, draagbare apparaten of ferro-elektrische transistoren met een hoge lekstroom.

6.2. Vooruitzichten

Het experimentele bewijs en verschillende ontdekkingen in deze thesis hebben het

project tot een goed einde gebracht. Echter zijn er nog een paar zaken die verdere studie vereisen. Ten eerste zou het 3-domeinmodel verder getest moeten worden voor andere geklemde, dunne films met tweede-orde-faseovergangen. In Hoofdstuk 4 is de toegepaste thermische rek samendrukkend, terwijl een 0.005 uitrekkende thermische rek gewenst is, vanwege de grotere voorspelde verhoging van de piëzo-elektrische respons vergeleken met PZT-S. Ten tweede is de origine van de schroefdislocaties onduidelijk. Aangezien er geen deeltjes of moleculen zijn waargenomen bij het PZT/SRO grensvlak, is het mogelijk dat de dislocaties veroorzaakt worden door een rekeffect. Ten derde is er in Hoofdstuk 5 nog onduidelijkheid over de beweging van de ionen in de IG, terwijl er een gatespanning aangelegd wordt. Impedantiemetingen zijn nodig om de onderliggende mechanismes te begrijpen. Daarbij, aangezien de PZT-C niet compleet omgeschakeld is, is het nog steeds de vraag hoe a-domeinen omschakelen tot c-domeinen. Sommige studies suggereren dat b-domeinen ontstaan als de gatespanning genoeg opgehoogd wordt, waarna uiteindelijk zowel a- als b-domeinen veranderen in c-domeinen. Tot slot is de anisotropie die door het $SrRuO_3$ geïnduceerd is nog nooit gerapporteerd en dit zou verder bestudeerd kunnen worden.

List of publications

1. Meng Wu*, **Sizhao Huang***, Hui Zeng, Gertjan Koster, Yu-Yang Huang, Jin-Cheng Zheng, HuiQiong Wang, *"Asymmetric response of electrical conductivity and V valence state to strain in cation-deficient $Sr_{1-y}VO_3$ ultrathin films based on absorption measurements at the V L2-and L3-edges"*, Journal of synchrotron radiation (2019). *** for first co-authors**

2. **Sizhao Huang**, Evert Houwman, Kurt Vergeer, Nicolas Gauquelin, Andrey Orekhov, Dmitry Chezganov, Johan Verbeeck, Sixia Hu, Gaokuo Zhong, Jani Peräntie, Yukuai Liu, Frans Blom, Gertjan Koster, Guus Rijnders, *"Substrate induced thermal strain-enhanced piezoelectricity in $PbZr_{0.6}Ti_{0.4}O_3$ piezoelectric"*, (prepare for submitting to Advanced Functional Materials 2021) – Ph.D. thesis Chapter 4.

Contributed to journal articles:

1. Singh, Deepak; Birkhölzer, Yorick; Cunha, Daniel; Dubbelink, Thijs; **Huang, Sizhao**; Hendriks, Theodoor; Lievens, Caroline; Huijben, Mark, "*Enhanced cycling and rate capability by epitaxially matched conductive cubic TiO coating on $LiCoO_2$ cathode film"*, ACS Applied Energy Materials (2021)

2. Jordi Antoja-Lleonart, Silang Zhou, Kit De Hond, **Sizhao Huang**, Gertjan Koster, Guus Rijnders, Beatriz Noheda *"Atomic layer deposition of SiO_2-GeO_2 multilayers"*, Applied Physics Letters (2020)

3. F. Yen, **S. Z. Huang**, S. X. Hu, L. Y. Zhang, and L. Chen, "*Indirect observation of molecular disassociation in solid benzene at low temperatures"* (arXiv preprint arXiv:1703.01719 (2017)

4. Wu, Di, **Sizhao Huang**, Dan Feng, Bing Li, Yuexing Chen, Jian Zhang, and Jiaqing He. "*Revisiting AgCrSe 2 as a promising thermoelectric material*", Physical Chemistry Chemical Physics 18, no. 34 (2016): 23872-23878.

5. Phu Tran Phong Le, **Sizhao Huang**, Minh Duc Nguyen, Johan E. ten Elshof and Gertjan Koster, *"Tuning the Metal Insulator Transition of Vanadium Dioxide on Oxide Nanosheets"*, (submitted for Applied Physics Letters 2021)

6. Binbin Chen, Nicolas Gauquelin, Nives Strkalj, **Sizhao Huang**, Ufuk Halisdemir, Minh Duc Nguyen, Daen Jannis, Martin Sarott, Felix Eltes, Stefan Abel, Matjaž Spreitzer, Manfred Fiebig, Morgan Trassin, Jean Fompeyrine, Johan Verbeeck, Mark Huijben, Guus Rijnders, and Gertjan Koster, "*Signatures of strain-enhanced out-of-plane ferroelectricity in BaTiO3 superlattices integrated on silicon*" (Nature Communication 2021 in reviewing)

Acknowledgements

It appears that this thesis is a four-year hard-working of one man based on the epitaxial $PbZr_xTi_{1-x}O_3$ thin film phase diagram and electromechanical properties. However, Roma city was not built in one day, neither by one person. Here I would like to express my sincere gratitude to all those people, whom have accompanied me and supported me through all these years in all sorts of ways.

First, I would like to thank my supervisor **Guus Rijnders** for giving me this very opportunity to Twente, in pursuing a Ph.D. degree. You are very knowledgeable in many topics and very open-minded in my research directions. I always enjoy discussing with you, it was your professional criticism and kind encouragement that drove me this far. I would like to thank my supervisor **Gertjan Koster**, whom has been kindly offering his valuable advises in many aspects, from reciprocal space mapping to depressive emotion issues, from scientific writing to colour selections in figures. You enlighten me with your practical and joyful suggestions, make my research efficient and delightful. I would also thank **Evert Houwman**, whom can always offer insight and precise physical explanations to my questions. Without you, I would not imagine how I can finish Chapter 3 on my own. I would also show my appreciation to **Frans Blom** from Canon. Your frequent visiting and thoughtful discussion helped me to shape the thesis contents. I was also very impressed by our tour at Canon company. I would also be grateful to **André, Bernard, Christ, Minh, Mark** and **Monica** for fruitful scientific discussions. (The names are in alphabet order) As a former lab technician who controlled budgets, I deeply appreciate the staff: **Daniel, Dominic, Daan, Frank, Harry, Jose, Karin** and **Marion**. (The names are in alphabet order) I know you are the foundation of the IMS group.

By this opportunity I would also like to thank my collaborators. **Nicolas Gauquelin**, **Rico Keim**, **Lei Jin**, **Xiaobin Xie** and **Henk Wolferen**, thank you all for the nice STEM images, SEAD, CBED and other conversations we had. Thank **Meng Wu** for our continuous years' work on LTO, SVO and XAS measurements. Thank **Gaokuo Zhong**, **Hubert Gojzewski, Jianjun Yao**, **Lu You** and **Shuzhen Yang** for all sorts of SPM measurements and joyful discussions. Thanks to **Sixia Hu**, **Haoliang Huang** for XRD, RSM and GI-XRD discussions, particularly allowing me to remotely

measure the XRD. Especially thank **Yukuai Liu** whom frequently advised me on ferroelectrics devices and BCZTO, also all the years you have taught me how to conduct all experiments hand by hand since SUSTech.

I also want to thank my colleagues for serious scientific discussions and fruitful chatting. All IMS members and part of ICE, PIN members have shown their great support to my research, for this I could not be more grateful. I would specially thank my office-mates: **Jaap, Laura, Kit, Yorick and Rui**. Every moment at the office has been very delightful and productive. I also thank **Binbin, Ufuk, Jani, Liao**, **Kurt, Pierre-Alexis, Deepak** and **Jian-Yao**. You have shown how to be a postdoc. I particularly want to thank **Jun**, **Thanh** and **Sina**. Our PZT gang, you cannot imagine how sad it was to see you leaving, and how cheerful to see you have started new careers. I personally appreciate **Jun** and **Phu** choosing me to be their paranymph. It was my great honour and great pleasure. I wish to thank all past and current IMS members whom have not only been the colleagues to support my study, but also been the friends to care for each other.

Some of my disciplines and experience were forged at SUSTech, nowadays turning out to be my useful skills during my research. Herein, I would deeply appreciate **Lang Chen**, **Chuanwei Huang**, **Yukuai Liu**, **Sixia Hu**, **Mao Ye**, **Meng Wu**, **Deyang Chen** and **Zuhuang Chen** for the coaching and assistance in the old times. I would also extend my gratitude to **Pu Yu**, **Junling Wang**, **Yinhao Chu**, **Houbin Huang** and **Xiaojun Zhang** whom kindly shared their wisdom when I needed one. My dearest roommates **Xiji**, **Yang**, **Xiaobin** and **Shizhang** always contribute fruitful discussions over a diverse background from DFT to STM.

At the end, I wish to thank my great Chen(陈) family. It is an honourable and proud family that always gives me the strength to overcome the difficulties. My dear brothers **Hu** and **Gao** took the responsibilities to look after the elders while I was absent in Wuhan during the pandemic. It is exactly the same spirit of unity, caring and sacrifice that the family has shown in the 1911 Revolution, Sino-Japanese War, Civil War and Cultural Revolution. I wish my aunt **Yuyan Chen** and grandfather **Zhonghua Chen** can be proud of my achievements.

During the hard times, only one person nearby, **Zhen**, has shown her support. The bonding between her and me was built by the four-leaf clover and five-leaf clover, which is blessed. **Kuroshio** has accompanied me for more than 10 years. He plays an indispensable role in my small family. The coming of **Asashio** during the lock-down, was one of the most cheerful things I have experienced so far. I am the lucky man to have you as a company, to share every moment of my joy and tears.